Atmospheric Super-Rotation on Venus With a Simplified Global Circulation Model

Thesis

UNRESTRICTED

Department of Physical Sciences
The Open University

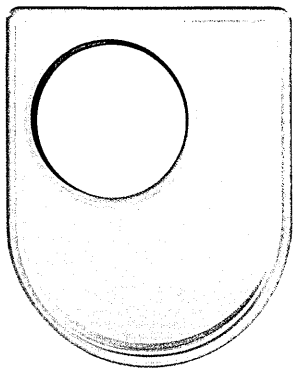

The Open University

Jon Dawson

Atmospheric super-rotation on Venus with a simplified global circulation model

A thesis submitted for the degree of Master of Philosophy

Date of Submission: 26 September 2012
Date of Award: 28 April 2014

Milton Keynes, September 2012
Corrected, March 2014

Abstract

A spectral GCM for Mars was converted to Venus parameters (radius, gravity, rotation rate), and tested to determine the optimum configuration for use as a Venus Global Circulation Model.

Super-rotation, a circulation of the atmosphere faster than the underlying planet, is a particular feature of the of Venus' atmosphere where the wind speed at the cloud tops is $\sim 100\ \mathrm{m\,s^{-1}}$. It is important that the model developed can reproduce this feature.

A reference simulation was performed at T21 resolution and forced with a realistic temperature profile, super-rotation was achieved of $\sim 50\ \mathrm{m\,s^{-1}}$ with strong meridional circulation. Topography was added and found to make little difference to the super-rotation, the meridional circulation was stronger than the reference with counter cells developing above the high elevation features. Tests were performed with increased background temperature profiles, and therefore stability, used for the forcing. It was found that peak zonal winds increased and the meridional circulation weakened as the stability increased. Realistic wind speeds could be achieved by tuning the temperature increase. A simple diurnal cycle was introduced and the results presented when run with a maximum temperature increase of 100 K over the reference simulation temperature profile.

The sensitivity of the model to vertical and horizontal resolution was tested. It was found at that 50 vertical levels provided the best compromise between good results and the computer time required. The final value of global super-rotation and the time taken for the simulation to reach equilibrium were found to be strongly dependent on the horizontal resolution. T42 resolution reaching equilibrium faster than the lower resolutions tested thus offsetting the additional computer time required.

Contents

Abstract i

Publications xiii

1 Introduction **1**

1.1 Venus 1

1.2 Planetary and atmospheric parameters 3

1.3 Aims of this research 4

1.4 Structure of this thesis 5

2 The Venusian atmosphere **9**

2.1 The atmosphere of Venus 10

2.2 Current atmospheric structure 11

2.2.1 The greenhouse effect 12

2.3 Evolution of the Venusian atmosphere 18

2.4 Circulation of the Venusian atmosphere 19

2.5 Features and waves seen in the atmosphere 23

2.6 Super-rotation 27

2.6.1 An example of a super-rotation calculation 29

2.7 Summary 30

3 Previous studies of Venusian atmosphere dynamics **33**

3.1 Background to modelling studies 34

3.1.1 Hide's theorem 34

3.1.2 Moving flame 34

3.1.3 The Gierasch mechanism 35

3.1.4 Held and Hou (1980) 36

3.2 One and two-dimensional models 36

3.2.1 Kalnay de Rivas (1975) 36

3.2.2 Young and Pollack (1977) 37

3.2.3 Rossow and Williams (1979) 38

3.3 Three dimensional modelling after Pioneer Venus 39

3.3.1 Rossow (1983) 40

3.3.2 Mayr and Harris (1983) 40

3.3.3 Covey et al. (1986) 41

3.3.4 del Genio and Zhou (1996) 42

3.3.5 Yamamoto and Takahashi (2003a,b, 2004, 2006) 43

3.3.6 Lee, Lewis and Read (2007) 46

3.3.7 Herrnstein and Dowling (2007) 48

3.3.8 Hollingsworth, Young, Schubert, Covey and Grossman (2007) 48

3.3.9 Lee and Richardson (2010) 48

3.3.10 LMD: Crespin, Lebonnois, Hourdin, Eymet, Fournier and Forget (2006) 49

3.3.11 The VSGCM, the model described in this document 52

3.4 Summary 54

4 The Venus Simplified Global Circulation Model and Set up for Experiments **57**

4.1 History of the model 58

4.2 The Spectral core 58

4.3 Spectral models vs. Grid Point 59
4.4 Radiative temperature 60
4.5 Settings for experiments 62
4.5.1 Vertical levels 62
4.5.2 Sigma levels 62
4.5.3 Sigma to Height conversion: Pseudo heights 64
4.5.4 Time-steps per day 65
4.5.5 Rotation rate 65
4.5.6 Planetary parameters 66
4.5.7 Restoration and Friction timescales 66
4.5.8 Run length 67
4.6 Summary 68

5 Results: Reference runs and Topography **69**

5.1 Base run with sponge layer on
eddies only 71
5.1.1 Atmospheric Angular Momentum 71
5.1.2 Zonal wind 73
5.1.3 Local super-rotation index 74
5.1.4 Mean Meridional Circulation 75
5.1.5 Temperature anomaly 76
5.2 Base run with sponge layer on all terms 77
5.2.1 Atmospheric Angular Momentum 77
5.2.2 Zonal Wind 78
5.2.3 Local super-rotation index 79
5.2.4 Mean Meridional Circulation 80
5.2.5 Temperature anomaly 81
5.3 Summary of reference simulations 81
5.4 Topography 84

5.4.1 Topography data 86
5.4.2 Results with topography 86
5.4.3 Atmospheric Angular Momentum 88
5.4.4 Zonal wind 89
5.4.5 Local super-rotation index 91
5.4.6 Mean Meridional Circulation 92
5.5 Summary of topography experiments 93

6 Modified background stability & diurnal cycle **95**

6.0.1 Stability 96
6.1 T21 experiments with modified background stability forcing 98
6.1.1 Atmospheric angular momentum 98
6.1.2 Zonal wind 100
6.1.3 Local super-rotation index 102
6.1.4 Mean meridional circulation 102
6.1.5 Temperature anomaly 105
6.2 T42 experiments with modified background stability forcing 105
6.2.1 Atmospheric angular momentum 106
6.2.2 Zonal wind 106
6.2.3 Local super-rotation index 107
6.2.4 Mean meridional circulation 107
6.3 Summary of modified background stability experiments 109
6.4 Diurnal cycle 112
6.4.1 Atmospheric Angular Momentum 114
6.4.2 Zonal wind 115

6.4.3 Local super-rotation index 117
6.4.4 Mean Meridional Circulation 118
6.4.5 Temperature anomaly 119
6.5 Summary of diurnal cycle experiments 120

7 Resolution **123**
7.1 Vertical resolution 123
7.1.1 Vertical resolution with N_9 forcing 123
7.1.2 Atmospheric Angular Momentum 124
7.1.3 Zonal wind 125
7.1.4 Local super-rotation index 125
7.1.5 Vertical resolution with N_4 forcing 127
7.1.6 Atmospheric Angular Momentum 127
7.1.7 Zonal wind 128
7.1.8 Local super-rotation index 128
7.2 Summary of vertical resolution experiments 130
7.3 Horizontal resolution 133
7.3.1 Horizontal resolution with N_9 forcing 133
7.3.2 Atmospheric Angular Momentum 133
7.3.3 Zonal wind and super-rotation 135
7.3.4 Horizontal resolution with N_4 forcing 138
7.3.5 Atmospheric Angular Momentum 138
7.3.6 Zonal wind and super-rotation 139
7.4 Summary of horizontal resolution experiments 142

8 Summary and discussion **145**
8.1 Summary 145
8.2 Rationale and key science 151

8.3 Aims of the research 155
8.4 Future work 156

List of Figures

2.1 Cloud layers and wind speeds 12

2.2 The radiative energy flux for Venus and Earth 14

2.3 Mean temperature profiles calculated for Venus and Earth 16

2.4 Measured temperature profiles for Venus and Earth 17

2.5 The Y-feature, IR image from Pioneer Venus 20

2.6 Venus zonal winds measured from cloud tracking of Galileo images . 21

2.7 Wind profiles at cloud level. From Sánchez-Lavega et al. (2008) . . . 22

2.8 Schematic of the possible Venus atmospheric circulations 23

2.9 Image of polar vortex - from Pioneer Venus 24

2.10 Image of double eye 25

2.11 Wave patterns in the clouds of Venus 26

2.12 $\bar{u}$ profile used for example S calculation 30

3.1 Mean solar heating for Yamamoto and Takahashi (2003b) 44

3.2 Latitude-height cross section of longitudinally averaged zonal flow (From Yamamoto and Takahashi (2003b)) 45

3.3 Zonal winds from Lee et al. (2007) 47

3.4 Wind and MMC plots from Lebonnois et al. (2010) 51

4.1 Thermal forcing 61

4.2 Equator - pole temperature 61

4.3 Sigma levels 63

5.1 Time evolution of S for base run with sponge layer on eddy terms . . 72
5.2 Zonal wind for base run with sponge layer on eddy terms only 73
5.3 s for base run with sponge on eddy terms 74
5.4 Mean Meridional Circulation for base run with sponge on eddy terms 75
5.5 ΔT for base run with sponge on eddy terms 76
5.6 Time evolution of S for base run with sponge on all terms 77
5.7 Zonal wind for base run with sponge on all terms 78
5.8 Plot of s for base run with sponge on all terms 79
5.9 Mean Meridional Circulation for base run with sponge on all terms . . 80
5.10 ΔT for base run with sponge layer on all terms 81
5.11 Topographic map of the Venusian surface. 84
5.12 Plot of Magellan topographic dataset. 87
5.13 Surface pressure for simulation using topography at T21 resolution. . 87
5.14 Time development of S with topography 88
5.15 $\bar{u}$ for simulation with topography 89
5.16 $\bar{u}$ difference for simulation with topography 90
5.17 s for simulation with topography 91
5.18 MMC for simulation with topography 92

6.1 MBS Thermal forcing 96
6.2 Brunt-Viäsälä frequency squared, N^2 97
6.3 Time evolution of S with MBS forcing 98
6.4 $\bar{u}$ and s for MBS forcing states 101
6.5 MMC and temperature anomaly for MBS forcing states 104
6.6 Time development of S for T42 with MBS forcing 106
6.7 $\bar{u}$,s and MMC for T42 with MBS forcing 108
6.8 Diurnal restore state temperature 113
6.9 Time development of S for diurnal cycle 114
6.10 Zonal wind using diurnal cycle 115

6.11 Zonal wind difference from N_9 forcing using diurnal cycle 116
6.12 Super-rotation index using diurnal cycle 117
6.13 MMC using diurnal cycle 118
6.14 Temperature anomaly using diurnal cycle 119

7.1 Time development of S for NL experiments with N_9 forcing 124
7.2 $\bar{u}$ and s for vertical level experiments with N_9 forcing 126
7.3 Time development of S for NL experiments with N_4 forcing 127
7.4 $\bar{u}$ and s for vertical level experiments with N_4 forcing 129
7.5 Time development of S for horizontal resolutions 134
7.6 $\bar{u}$ and s for horizontal resolutions 137
7.7 Time development of S for horizontal resolutions 138
7.8 $\bar{u}$ and s for horizontal resolutions 141

Publications

Lewis, S. R; **Dawson, J.**; Read, P. L.; Yamamoto, M. (2012) *International modeling efforts and historical background*, in Bengtsson, L. (ed.), Towards Understanding the Climate of Venus: Application of Terrestrial Models to Our Sister Planet, Springer Science, New York, 2013.

Lebonnois, S.; Lee, C.; Yamamoto, M.; Lee, C; **Dawson, J.**; Lewis, S. R.; Mendonça, J.; Read, P. L.; Parish, H.; Schubert, G.; Bengtsson, L.; Grinspoon, D.; Limaye, S.; Schmidt, H.; Svedhem, H.; Titov, D. (2012) *A comparative analysis of simplified general circulation models of Venus atmosphere*, in Bengtsson, L. (ed.), Towards Understanding the Climate of Venus: Application of Terrestrial Models to Our Sister Planet, Springer Science, New York, 2013.

Lewis, S. R.; **Dawson, J.**; Read, P. L.; Mendonça, J.; Ruan, T. and Montabone, L. (2012). *Super-rotating jets in the atmospheres of terrestrial planets.* In: Comparative Climatology of Terrestrial Planets , 25-28 June 2012, Boulder, Co, USA.

Lebonnois, S.; Lee, C.; Yamamoto, M.; **Dawson, J.**; Lewis, S. R.; Mendonça, J.; Read, P. L. and Parish, H. (2011). *Weakly forced atmospheric GCMs : lessons from model comparisons.* In: EPSC-DPS Joint Meeting 2011, 2-7 October 2011, Nantes.

Lewis, S.; Lebonnois, S.; Covey, C.; **Dawson, J.**; Lee, C.; Parish, H.; Read, P. L.; Schubert, G.; Yamamoto, M.; Bengtsson, L.; Grinspoon, D.; Limaye, S.; Schmidt, H.; Svedhem, H. and Titov, D. (2010). *A comparative analysis of Simplified General Circulation Models of the atmosphere of Venus.* In: European Planetary Science Congress, 19-24 Sep 2010, Rome, Italy.

Dawson, J.; Lewis, S. R. (2014). *Thermal forcing and static stability with a T21 GCM for Venus.* In preparation.

Lewis, S. R.; **Dawson, J.** (2014). *Horizontal and vertical resolution in a T21 GCM for Venus.* In preparation.

Chapter 1

Introduction

1.1 Venus

Venus is often called the morning or evening star, because it reaches maximum brightness at those times. The planet is one of the four innermost orbiting, rocky, terrestrial planets (Mercury, Venus, Earth and Mars) and one of four terrestrial planetary bodies in the solar system with an atmosphere (Venus, Earth, Mars and Titan). It is the second planet from the Sun and the near twin of the Earth in terms of size, mass and composition. Named after the Roman goddess of love, Venus is the only planet[1] in the solar system named after a female figure.

Observed since the beginning of astronomy, Venus was originally known in the West as 'the wandering star'. Pythagoras (c. 500 BC) is credited with realising that the morning and evening stars were, in fact, the same body. Galileo observed Venus using his newly invented telescope in the 17th century and argued that Venus orbited the Sun, and not the Earth[2], due to his observations of phases similar to those of the moon.

[1] Not including dwarf planets

[2] Galileo was later excommunicated for his heliocentric views

Venus orbits the Sun at an average distance of 108M km (~0.72 AU). Its orbital period, a Venusian year, is ~225 Earth days long and it rotates on its axis, a Venusian sidereal day, once every 243 Earth days. The planetary rotation of Venus is retrograde, in that its rotation is clockwise when viewed from above the plane of the ecliptic, unlike every other planetary body in the solar system which rotates anti-clockwise.

The combination of rotation rate and orbital period gives a solar day on Venus of 116 Earth days, the retrograde rotation resulting in the Sun rising in the west and setting in the east.

Lack of knowledge about the Venusian atmosphere was historically responsible for much confusion regarding the rotation rate of the planet. Telescopic observations had revealed the complete cloud coverage and observations of the rotation of dark spots in the clouds are critiqued by Hussey (1832). In his paper Hussey (1832) provides details of the conclusions by scientists such as Cassini and Schröeter who determined the rotation period to be slightly above 23 hours. Bianchini asserted 23 days and 8 hours and Sir William Herschel favoured a period closer to 24 days.

The rotation of Venus was finally resolved accurately in 1961. With the use of radio telescopes, researchers at Jet Propulsion Laboratory (JPL) in California, Jodrell Bank in the UK and the Soviet deep space facility in Evpatoria used the Doppler effect to measure the rotation period to be 243 Earth days (Pettengill and Price, 1961). Further measurements at JPL showed the rotation to be retrograde.

1.2 Planetary and atmospheric parameters

Table 1.1 shows a summary of the planetary and atmospheric parameters for Venus, with data for Earth and Mars included for comparison. Notable differences between these three terrestrial planets include the relatively small values of both obliquity (-2.6°) and orbital eccentricity (0.0067) for Venus. One result of this is that seasonal effects are weak on Venus (although not entirely absent).

Table 1.1: Key Planetary and atmospheric parameters

	Venus	**Earth**	**Mars**
Mean orbital radius (10^{11} m)	1.08	1.50	2.28
Distance from Sun (AU)	0.67	0.98 - 1.02	1.38 - 1.67
Orbital eccentricity	0.0067	0.0167	0.093
Planetary obliquity	177.4°	23.45°	25.19°
Rotation rate, Ω (10^{-7} s^{-1})	2.993	729.4	708.8
Solar day (s)	10,087,200	86,400	88,775
Year length (Earth days)	224.70	365.24	686.98
Equatorial radius (10^6 m)	6.052	6.378	3.396
Surface gravity, g (m s^{-2})	8.87	9.81	3.72
Surface pressure (Pa)	9.32 $\times 10^6$	1.013 $\times 10^5$	600 (variable)
Atmospheric constituents (molar ratio)	CO_2 (96.5%) N_2 (3.5%)	N_2 (77%) O_2 (21 %) H_2O (1 %) Ar (0.9 %)	CO_2 (95 %) N_2 (2.7 %) Ar (1.6 %) O_2 (0.13 %)
Gas constant R (m^2 s^{-2} K^{-1})	188	287	192
C_p/R	4.5	3.5	4.4
Mean Solar Constant (W m^{-2})	2614	1367	589
Bond albedo	0.75	0.306	0.25
Equilibrium temperature, T_e (K)	232	256	210
Scale height, $H = RT_e/g$ (km)	15.9	7.5	10.8
Surface temperature (K)	737	230-315	140-290
Dry adiabatic lapse rate (K km^{-1})	10.5	9.8	4.5

1.3 Aims of this research

This document describes the processes performed to convert a spectral Global Circulation Model for Mars to one for Venus. A number of tests were performed with the model to investigate the model's sensitivity to various parameters and settings. The ultimate goal is to determine the optimum configuration of the model for use as a Venus Global Circulation Model.

Super-rotation, a circulation of the atmosphere faster than the planetary rotation, is a particular feature of the Venus atmosphere which rotates up to 60 times faster than the underlying planet. Super-rotation has been produced in a number of models and it is of importance that the model developed is able to reproduce this feature. The model should also produce super-rotation with realistic parameters.

However different models produce different super-rotation, hence it would be useful information to know how sensitive the model developed is to:

1. The model dynamics.
2. The horizontal and vertical resolution.
3. The model initial state.
4. The presence or absence of topography.
5. The precise form of the forcing function and associated background static stability profile.

To shed light on what drives the super-rotation in the model(s) tests should be performed to isolate large-scale wave processes by removing any thermal tide, and then to add a thermal tide to test the effect on the model output.

Among the wider questions that the model may help to answer include:

i) Informing about large-scale Venus dynamics.

ii) Informing about different models, with Venus as a testbed for model core validation.

1.4 Structure of this thesis

The structure of this document is as follows:

Chapter two provides an introduction to the Venusian atmosphere, and the atmospheric dynamics. At the beginning of the chapter some basic atmospheric parameters are given together with brief details of the history of the discovery of the atmosphere. A table of key atmospheric constituents is given and some details of the cloud layers. An explanation of the physics of the 'greenhouse' effect is followed by the details of the evolution of the atmosphere, circulation of the atmosphere and the features and waves seen in the clouds.

A definition for super-rotation is provided, which will be referred to in the later results chapters when diagnosing the winds. An example of the super-rotation calculation is shown.

Chapter three initially summarises the major theories proposed to explain the circulation observed in the Venusian atmosphere. This is followed by summaries of many of the modelling studies previously performed on the atmosphere of Venus. For each of these summaries details are given of the model used and the main results obtained by those models. Finally for this chapter a brief discussion is given of some of the future modelling efforts as suggested by the various authors of the more recent modelling studies.

Chapter four is concerned with the model used for this study. The history of the model, type of model, and model core are given before brief basic details of other common model types. There are many configuration settings which can be set in the model code for the planet and atmosphere to be modelled. This chapter describes the configuration of the model for use as a Venus GCM.

The radiative temperature state used by the model is described in detail. This is followed by the settings used for the experiments. The vertical level scheme is detailed as well as the sigma levels used for the experiments and the conversion between pressure and height.

Time-steps for the model and planetary rotation rate follow before a table of the main planetary parameters used when setting the model for Venus (table 4.1) is presented. Then details and justification for the restoration and friction timescales used are given, together with a brief discussion of those settings for restoration and friction timescales used previously by other researchers, with similar and different model types.

In chapter five the results obtained when the model was run for base (or reference) simulations are presented; these are runs which are used as reference simulations for subsequent experiments. Plots for the zonally averaged zonal wind ($\bar{u}$), local super-rotation index (s), atmospheric angular momentum (AAM), mean meridional circulation (MMC) and temperature difference from the mean temperature (the temperature anomaly, ΔT) are presented for the basic configurations of the model, both for the case with the sponge layer on eddies only and the sponge layer on all terms.

A section follows with existing details of the topography of Venus. The topographical data-set from the NASA Magellan satellite mission is introduced and its use to make a topographical data file for the model to use is described. The results obtained from the model when run using this data file are presented. The results are shown for the case of a sponge layer on eddy terms only. Plots for wind speed, local super-rotation index, mean meridional circulation and temperature anomaly are presented.

Chapter six presents the results obtained when using the model with a selection of different input temperatures, the 'modified background stability' (MBS) forcing states.

The effect of these input temperatures on the simulated winds, atmospheric circulation and global temperatures obtained is compared to the 'base' simulations. It is shown how the wind speed and super-rotation are enhanced by increasing the temperature forcing from the observed values.

This is followed by a section describing the changes made to allow the model to be run with the inclusion of a simple diurnal cycle. The zonal wind, mean meridional circulation and temperature anomaly obtained when the model was run with this diurnal cycle are presented.

In chapter seven the effect on the model output when changing the model resolution is described. First the results obtained, and the effect on the model output, when changing the vertical resolution. Results are shown for both an increased temperature and standard forcing state with the number of levels (NL) set to 32, 50, 100 and 200. The differences in wind and super-rotation index are compared for the four different NL's each with the two different temperature input states.

This is followed by varying the horizontal resolution. The horizontal resolution of the model is varied by changing the number of wave modes retained. The model was run at three resolutions, retaining 10, 21 and 42 wave modes, with the two forcing states tested with the vertical resolution. Results are shown for evolution of angular momentum, zonal wind and local super-rotation index.

The final chapter in this dissertation summarises the work done and the results obtained, and suggestions for future work are given.

There are many terms used in the following document. Where these occur, all such terms will be defined in context.

Chapter 2

The Venusian atmosphere

This chapter is an introduction to the Venusian atmosphere and its dynamics; it begins with the discovery of the atmosphere and some brief history of the development of theories concerning Venus and the conditions on the planet. The current atmospheric composition is listed in table 2.1, and details of the cloud layers, their heights and the wind speeds are given. The clouds are important on Venus for the atmospheric circulation, and the surface conditions. So to provide some background, details of the physics of the 'greenhouse' effect are given with example calculations. Temperature profiles for Venus and Earth (figure 2.4) are shown.

Later in the chapter, the evolution of the atmosphere, evidence for water loss and an equilibrium between the atmosphere and surface are presented leading to a possible explanation for the current atmospheric composition. The circulation of the atmosphere and a method for calculating atmospheric wind speeds is given before two diagrams of wind profiles are shown. The features seen in the Venus atmosphere such as the 'polar vortex' and the 'double eye' precede details of the types of waves and those seen in the atmosphere.

Finally for the chapter definitions for local and global super-rotation are given and an example calculation of global super-rotation with a specified wind field is shown.

2.1 The atmosphere of Venus

The atmosphere of Venus was first detected by Russian polymath Mikhail Lomonosov in 1761 (Marov, 2005). Lomonosov observed the refraction of solar rays during a transit of Venus across the disk of the Sun and correctly inferred that only refraction by an atmosphere could explain the appearance of a light ring (or fire ring) around the part of Venus that had not yet come in contact with the Sun's disk during the initial phase of the transit.

Venus was known to have a high albedo (reflectivity of sunlight) due to the thick cloud covering. The albedo of 0.76, two and a half times that of Earth, was once thought to offset the increase in the solar constant (compared to Earth) due to Venus being closer to the Sun. Thus the planetary surface would receive and absorb less of the greater radiant energy from the Sun (insolation) and therefore the surface temperature could be expected to be similar to that of Earth. The popular vision was of a planet with oceans and steamy jungles. When the atmosphere was shown by Adams and Dunham in 1934 to be composed mainly of CO_2 (97%) the idea that soda water oceans existed became popular (Taylor, 2006).

At the beginning of the space era (Sputnik was launched by the U.S.S.R. in 1957) it became possible to estimate the surface temperature of Venus using Earth based radio telescopes to measure the emitted microwave radiation. At wavelengths of a few centimetres, radiation from the planet's surface passes through the cloud layers with little attenuation and can be picked up on Earth. Early results for Venus suggested a surface temperature of approximately 670K. It was not until the Soviet 'Venera' series of spacecraft made the first landings on the planetary surface that the surface temperature and pressure were accurately measured (Venera 7, 1970). It is now known that the Venusian surface temperature is $\sim$735K, and its surface pressure is 92 times that of Earth and the atmosphere comprises mainly CO_2 (97%) with thick clouds of sulphuric acid (H_2SO_4) (Svedhem et al., 2007).

2.2 Current atmospheric structure

Table 2.1 summarises the basic composition of the Venusian atmosphere below the cloud level.

Table 2.1: Basic components of the Venus atmosphere near the surface.
Mixing ratio in % or parts per million (ppm), from Taylor (2006)

Composition (near surface)	**Species**	**Mixing ratio**
Major	CO_2	96.5 %
	N_2	3.5 %
Minor	SO_2	150 ppm
	Ar	70 ppm
	H_2O	20 ppm
	CO	17 ppm
	He	12 ppm
	Ne	7 ppm

The main cloud deck extends from about 70 km down to about 45 km, with associated thick haze layers above and below. The visibility in the clouds is quite good by Earth standards with an average visibility of several kilometers. (Mills et al., 2007). Within the clouds detailed layering occurs, with particles of different sizes and different gas species congregating at different height layers.

Figure 2.1 shows the cloud layers in the Venusian atmosphere together with an indication of the wind speeds at various heights. Also shown are the observational techniques used to obtain the data. Although the cloud layers are much higher than clouds found on Earth, the temperature and pressures at the cloud levels are similar for both planets (see figure 2.4).

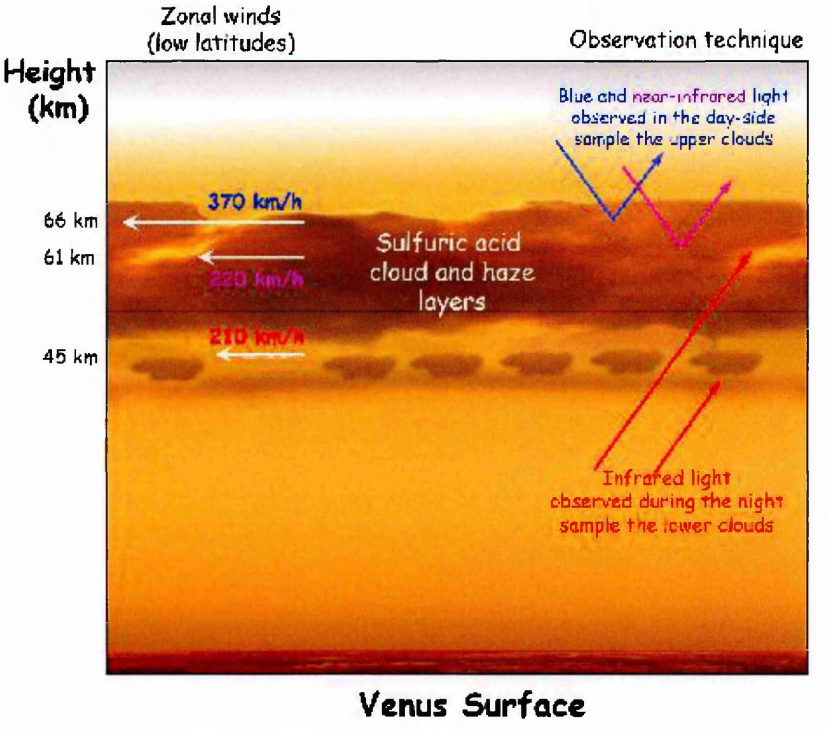

Figure 2.1: Cloud layers and wind speeds
Graphic from: http://www.esa.int/esaMI/Venus_Express/SEMZG6Q4KKF_1.html

2.2.1 The greenhouse effect

The incident radiation from the Sun is predominantly short wave, which heats the planet's surface. The planet then re-emits this radiation as long wave, infra-red radiation. The 'radiative equilibrium' of the planet can be expressed as follows:

The total radiant power of the Sun is given by:

$$E_{\text{sun}} = 4\pi\sigma R_{\text{sun}}^2 (T_{\text{sun}})^4 \tag{2.1}$$

where σ is the Stefan-Boltzmann constant = 5.670 x 10^{-8} W m $^{-2}$ K $^{-4}$

The solar constant, S, is then given by:

$$S = \sigma T_{\text{sun}}^4 (R_{\text{sun}}/D_{\text{sun}})^2 \tag{2.2}$$

where D_{sun} is the planet's distance from the Sun in AU.

So for equilibrium:

$$E_{\mathrm{E}} = 4\pi\sigma R_P^2 (T_{\mathrm{E}})^4 = (1 - A) S \pi R_P^2 \tag{2.3}$$

where: σ is the Stefan-Boltzmann constant

R_P is the planetary radius

A is the albedo (the amount of insolation reflected back into space)

S is the energy received from the Sun.

and T_{E} is the Effective Temperature of the planet

and hence the radiative equilibrium temperature for the planet, T_{E}, can be calculated given the albedo, A.

The calculation of the effective temperature for Venus, which is the equivalent black-body temperature at which the planet radiates heat back into space, gives a figure of 229K which is considerably less than the actual surface temperature of 735K. For Earth the effective temperature is calculated to be 255K, also much less than the actual surface temperature of 288K. The higher surface temperature for both planets is due to the atmosphere 'trapping' some of the outgoing long wave radiation.

An atmosphere is generally transparent to the incoming short wave radiation (optically thin) but highly absorbent of the outgoing infra-red radiation (optically thick) due to absorption by atmospheric gases such as water vapour and carbon dioxide. This absorption and re-radiation at a lower temperature is known as the *greenhouse effect* and results in a surface temperature higher than the planet would have in the absence of an atmosphere.

The graphic, figure 2.2, shows the different components of radiative energy fluxes for Venus and Earth, taking the solar irradiance at Venus as 100%. An indication of the proportion of energy absorbed by various parts of each planet and atmosphere are also shown (from Taylor and Grinspoon, 2009).

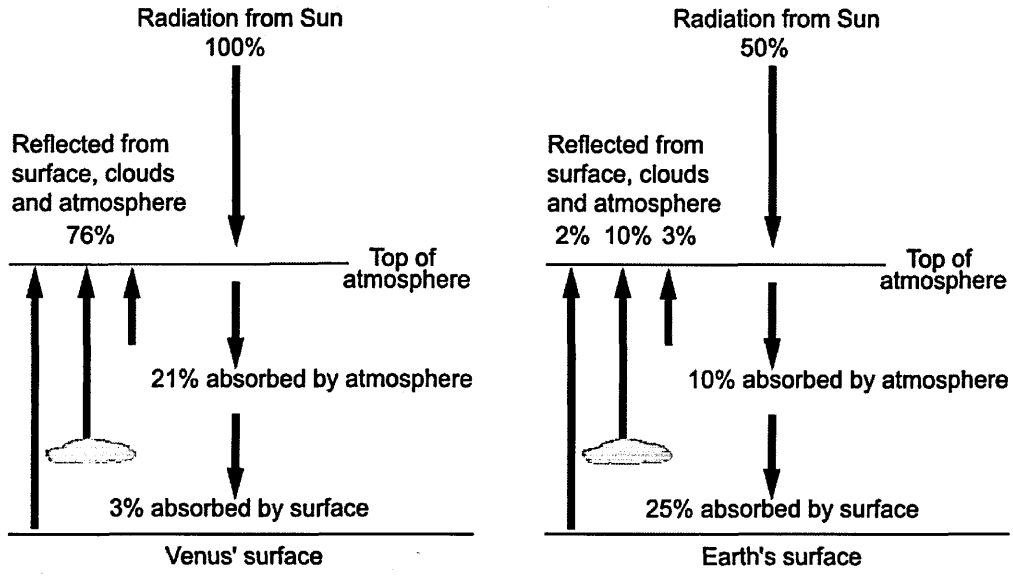

Figure 2.2: The radiative energy fluxes for Venus and Earth, solar irradiance at Venus shown as 100% (from Taylor and Grinspoon, 2009).

A simple model of an atmosphere

At its simplest the heating effect of an atmosphere can be modelled by assuming a planet has a thin atmosphere, at uniform temperature, which is optically thin to the incoming short wave radiation and optically thick to the outgoing long wave radiation (Andrews, 2000). Assuming the atmosphere is at the effective temperature of the planet, the 'greenhouse effect' can be expressed as:

$$T_{\mathrm{Surf}} = 2^{1/4} T_{\mathrm{E}} \tag{2.4}$$

where T_{Surf} is the surface temperature and T_{E} is the radiative equilibrium temperature calculated with equation 2.3.

Using this simple model to calculate the surface temperature gives 272K for Venus and 291K for Earth. This simple model is clearly inadequate for Venus with an actual surface temperature of 735K; however the temperature for Earth is quite close to the true value of 288K.

A more refined model atmosphere

Results which match the observed and measured temperature values can be obtained by using only simple refinements to this model (Andrews, 2000; Taylor, 2006). The model atmosphere is divided into two regions, optically thick nearest the surface (the troposphere) and an optically thin region above (the stratosphere). In the troposphere convection processes dominate, and convective equilibrium is assumed. In the stratosphere radiation transports the majority of heat, and radiative equilibrium is assumed. With the additional assumptions of a constant temperature gradient in the troposphere, which is assumed to be marginally stable at the dry adiabatic lapse rate, and a constant lapse rate in the stratosphere of zero, the model atmosphere can now be specified by just three parameters; surface temperature, tropospheric lapse rate and stratospheric temperature.

In formulating this model the perfect gas law, the first law of thermodynamics and the hydrostatic equation are used to obtain the vertical temperature gradient in the troposphere. The stratospheric temperature is assumed to be constant with height and is related to the effective temperature by:

$$T_{\text{Strat}} = \frac{T_{\text{E}}}{2^{1/4}} \tag{2.5}$$

The height of the tropopause (where the stratosphere begins and the convective and radiative transfer schemes change over) can be calculated from radiative transfer theory or estimated using any of a range of approximation methods (e.g. Goody and Yung, 1989).

Calculating the temperature where the emission of IR radiation to space balances the incoming insolation flux using this simple model atmosphere results in the vertical profiles shown in figure 2.3. The surface temperature for Venus is now slightly above 700K. For both Venus and Earth this model gives a good approximation of the surface and atmospheric temperatures.

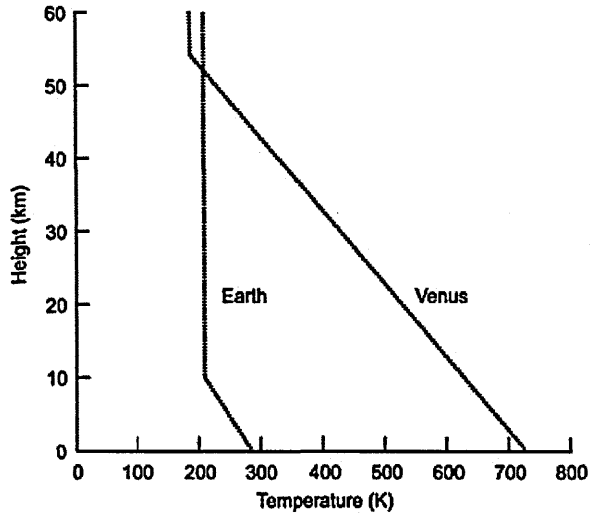

Figure 2.3: The mean temperature profiles calculated for Venus and Earth. Adapted from Taylor (2006).

Figure 2.4 shows the measured temperature profiles for Venus and Earth. The atmosphere of Venus is much thicker than that of Earth and the clouds on Venus are at a much higher altitude although the temperatures and pressures at the cloud levels are quite similar for both planets.

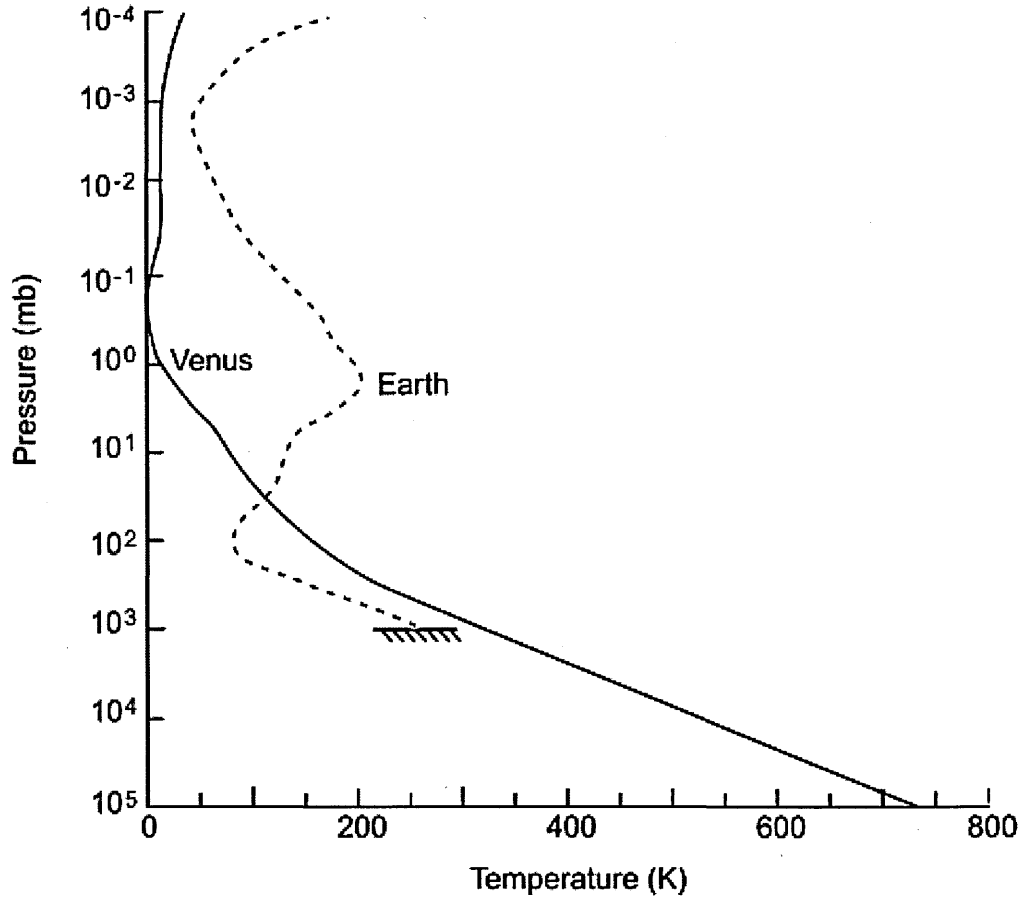

Figure 2.4: Measured temperature profiles for Venus and the Earth, where the vertical scale is in millibars (1 mb = 100 Pa). The solid line is derived from remote sounding measurements made by the Pioneer Venus Orbiter Infrared Radiometer and extrapolated assuming a dry adiabatic lapse rate below 500 mb; the dashed profile is from measurements by the Improved Stratospheric Sounder on the Upper Atmosphere Research Satellite (from Taylor and Grinspoon, 2009).

2.3 Evolution of the Venusian atmosphere

Venus, Earth and Mars are all believed to have formed at approximately the same time, as collisions between planetesimals that grew by accreting gases and dust from the solar nebula after the Sun had formed. Venus and Earth should have started with similar proportions of water (and other volatiles) during this process, and another important source of water may have been the heavy bombardment of comet-like objects arriving towards the end of the accretionary period (Ip and Fernandez, 1988). Since formation, the atmospheric evolution for each of these planets has been very different.

Venus is now a very dry planet and the water which is present is enriched in deuterium to approximately 150 times the terrestrial value (de Bergh et al., 2006). This suggests that Venus has lost most of its water, as the processes for hydrogen isotope escape discriminate strongly against the loss of deuterium leading to deuterium enrichment. Radiative-convective models of the early Venus atmosphere show the increasing greenhouse effect driving H_2O into the upper atmosphere where solar UV photons disassociate the H_2O molecules allowing the lighter hydrogen to escape into space. This hydrodynamic escape mechanism is rapid enough to remove a large ocean in less than 600 million years (Kasting, 1988).

When Venus formed the Sun was 30% cooler than at present. Venus is thought to have possessed deep water oceans during the time when the Sun began to heat up and its radiant power increased. The increase in insolation would have raised the surface temperature, and due to evaporation from the oceans the amount of atmospheric water vapour would have increased. Water vapour is a strong greenhouse gas therefore further increasing the temperature and driving yet more water vapour into the atmosphere. This feedback loop eventually boiled off all the surface water, which disassociated into H_2 and O in the upper atmosphere and the H_2 escaped into space.

Without oceans Venus could not have a water based carbon cycle as on Earth, where the majority of the carbon is locked in crustal rocks and the oceans. Hence despite Venus and Earth now possessing similar amounts of CO_2 (Svedhem et al., 2007), the CO_2 on Venus is mainly contained in the atmosphere. This 'runaway greenhouse effect' and the evolution of the Venusian atmosphere is of current interest to terrestrial climate change as this could be the ultimate fate for the Earth.

A possible explanation for the high CO_2 concentration in the atmosphere and therefore the high surface temperature and pressure on Venus was suggested by Urey (1961), and involves the chemical equilibrium between the atmospheric carbon dioxide and carbonate and silicate materials in the crust.
The reaction:

$$CaCO_3 + SiO_2 \rightleftarrows CaSiO_3 + CO_2$$

reaches equilibrium with CO_2 at temperatures and pressures typical of Venus, so may offer an explanation for the extreme climate. However, among the many questions unresolved is how such a mechanism would operate in practice (Taylor, 2006).

2.4 Circulation of the Venusian atmosphere

By the early 1960's ultraviolet images of Venus had been taken, revealing features in the clouds not apparent from visible wavelength observations. In particular a Y-shaped feature was observed (sometimes described as 'the ψ feature'), shown in figure 2.5, which rotates around the planet with a period of 4-5 Earth days (Edays) (Taylor, 2006).

This rotation of the Y-feature implied a wind velocity of $\sim$100 $\mathrm{m\,s^{-1}}$ at the cloud tops, despite the solid surface which rotates at about 2 $\mathrm{m\,s^{-1}}$ (at the equator). The wind speeds were confirmed and measured more accurately by the space probes visit-

Figure 2.5: Pioneer Venus IR image of the Y-feature

ing Venus and also by Earth based measurements. The zonal flow at low latitudes is over 100 $\mathrm{m\,s^{-1}}$ at the cloud tops, which are at approximately 70 km altitude; i.e. the 50 mb pressure level (Gierasch et al., 1997). Thus Venus' atmosphere takes ~4 Edays to rotate, approximately 60 times faster than the underlying planet. This atmospheric rotation is known as Retrograde Super-rotating Zonal flow (RSZ).

Images of the clouds can be used to track features in the clouds over short periods thus allowing the cloud top wind speeds to be calculated. Peralta et al. (2007) present latitudinal profiles of cloud tracked winds, at two cloud levels, from images obtained by the Galileo spacecraft flyby during February 1990. For this analysis Peralta et al. (2007) used images obtained at two wavelengths, 418 nm (ultraviolet) and 986 nm (near-infrared (NIR)), representing two different altitude levels in the clouds. The 418 nm images are at approximately 65–70 km (the cloud tops) and the 986 nm images below that.

The plot shown in figure 2.6 shows the zonal wind velocity as a function of latitude from this data. From the cloud top data it can be seen the zonal wind velocity is approximately 100 $\mathrm{m\,s^{-1}}$ at equatorial latitudes, decreasing significantly above ~45° in

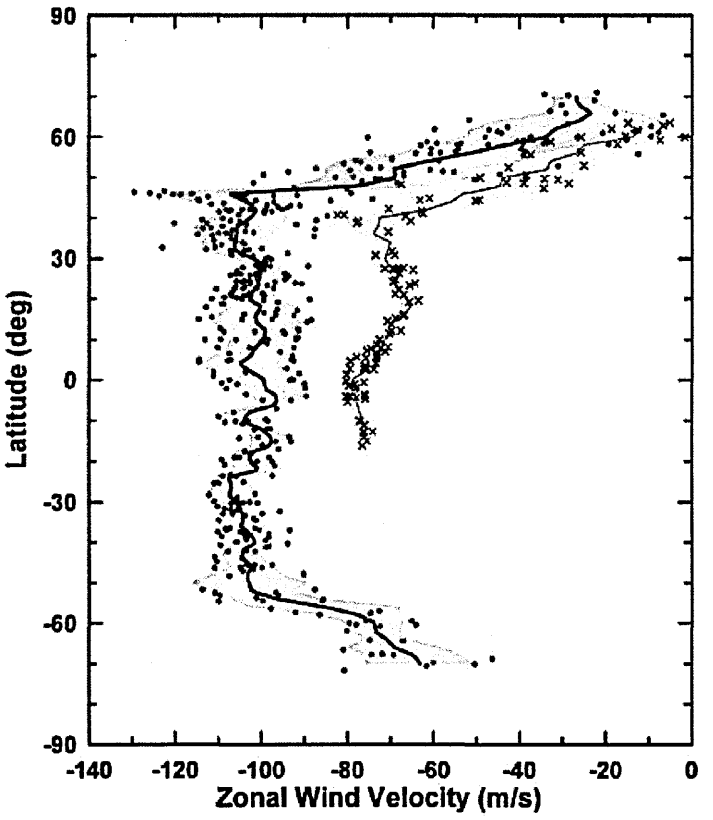

Figure 2.6: Venus zonal winds measured from cloud tracking with Galileo images. Measurements in the ultraviolet and NIR appear as black circles and crosses respectively. Binned profiles to the data are shown with a dark and a lighter continuous line. Uncertainties over the fit are shown with the shaded region. From Peralta et al. (2007)

the northern hemisphere and $\sim 50°$ in the southern hemisphere.

Sánchez-Lavega et al. (2008) used data from the Venus Express (VEx) satellite which arrived at Venus in April 2006, to calculate the zonal winds at the cloud tops. VEx's elliptical orbit achieved perigee close to the South Pole. Hence the most detailed observations were made of the southern hemisphere and the VIRTIS spectrometer carried allowed the winds to be calculated at 3 altitudes; the upper clouds at ~ 66 km and ~ 61 km, and lower clouds at ~ 47 km. A plot of the wind profiles is shown in figure 2.7.

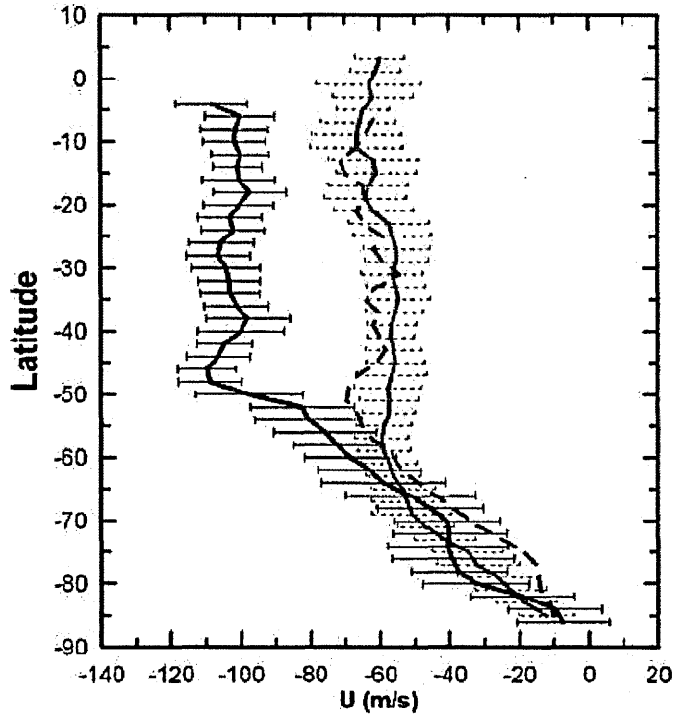

Figure 2.7: Averaged wind profiles in Venus' southern hemisphere at cloud level (April 2006 July 2007). The zonal velocity is drawn as a function of latitude as measured using cloud tracers at three wavelengths: ultraviolet (blue, 380 nm; upper cloud, altitude ~66 km; day time), near-infrared (violet, 980 nm; upper cloud, altitude ~61 km; day time), and infrared (red, 1.74 mm; lower cloud, altitude ~47 km; night time). From Sánchez-Lavega et al. (2008)

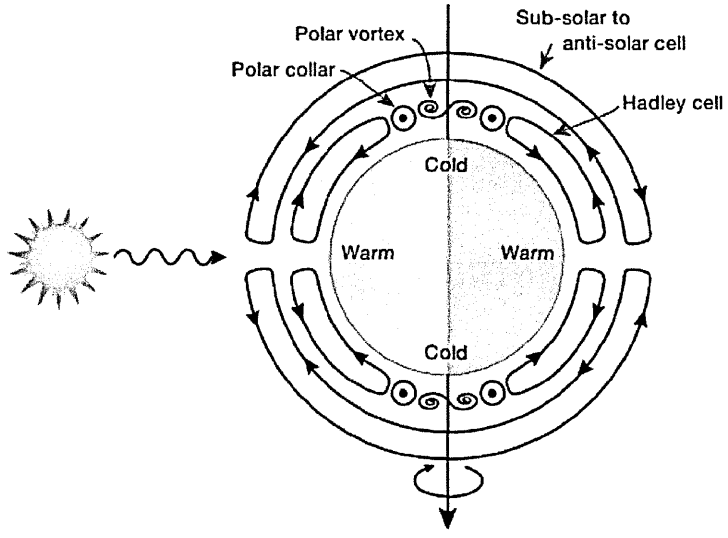

Figure 2.8: Schematic of the possible Venus atmospheric circulations. From Svedhem et al. (2007)

2.5 Features and waves seen in the atmosphere

Early observations by VEx at high resolution (Svedhem et al., 2007) have revealed more detailed information on the overall atmospheric circulation. Figure 2.8 shows a schematic view of the possible circulations. Here the atmospheric dynamics of Venus can be divided into two broad regimes: the retrograde zonal super-rotation in the troposphere and mesosphere (the middle and lower atmosphere) (Gierasch et al., 1997) and the solar-antisolar circulation across the terminator in the thermosphere above (Bougher et al., 1997).

Three regimes are present in the troposphere and mesosphere (the middle and lower atmosphere): the Hadley circulation with convective and wave dominated flow at lower latitudes; the cold polar collar and the enclosed vast vortex like feature with a revolving 'double eye', that rotates every 2.5 – 2.8 Edays (Svedhem et al., 2007).

The polar vortex and revolving dipole (the 'double eye') are intriguing features in

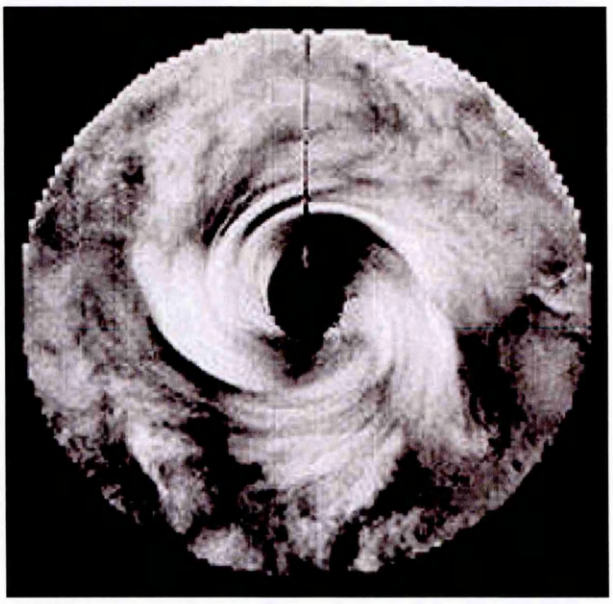

Figure 2.9: Image of polar vortex - from Pioneer Venus

the atmosphere of Venus. The polar vortices are large cyclonic structures surrounding the poles, several thousands of kilometers across (Svedhem et al., 2007). Pioneer Venus observed a region of cool air surrounding a higher temperature polar cap, the 'polar cold collar', and a large vortex inside this 'cold collar' (Taylor et al., 1980). The south polar vortex was imaged by the Pioneer Venus Orbiter (PVO). Figure 2.9 shows an UV image of this feature. It is thought that the vortices contribute to the momentum transfer in the polar regions, possibly by transferring zonal momentum down to the lower atmosphere (Taylor et al., 1980).

More detailed images of the polar regions show the double-eye, the dipole feature inside the cold collar. Figure 2.10 shows a composite IR and UV image of the south polar region, from VEx observations, clearly showing the cold collar and the double-eye.

Waves are ubiquitous in planetary atmospheres and play an important role in the circulation of the most studied atmosphere, that of Earth. Gravity waves are disturbances for which the restoring force is buoyancy. They are generated in many different

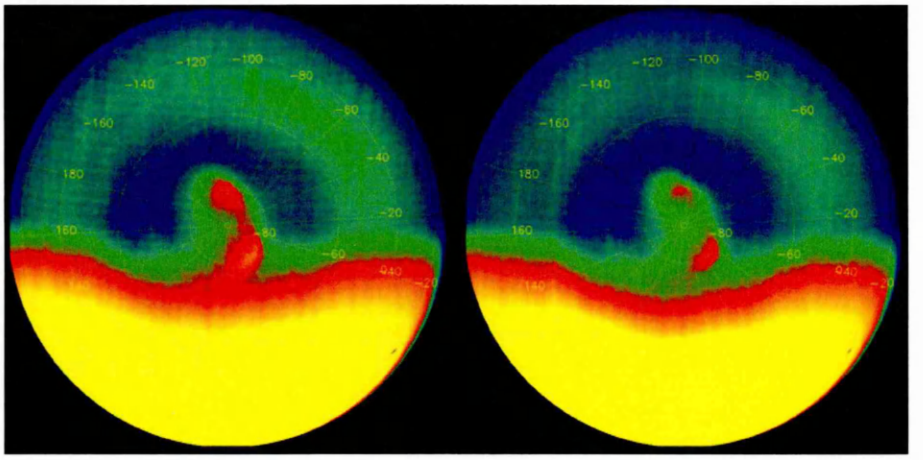

Figure 2.10: Image of double eye
(Copyright: ESA/VIRTIS/INAF-IASF/Obs. de Paris-LESIA)

ways, including by flow over topography and by convective activity in the troposphere. Young et al. (1987) report that gravity waves, perhaps generated by topography, may have been detected by the VEGA balloons during their missions many years ago. Waves generated in the lower atmosphere may propagate vertically, whereas the atmospheric density decreases the amplitudes of the wave fluctuations (in wind, temperature and density) will increase. Inertia-gravity waves are a type of gravity wave with horizontal wavelengths of hundreds of kilometres and periods of several hours (Andrews, 2000).

Another type of wave observed in atmospheres, with horizontal scales of thousands of kilometres and periods of several Earth days are known as Rossby waves or planetary waves. These waves are however difficult to identify unambiguously since purely sinusoidal Rossby-waves can only exist in very simple background flows (Andrews, 2000).

Kelvin waves are a type of gravity wave which are trapped at the equator. Kelvin waves are also observed on horizontal scales of thousands of kilometres and periods of several Earth days.

Waves have been detected in the atmosphere of Venus with VEx observations in

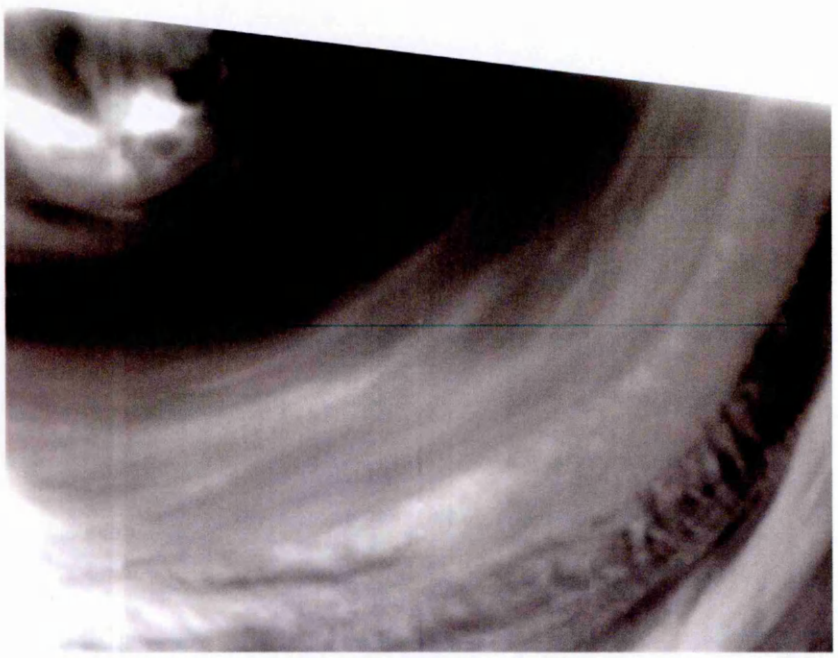

Figure 2.11: Wave patterns in the clouds of Venus
(Copyright: ESA/VIRTIS/INAF-IASF/Obs. de Paris-LESIA)

the IR and UV showing significant wave activity. Figure 2.11 shows an image of the southern hemisphere of Venus taken at 1.7 μm (IR). In this image a remarkable wave structure is evident. Running from the bottom to the top right a band with many 'waves' can be seen, each 'wave' extending about 150 km. This feature is seen at a latitude of $\sim$55°S; the South pole and part of the polar vortex can be seen as the bright area in the top left corner. Between the black stripe around the pole and the wave structure is the cold-collar.

Images of the clouds can be used to track features seen in the clouds allowing the period of waves and cloud top wind speeds to be calculated. Ultra-violet images of the cloud tops were taken by the PVO Cloud Photopolarimeter (OCPP) spanning 1979 to 1986 and used by del Genio and Rossow (1990) to derive the period and types of the waves seen in the clouds. del Genio and Rossow (1990) used data on the variation of brightness of UV features to identify at least four planetary scale wave modes. Tracking the motion of the Y feature revealed an equatorial 4-Eday wave and a five-Eday wave in mid-latitudes. Also identified were solar-locked diurnal and semi-diurnal tidal modes present in both UV brightness and cloud-tracked wind data.

Although tracking of the features seen in Ultra-Violet images of the atmosphere of Venus is a useful technique, the nature of the UV absorber responsible for those features is currently unknown.

More recently the wind speeds within the cloud layers have been mapped in 3 dimensions, by tracking clouds using data from the VIRTIS instrument carried on VEx (Sánchez-Lavega et al., 2008, see figure 2.7) . The measured wind speeds show that the zonal winds in the Southern hemisphere are nearly constant with latitude, with westward velocities of 105 $\mathrm{m\,s^{-1}}$ at the cloud tops and 60-70 $\mathrm{m\,s^{-1}}$ at the cloud base. At high latitudes the zonal winds decrease linearly with increasing latitude. Meridional winds at the cloud tops are poleward, with a peak speed of 10 $\mathrm{m\,s^{-1}}$ at 55° and below the clouds less than 5 $\mathrm{m\,s^{-1}}$ when averaged over the Southern hemisphere.

All of the zonal winds are westward, in the same direction as the planetary rotation. Suggestions to perhaps explain this direction for the circulation include angular momentum being supplied to the atmosphere by the solid body of the planet and transported upwards, and the Sun exerting a torque on the atmosphere and thus supplying the angular momentum (Taylor, 2006).

2.6 Super-rotation

Super-rotation is common in atmospheres, particularly for planets with slow rotation rates. A definition for super-rotation can be given by considering the excess specific angular momentum present in an atmosphere (Read, 1986a,b; Lewis and Read, 2003). The planetary angular momentum per unit mass is defined as the angular momentum a parcel of air (or atmosphere) would have when at rest at the equator:

$$M_o = \Omega a^2 \tag{2.6}$$

where a is the planetary radius, and Ω the angular velocity.

If $\bar{u}$ is the longitudinally averaged zonal wind speed at a latitude ϕ, then the angular momentum for this wind is given by:

$$m = a\cos\phi(\Omega a\cos\phi + \bar{u}) \tag{2.7}$$

A local super-rotation value, s, can now be defined as the ratio of the excess angular momentum, $m - M_o$, and the angular momentum, per unit mass, at the equator M_o. The local super-rotation value is then given by:

$$s = \frac{m - M_o}{M_o} \tag{2.8}$$

With this definition a value of $s > 0$ indicates excess angular momentum is present in the atmosphere and there is *super-rotation.*

The *globally* integrated super-rotation, S, is given by the ratio of the angular momentum of the westward winds to the integrated angular momentum when the winds are zero, M_a (Lewis and Read, 2003). The globally integrated angular momentum is:

$$S = \frac{\int_{P_0}^{0}\int_{0}^{2\pi}\int_{-\pi}^{\pi} ma^2\cos\phi\,\mathrm{d}\phi\,\mathrm{d}\lambda\,\mathrm{d}p/g}{M_a} - 1 \tag{2.9}$$

where λ is the planetary longitude, p the pressure, and P_0 the surface pressure.

The angular momentum of the atmosphere at rest with respect to the surface, M_a in equation 2.9, is given by:

$$M_a = \int_{P_0}^{0}\int_{0}^{2\pi}\int_{-\pi}^{\pi} \Omega(a\cos\phi)^2 a^2\cos\phi\,\mathrm{d}\phi\,\mathrm{d}\lambda\,\mathrm{d}p/g \tag{2.10}$$

If the globally integrated angular momentum is greater than the angular momentum of an atmosphere in solid body rotation with the planetary surface, i.e if $S > 0$, the

atmosphere is said to have *global super-rotation.*

The atmosphere of Venus has a global super-rotation value of ~ 10 (Read (1986a) from measured winds (Schubert, 1983)), with an atmospheric rotation approximately 60 times the equatorial speed of the underlying planet. Super-rotation has been observed in many planetary atmospheres (Mayr and Harris, 1983). Earth and Mars both show a slight super-rotation (~ 0.05), whereas Titan, Saturn's largest moon, shows significant super-rotation and like Venus also has a thick atmosphere and a slow rotation rate.

On Venus the velocity of the RSZ (Retrograde Super-rotating Zonal wind) varies considerably with height. Above the clouds the flow is decelerated sharply by the pressure gradient resulting from the temperature distribution (Taylor, 2006). Below the clouds the velocity also slows with decreasing height. Doppler tracking of the Pioneer Venus probes indicated a wind speed of $\sim$10 m s^{-1} at the 10 km level, reducing to close to zero at the surface.

2.6.1 An example of a super-rotation calculation

The global super-rotation can be estimated by using equation 2.9 and some simple assumptions for the wind speeds used in equation 2.7. For this example calculation a basic wind profile was set assuming the equatorial cloud top zonal wind speed was 100 m s^{-1} at 65 km altitude, decreasing steadily to zero at the surface, and decreasing above the clouds. The profile for $\bar{u}$ is assumed to be constant between $\pm 50°$, decreasing to zero at the poles. The plot in figure 2.12 shows graphically the assumed wind for latitude and height.

With this example wind profile, S was calculated to be 12, consistent with the estimate of ~ 10 made by Read (1986a) from measured winds (Schubert, 1983).

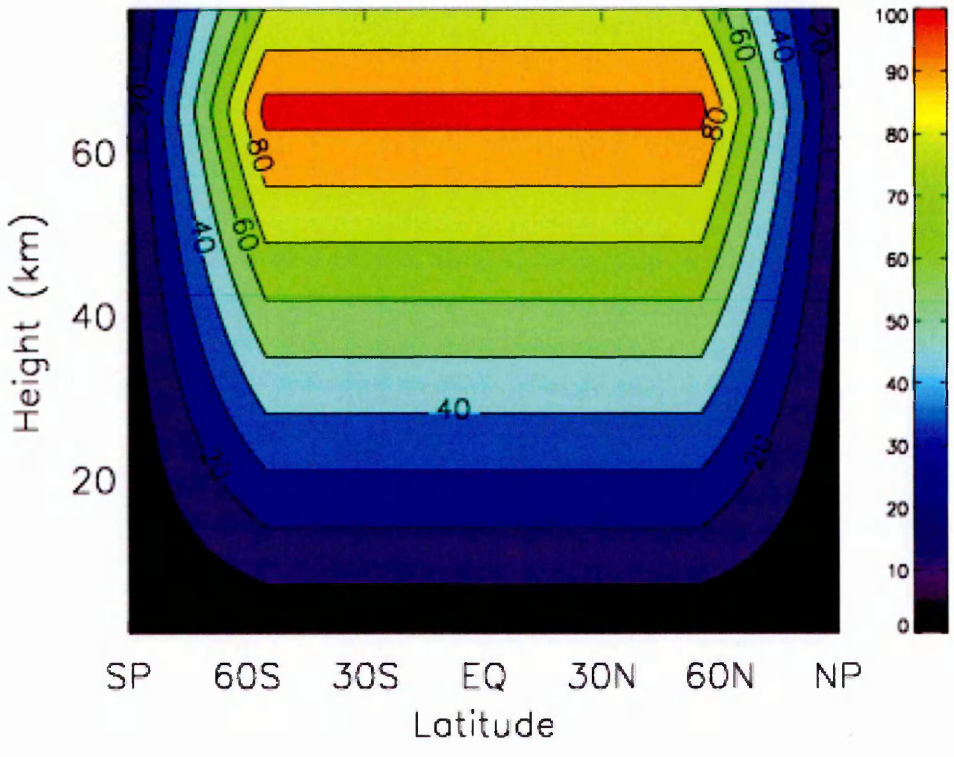

Figure 2.12: $\bar{u}$ profile used for example S calculation

2.7 Summary

In this chapter the discovery of the Venusian atmosphere and some historical details of the development of theories concerning Venus and the current conditions on the planet have been summarised.

The current composition was given in table 2.1. Details of the cloud layers, their heights and windspeeds were shown in graphical form in figure 2.1.

The physics of the 'greenhouse' effect were given, with examples of simple models of atmospheres, example calculations and then measured temperature profiles for both Venus and Earth (figure 2.4) showing the applicability of simple models to the 'real' atmospheres.

The evolution of the Venusian atmosphere was presented with discussion of evidence for water loss and a possible equilibrium between the atmosphere and surface, leading to a possible explanation for the current atmospheric composition.

The circulation of the Venus atmosphere followed and a method for calculating atmospheric wind speeds by tracking features seen in the clouds was given before two diagrams of wind profiles generated from cloud tracking data (from the Galileo and VEx satellites) were presented.

A schematic of the possible Venus atmospheric circulations from Svedhem et al. (2007) showing the Hadley cells, polar vortexes and polar collars in the middle and lower atmosphere (troposphere and mesosphere) with the sub-solar to anti-solar circulation in the thermosphere above them was shown in figure 2.8.

The features seen in Venus' atmosphere such as the 'polar vortex' and the 'double eye' were shown before details of some of the types of waves seen in atmospheres. Waves seen in the atmosphere of Venus were discussed with an image from VEx.

Super-rotation was defined by considering angular momentum in the atmosphere, definitions for both local and global super-rotation indexes were given (s and S), definitions that will be used to diagnose the model winds in the following results chapters. An example calculation of global super-rotation S was shown, using a specified wind field with wind speeds peaking at $100\,\mathrm{m\,s^{-1}}$ at the cloud top level.

Chapter 3

Previous studies of Venusian atmosphere dynamics

This chapter is devoted to previous modelling studies of the atmosphere of Venus. Commencing with brief descriptions of Hide's 1969 theorem, the experiment to explain super-rotation by Schubert and Whitehead (1969), the mechanism suggested by Gierasch (1975) and the Hadley circulation theory of Held and Hou (1980), which have been used and tested by many researchers in later years. This is followed by brief descriptions and summaries of the one and two-dimensional models used by a number of research groups up to the 1978 Pioneer spacecraft's arrival at Venus.

Following Pioneer Venus, increasingly sophisticated three-dimensional models become common. Many of these models are described and for each model a description of the model's intended use is given and the main results obtained from that model presented.

Andrews (2000) hierarchy of models suitable for understanding large-scale atmospheric dynamics places Global Circulation Models (GCMs), often referred to as Global Models, at the top as they are the most sophisticated. These models solve the primitive equations of fluid motion on a spherical grid, including Newton's laws, the hydrostatic equations and the ideal gas law.

The GCMs for Earth's climate have been under development for many years (Donner and Large, 2008) and good results can now be obtained from them, with increasingly accurate predictions of weather patterns, oceanic circulations and longer term climate effects now available. The circulation models need to be fine tuned for each planet, to take account of the differing atmospheric structures, and in the case of the terrestrial planets the lack of oceans on Mars and Venus. The models for Mars (e.g. Haberle et al., 1993; Forget et al., 1999; Lewis et al., 1999) are now beginning to be able to offer predictions of weather and climate phenomena, however those for Venus remain quantitative with some fundamental questions, such as the mechanisms for the super-rotation, unanswered.

3.1 Background to modelling studies

3.1.1 Hide's theorem

In order for the atmosphere of a planet to have a positive global super-rotation, the integrated angular momentum must be greater than that of a stationary atmosphere. According to Hide (1969), in the absence of viscous effects, non-axisymmetric pressure gradients and magnetic fields, the specific angular momentum is a conserved quantity following the motion of the fluid (Read, 1986a). In this case, angular momentum can only be re-distributed by the mean circulation, or created and destroyed by interaction with the surface. Hide (1969) shows that an equatorial maximum cannot be created by axisymmetric processes (e.g. Hadley circulation) alone, unless super-rotation was its initial condition. Further, the axisymmetric processes cannot alone counter the decelerating effect of friction.

3.1.2 Moving flame

An early idea to attempt to explain super-rotation was the 'moving flame' experiment of Schubert and Whitehead (1969). Following an experiment by Riehl and Fultz

(1958), an experiment with potential implications for Venus was carried out by Schubert and Whitehead (1969) with a cylindrical annulus of Mercury heated from below by a rotating Bunsen burner. The rotating heat source causes the liquid mercury to rotate in a direction counter to that of the flame, with a rate of rotation 4 times higher than the rotation rate of the flame.

The zonal winds on Venus are in this direction relative to the apparent motion of the Sun above them, and Schubert and Whitehead (1969) conclude that solar heating of the thick CO_2 atmosphere of Venus could be induced by this mechanism.

3.1.3 The Gierasch mechanism

Gierasch (1975) proposed a new mechanism to explain super-rotation, the 4 day circulation of the Venusian atmosphere and overturning in the atmosphere. The mechanism suggests a transport of retrograde zonal momentum upward at the equator then poleward, descending at the pole and then flowing equator-ward in the lower atmosphere, driven in the equator-ward flow by eddies, i.e. a Hadley type cell. The atmosphere on Venus shows a Hadley cell in each hemisphere, ranging from the equator to close to the pole. The momentum transported by the Hadley cell is proposed to be required to maintain the observed Retrograde Super-rotating Zonal flow.

The Gierasch (1975) mechanism assumes strong horizontal diffusion and weak vertical diffusion. The horizontal diffusion will produce a velocity distribution close to solid rotation at each level, and the meridional Hadley cell will transport angular momentum upwards at a sufficient rate to compensate for vertical diffusion.

Zonal winds generated at high levels can be in cyclostrophic balance against the meridional pressure gradient. On Venus the $\sim 100\ \mathrm{m\,s^{-1}}$ winds at the equatorial cloud tops are compatible with cyclostrophic balance if the equator to pole temperature dif-

ference is of the order of 3K throughout the atmosphere (Leovy, 1973).

The timescale of the meridional overturning of the Hadley cell is $\tau \simeq L/v = 10^7\ s$, where $L = 10,000\,\mathrm{km}$ is the equator to pole distance, and $v = 1\,\mathrm{m\,s^{-1}}$ is the typical meridional velocity. Therefore the Gierasch mechanism requires coefficients for horizontal eddy diffusion greater than $10^{11}\,\mathrm{cm^2\,s^{-1}}$, and for vertical eddy diffusion smaller than $10^5\,\mathrm{cm^2\,s^{-1}}$.

Gierasch (1975) suggests baroclinic instability associated with relative rotation might produce such strong horizontal mixing.

3.1.4 Held and Hou (1980)

Held and Hou (1980) proposed a theory for the meridional circulation with a number of models for an atmosphere which describe the generation of Hadley type cells. The description is applicable to general planetary atmospheres particularly for slowly rotating planets like Venus.

The essence of the models is a simple two layer, axisymmetric atmosphere with the lower layer coupled to the surface via friction and the upper layer almost inviscid. An overturning Hadley circulation moves air polewards in the upper layer and towards the equator in the lower layer. In the upper layer specific angular momentum, m, is conserved while in the lower layer zonal flow is weak due to friction.

3.2 One and two-dimensional models

3.2.1 Kalnay de Rivas (1975)

Kalnay de Rivas (1975) presented the results of two dimensional simulations of the deep circulation of Venus. The intention was to show that the high surface temperature of Venus can only be explained by the greenhouse effect, and not by any of the

competing theories around at the time (e.g. the Goody and Robinson (1966) dynamical model).

Secondly Kalnay de Rivas (1975) used the results from a quasi-three dimensional version of her model (obtained by extending the two dimensional model with some longitudinal wave terms) to test the then new Gierasch mechanism, which seeks to explain super-rotation and the 4 day Venus circulation.

The three dimensional model was a quasi-Boussinesq 'pressure type' model, where the original momentum equations were used to determine the pressure by the solution of an elliptic equation. The model used a combination of exponential Fourier components in the longitudinal plane (spectral method), and finite differences for the meridional plane (latitude and height).

The three dimensional model was tested with only the lowest zonal wavenumber's present and 18 grid intervals from equator to pole. In numerical experiments where the model was integrated for $2.2 \times 10^7\, s$ ($\sim$250 Earth days; 1 Venus sidereal day) Kalnay de Rivas (1975) obtained a maximum zonal velocity of 17 $\mathrm{m\,s^{-1}}$ at 10° from the pole. The model produced a single equator to pole Hadley cell for each hemisphere.

In other numerical experiments Kalnay de Rivas (1975) showed the Gierasch (1975) mechanism's dependence to work on the magnitude of the horizontal eddy diffusion. For these experiments integration times were $\sim$350 Earth days ($\sim$ 1.4 Venus sidereal days).

3.2.2 Young and Pollack (1977)

Young and Pollack (1977) used a three dimensional model with an equally spaced vertical grid, solving the primitive equations using centred and finite differences, and spectral harmonics to resolve the flow structure horizontally. The model used a maximum of 32 vertical levels, although most integrations used 16, up to 64 km at their

model top. Solar and infra-red heating rates were computed, the solar energy deposition rates giving a vertical temperature profile that was consistent with Venera 8 measurements. Considerable attention was devoted to discussion of eddy diffusion terms and their parameterizations.

Despite short integration times of the order of 15 Venus solar days, the results obtained by Young and Pollack (1977) were impressive. Zonal wind speeds reached up to $\sim 100\ \mathrm{m\,s^{-1}}$, in same direction as the underlying planet' s rotation, and the model exhibited stacked Hadley cells and warm poles. A perhaps more typical result for the winds was ~ 35 at the equator, increasing to a peak of ~ 51 at 50N and then reducing back to zero at the pole.

Young and Pollack (1977) suggest that the main mechanism for maintenance of the equatorial zonal wind, the super-rotation, is transport of angular momentum poleward by meridional circulation which is offset by equator-ward transport by planetary scale eddies. They state planetary scale eddies are the principal mechanism for converting potential energy to kinetic energy.

Subsequently, Rossow, Fels and Stone (1980) argued that the formulation by Young and Pollack (1977) and the conclusions drawn are incorrect. They point out that, with the exception of stresses at the surface, all model physics should conserve angular momentum, but the Young and Pollack (1977) vertical momentum diffusion formulation does not. Rossow, Fels and Stone (1980) also note that there are severe problems arising from the truncation used and the assumed symmetry which eliminates most of the wave modes.

3.2.3 Rossow and Williams (1979)

Rossow and Williams (1979) used a numerical two dimensional, horizontal model with a 128 x 128 grid point array and the Arakawa (1966) finite differences scheme, time-stepping with the standard leapfrog method with the aim of explaining the horizontal

distribution of angular momentum in Venus' stratosphere. Despite the relative lack of observational data available at the time Rossow and Williams (1979) conclude that the circulation is dominated by inertial effects, the turbulent cascade of kinetic energy and enstrophy. They posit a 'relaxed' state, resembling two dimensional vorticity conserving flow, which on a slowly rotating planet consists of a solid body rotation plus an advection wave (a Rossby-Hauritz wave) with zonal wavenumber 1, lying symmetrically about the equator.

Rossow and Williams (1979) also concluded that problems would arise in future attempts to model the Venus atmosphere because the inertial cascade process requires a relatively high resolution. They caution that coarse resolution, or severe truncation, will have two serious effects: that it increases the importance of eddy diffusion and that it artificially stabilises some of the planetary scale waves.

3.3 Three dimensional modelling after Pioneer Venus

After the Pioneer Venus spacecraft visited Venus in 1978 and released four descent probes more data was gathered on the structure and conditions of Venus' atmosphere. The improvement in available data allowed tighter constraints to be used for Venus GCMs, which themselves were improving in parallel with increases in computer power.

3.3.1 Rossow (1983)

Rossow (1983) used a three dimensional model to investigate:

i) whether the mean meridional circulation can provide the dominant vertical and horizontal heat flux in a massive, slowly rotating atmosphere as suggested by Stone (1974)

ii) what determines the the vertical and horizontal structure of the mean meridional circulation

iii) can the mean meridional circulation transport momentum over large vertical distances as suggested by Gierasch (1975)

iv) do some eddy motions behave as if they are barotropic two dimensional motions as suggested by Rossow and Williams (1979)

The model used was a version of the GFDL (NOAA/Geophysical Fluid Dynamics Laboratory) 9-levels, 15 wavenumber spectral GCM of Earth's atmosphere which had been modified to resemble Venus. When run for moderately long integration times (>5,000 Earth days), the zonal winds and circulation failed to reach the observed magnitudes. In the lower atmosphere, the zonal flow on Venus is 3–5 times stronger than produced by the model which developed $\sim 10\ \mathrm{m\,s^{-1}}$.

3.3.2 Mayr and Harris (1983)

Mayr and Harris (1983) also used a spectral model to discuss quasi-axisymmetric circulation in an anisotropic viscous fluid and super-rotation in planetary atmospheres, with a specific emphasis on Venus. Mayr and Harris (1983) state that it is understood that the required large eddy diffusivities may arise from longitudinal disturbances and therefore the flow is not completely axisymmetric. Flow in their model was driven by solar radiation absorbed at low latitudes, with air rising near the equator and falling at higher latitudes, a classic Hadley cell.

Assumptions made by Mayr and Harris (1983) included taking a Prandtl number of 1 (the Prandtl number = ν/α = kinematic viscosity/thermal diffusivity), and a ratio of 10^5 between the horizontal and vertical eddy diffusion coefficients; values which are broadly consistent with mixing length theory. In the Venus atmosphere, which is convectively stable, they found that the 4 day equatorial circulation could be maintained with a single Hadley cell. Above the clouds the latitudinal variation of temperature reverses, leading to warm poles. Depending on the assumptions made, in one case adding a Newtonian cooling term, the windspeeds achieved reached $> 100\ \mathrm{m\,s^{-1}}$.

3.3.3 Covey et al. (1986)

Covey et al. (1986) report the results of a series of experiments using a three-dimensional general circulation model where the planetary rotation rate was progressively slowed to evaluate the theories of Venus' super-rotation. Super-rotation theories imply the upward transport of angular momentum from the solid planet (Gierasch, 1975). The addition of significant momentum by tidal torques was considered unlikely, hence the angular momentum transported upwards must be of sufficient magnitude to spin up the atmosphere from rest to the observed super-rotating state, and then to maintain the super-rotation against frictional dissipation. The Gierasch mechanism suggests the zonal mean circulation will include a thermally forced equator to pole Hadley cell for a slowly rotating planet such as Venus.

The model used to test the theories of the Gierasch mechanism uses an "Earth" atmosphere, with the same atmospheric mass and composition as the Earth thus excluding the thick lower atmosphere of Venus and effectively only dealing with the Venus atmosphere at cloud levels. Covey et al. (1986) suggest that this restriction was insignificant because the Venus lower atmosphere is de-coupled from the upper atmosphere by a stable layer which confines the Hadley circulation to the upper levels, (Schubert et al., 1980). The model used was simplified by the omission of oceans, the hydrological cycle and topography.

This simplified model was first tested at the rotation rate of the Earth and the multi-cell structure observed was found i.e. a thermally direct Hadley cell at low latitudes, a cell rotating in the opposite sense in the mid-latitudes (a Ferrel cell), and the weaker polar cell at high latitudes. As the rotation rate of the planet was progressively slowed, the Hadley cell expands poleward, until it essentially reaches the poles when the rotation rate becomes 1/16th of the Earth's. As the rotation rate was slowed further, the equator to pole Hadley cell increases in magnitude. This behaviour was expected from the Gierasch mechanism.

Super-rotation was only weakly shown in the experimental results, both in the terrestrial rotation rate case and in the Venus slowly rotating case. The terrestrial rotation case agrees well with the observed slight super-rotation on Earth. However the magnitude and the latitudinal distribution do not match with observations of Venus' atmosphere. Covey et al. (1986)'s conclusions note that axisymmetric thermal forcing of a slowly rotating atmosphere is not solely sufficient to describe the Venusian atmospheric circulation, and wonder if the creation of weak super-rotation by the Gierasch mechanism may be necessary to establish the sign of Venus' rapid rotation and to set the conditions for subsequent acceleration to strong super-rotation.

3.3.4 del Genio and Zhou (1996)

Super-rotation was also tested in a number of numerical simulations by del Genio and Zhou (1996), work which followed previous studies by del Genio et al. (1993). Using an Earth like GCM partially modified for Venus parameters, tests were performed to investigate factors that influence the extent of equatorial super-rotation in statically stable atmospheres on slowly rotating planets, such as Venus and Titan. In these experiments the terrestrial type model was used with the removal of diurnal, seasonal and hydrological cycles, and without topographic and geographic variations.

del Genio and Zhou (1996) suggest that the key to super-rotation in the simulations is the presence of high altitude cloud cover. The clouds absorb significant amounts of insolation, thus stabilising the lapse rate and detaching the cloud level dynamics from the dissipation that occurs near the surface. Under these conditions the upward and poleward transport of angular momentum by the Hadley cell and the equator-ward eddy transport of momentum at low levels from the barotropic instability of the high latitude jet, the Gierasch mechanism, act to produce the super rotation. In their conclusions del Genio and Zhou (1996) state super-rotation could result provided the upper and lower atmospheric levels were decoupled and that care was taken to maintain precision for the momentum conservation properties on the model.

3.3.5 Yamamoto and Takahashi (2003a,b, 2004, 2006)

Yamamoto and Takahashi (2003a) used a spectral model developed for terrestrial modelling by the Center for Climate Research/National Institute for Environmental Study in Japan. This was a T10 model (a spectral model with triangular truncation at total wavenumber 10) with 50 vertical levels (L50) between 0 and 90 km. The grid for the calculation of the physical processes and non-linear terms was 32 x 16. The model was adapted to Venus parameters such as radius, gravity and rotation rate. Yamamoto and Takahashi (2003a) assumed a simplified radiative process of zonally uniform solar heating and Newtonian cooling. The profile of the solar heating rate is shown in figure 3.1.

Yamamoto and Takahashi (2003a) noted that the altitude of the maximum heating rate was lower than the cloud top heating maximum by about 10 km (Yamamoto and Takahashi (2003b) later noted that this profile produced fully developed super-rotation whereas a profile with a maximum at the cloud top did not). Solar heating due to CO_2 above 70 km and surface radiative processes are also neglected. The parameterization of the atmospheric diffusion was designed not to supply angular momentum from the surface to the atmosphere as is possible in Earth GCMs.

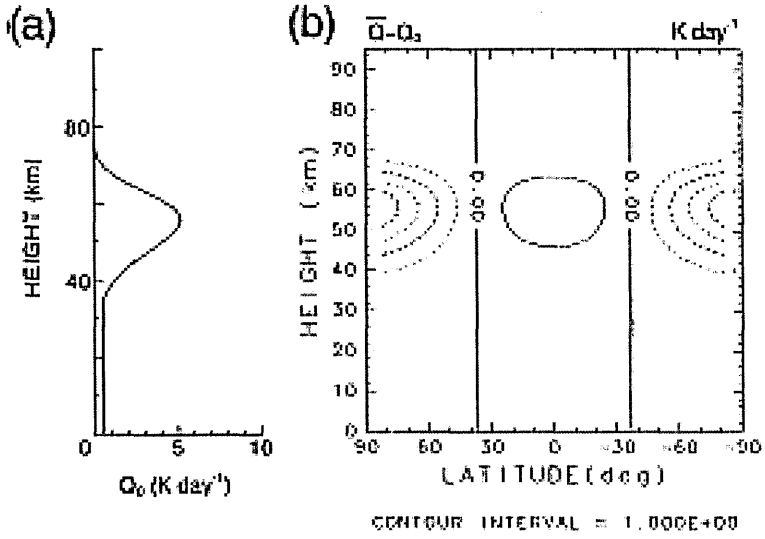

Figure 3.1: (a) The vertical profile of global mean solar heating rate Q_0 (K day^{-1}). (b) the latitude-height cross section of $\bar{Q} - Q_0$ ($\bar{Q}$:the zonal mean heating rate). Dashed curve indicates negative value. (From Yamamoto and Takahashi (2003a))

Spun up from rest and reaching equilibrium after $\sim$50,000 Earth days ($\sim$205 Venus days) the zonal wind peaked at approximately 100 m s^{-1} near 60 km altitude, at $\pm 60°$ latitude, with a similar form, though a smaller magnitude, to that shown in figure 3.2.

The observed super-rotation was maintained by the Hadley circulation, with a single cell, and various waves, essentially the Gierasch-Rossow-Williams (GRW) mechanism developed from Gierasch (1975). Vertically propagating gravity waves decelerate the flow above the clouds and enhance the meridional circulation, although the 4 day circulation was fully developed within the cloud layer.

Yamamoto and Takahashi (2003b) presented results from a model extended from Yamamoto and Takahashi (2003a) to T21 (a spectral model with triangular truncation at total wavenumber 21). With a 64 x 32 longitude-latitude grid in real space, the horizontal diffusion was 8th order. The vertical resolution remained at 50 levels between the surface and 90 km. The solar heating profile used was unchanged from Yamamoto and Takahashi (2003a), see figure 3.1.

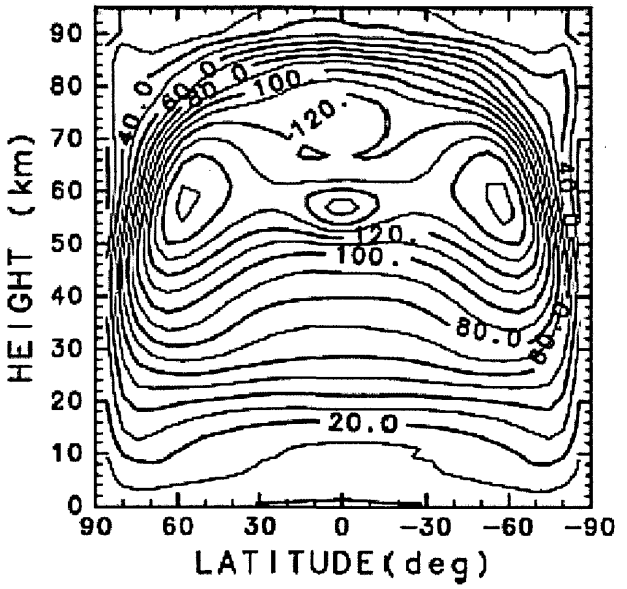

Figure 3.2: Latitude-height cross section of longitudinally averaged zonal flow (From Yamamoto and Takahashi (2003b))

Equilibrium was reached after $\sim$ 40,000 Earth days (165 Venus days). A zonal flow slightly stronger than previously was found, with windspeeds of $\sim 120\ \mathrm{m\,s^{-1}}$ between 50 and 70 km, and mid latitude jets again peaking at $\pm 60°$ near the cloud tops, see figure 3.2. Once again a single pair of Hadley cells was found to be predominant.

With more developments to their model Yamamoto and Takahashi (2004) refined their earlier simulations further. For these experiments, their model had 52 vertical levels, and a new three-dimensional solar heating and Newtonian cooling system. Although the heating distribution was improved over the previous model e.g. the peak solar heating was at a higher altitude, a little over 60 km above the surface, they noted that the heating rate below 55 km was much higher than is realistic for Venus.

A 4th order horizontal diffusion with an e-folding time of 4 days at the maximum wavenumber was introduced, which was less scale selective than in Yamamoto and Takahashi (2003a,b). The equator to pole temperature difference at the surface was set

to 10K, again prescribed to be larger than the real atmosphere ($\leq$ 5K). Linear surface drag was imposed with a time constant of 3 days.

These experiments again produced a strongly super-rotating atmosphere, with peak zonal wind-speeds of $\sim 100\,\mathrm{m\,s^{-1}}$ in the cloud tops at equatorial latitudes. Many waves are found, together with thermally induced tides. Yamamoto and Takahashi (2004) suggest that thermal tides are a more promising candidate for horizontal eddy momentum transport processes in the middle atmosphere rather than barotropic eddies.

Yamamoto and Takahashi (2006) further investigate the maintenance mechanism of super-rotation and the sensitivities to the surface boundary conditions, using the same model as Yamamoto and Takahashi (2004). The results were similar to Yamamoto and Takahashi (2004) with fully developed super-rotation and several waves with periods similar to those observed in Venus' atmosphere e.g. the 5.5 day, zonal wavenumber 1, Kelvin wave, as well as a range of thermal tides.

The experiments to test the sensitivity to the surface conditions revealed that the equator-pole temperature difference and the frictional drag are important parameters in the maintenance of the super-rotation. If any of these parameters were 'tuned' incorrectly then the peak zonal winds were found to be significantly reduced.

3.3.6 Lee, Lewis and Read (2007)

Lee (2006) began the development of a simplified Venus GCM, with radiative transfer simulated by linear Newtonian cooling in a similar, although not identical, distribution to Yamamoto and Takahashi (2003a,b). Using a modification of the UK Meteorological Office Hadley Centre Atmospheric Model, HadAM3, a finite difference, grid-point model run with $5° \times 5°$ horizontal resolution and 32 vertical levels, Lee et al. (2007) found a peak equatorial wind speed of $\sim 35\,\mathrm{m\,s^{-1}}$. A strong meridional circulation was developed in the form of a single Hadley cell in each hemisphere. Zonal jets were

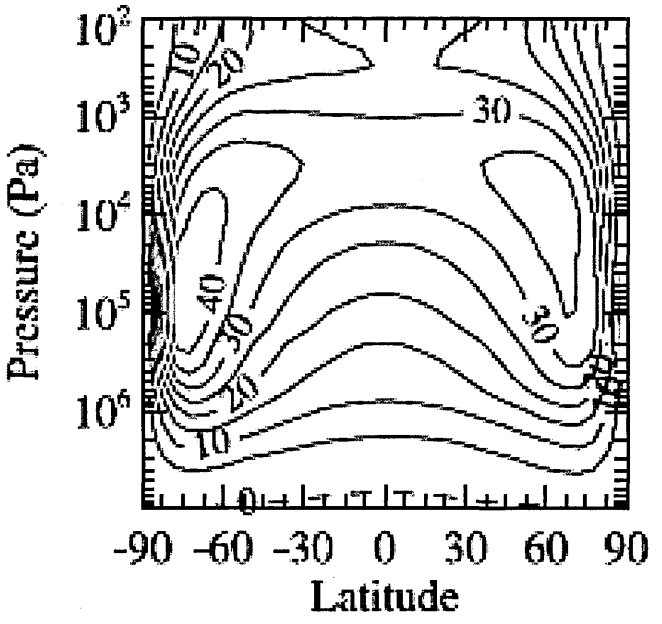

Figure 3.3: Zonal winds from Lee et al. (2007)

produced with a maximum of 45 $\mathrm{m\,s^{-1}}$ at 60 km in each hemisphere at mid latitudes, with a peak equatorial wind of 35 $\mathrm{m\,s^{-1}}$, as shown in figure 3.3. This GCM also produced significant warm pole and cold collar features.

The GCM used by Lee (2006); Lee et al. (2005, 2007) maintained super-rotation by a similar GRW mechanism (Gierasch, 1975) to Yamamoto and Takahashi (2003b), and reproduces many of the observed large-scale wave structures. In Lee et al. (2007) the period of the waves was much longer than is observed in the Venus cloud tops, which was related to the weaker than observed zonal wind. The mixed Rossby-Gravity wave mode has a period of $\simeq$ 30 days, slower than the $\simeq$ 5 days observed (del Genio and Rossow, 1990). Similarly the equatorial Kelvin wave was 9 ± 1 days rather than $\simeq 4$ days observed. The wave periods were shown to scale with the zonal wind speeds.

Development of this model has continued. Lee et al. (2010) introduced a simple bulk cloud parameterization and transport scheme. Mendonça et al. (2012) have introduced a more realistic radiation scheme which includes cloud scattering and have used the model for analysis of thermal winds.

3.3.7 Herrnstein and Dowling (2007)

Herrnstein and Dowling (2007) tested the effects of topography for a Venus atmospheric model. Using the PDS EPIC model, which was developed independently and using 20 vertical levels logarithmically spaced in pressure, Herrnstein and Dowling (2007) reproduced the results of Lee et al. (2007) for a smooth planet. The super-rotation was found to be diminished, peak wind speeds reducing from 55 $\mathrm{m\,s^{-1}}$ to 35 $\mathrm{m\,s^{-1}}$ when topography was added, the mid-latitude jets becoming asymmetric, and a slower jet in the northern hemisphere. The time to reach equilibrium was also reduced with topography included, taking a few Earth years rather than a few decades.

3.3.8 Hollingsworth, Young, Schubert, Covey and Grossman (2007)

Hollingsworth et al. (2007) adapted another terrestrial GCM, based on a version of the NASA Goddard Space Flight Center ARIES/GEOS dynamical core to Venus parameters and then used it to investigate the circulation equilibration and the formation of atmospheric super-rotation on a slowly-rotating planet. This model was run with a $4° \times 5°$ horizontal resolution and 56 vertical levels. Topography was not included.

Using a thermal structure similar to that of Yamamoto and Takahashi (2003a,b) the model was run for integrations of up to 20,000 Earth days. Super-rotation was achieved but was found to be slightly weaker than observed at $\sim 88\ \mathrm{m\,s^{-1}}$. A further experiment, performed with realistic heating, resulted in very weak super-rotation at $\sim 10\ \mathrm{m\,s^{-1}}$, and only weak eddy activity, confirming earlier studies which also used stronger than observed heating (Yamamoto and Takahashi, 2003a,b).

3.3.9 Lee and Richardson (2010)

Lee and Richardson (2010) compared three different dynamical cores for their response to Venus-like forcing and friction parameters in a Venus inter-comparison study.

The dynamical cores tested were an Arakawa B grid core, a spectral core and a finite volume (FV) core, each from the Geophysical Fluid Dynamics Laboratory (GFDL) terrestrial GCM. Each model was set up to have approximately 5° resolution for longitude and latitude. The thermal forcing, surface Rayleigh friction and 'sponge layer' were all taken from Lee et al. (2007).

Lee and Richardson (2010) presented results for integrations of 22,599 Earth days. All 3 GCMs were found to produce super-rotating winds of $35 \pm 10\ \mathrm{m\,s^{-1}}$ at the equator, with faster mid-latitude jets, however there was some sensitivity to the dynamical core type. The same momentum transport processes as Yamamoto and Takahashi (2003b) and Lee et al. (2007) dominated in all the models tested, unsurprisingly since all the GCMs were forced with the same simplified thermal function and had no diurnal tides or topography. The tests presented led Lee and Richardson (2010) to highlight the need for improved radiative parameterization which could include the effect of the thermal tidal forcing and also allow for radiative transfer between atmospheric layers.

3.3.10 LMD: Crespin, Lebonnois, Hourdin, Eymet, Fournier and Forget (2006)

Crespin, Lebonnois, Hourdin, Eymet, Fournier and Forget began the development of a more realistic Venus GCM at Laboratoire de Météorologie Dynamique in Paris based on experience with Earth, Mars and Titan models. The scheme was adapted to work with the LMDZ finite-differences dynamical core, run with a 48 x 32 horizontal grid with 50 vertical levels from the surface up to 95 km altitude.

Crespin et al. (2006) presented initial results for simulations using this model and found zonal winds of $\sim 150\ \mathrm{m\,s^{-1}}$ near the cloud tops, after $\sim$ 50,000 Earth days following a start from rest.

Lebonnois et al. (2010) presented a more comprehensive study of the results obtained with the LMDZ Venus GCM over a large range of parameters. The model now included topography, a diurnal cycle, dependence of the specific heat (C_p) on temperature, and a radiative transfer module which allowed a consistent computation of the temperature field.

Lebonnois et al. (2010) discussed results for the zonal wind and mean meridional circulation under four scenarios. These used both a realistic radiative transfer code and a simplified radiative forcing as used in Lee et al. (2007) and similar to Yamamoto and Takahashi (2003a,b, 2004, 2006); Herrnstein and Dowling (2007); Hollingsworth et al. (2007). Both radiation schemes were tested with and without topography. The results with simplified radiative forcing are broadly consistent with earlier studies. Slightly faster wind-speeds were produced by the realistic radiative transfer experiments with peak speeds $\sim 60\ \mathrm{m\,s^{-1}}$, although still weaker than observed on Venus. Figure 3.4 shows plots of the zonal wind and meridional circulation for each of these configurations.

In contrast to Herrnstein and Dowling (2007), Lebonnois et al. (2010) found the zonal wind peak speed and super-rotation were enhanced by the addition of topography.

Lebonnois et al. (2010) concluded that the angular momentum transport was consistent with the Gierasch-Rossow-Williams (GRW) mechanism when no diurnal cycle was used. With the addition of the diurnal cycle, however, the mechanism controlling super-rotation becomes more complex. The mean meridional circulation transports angular momentum upward (despite stacked, multiple Hadley cells in the model) and poleward. The thermal tides weaken this poleward transport and add a significant downward transport at the equator. This transport allows accumulation of angular momentum at low latitudes and prevents the formation of such clear high- and mid-latitude jets as were seen in models without the diurnal cycle.

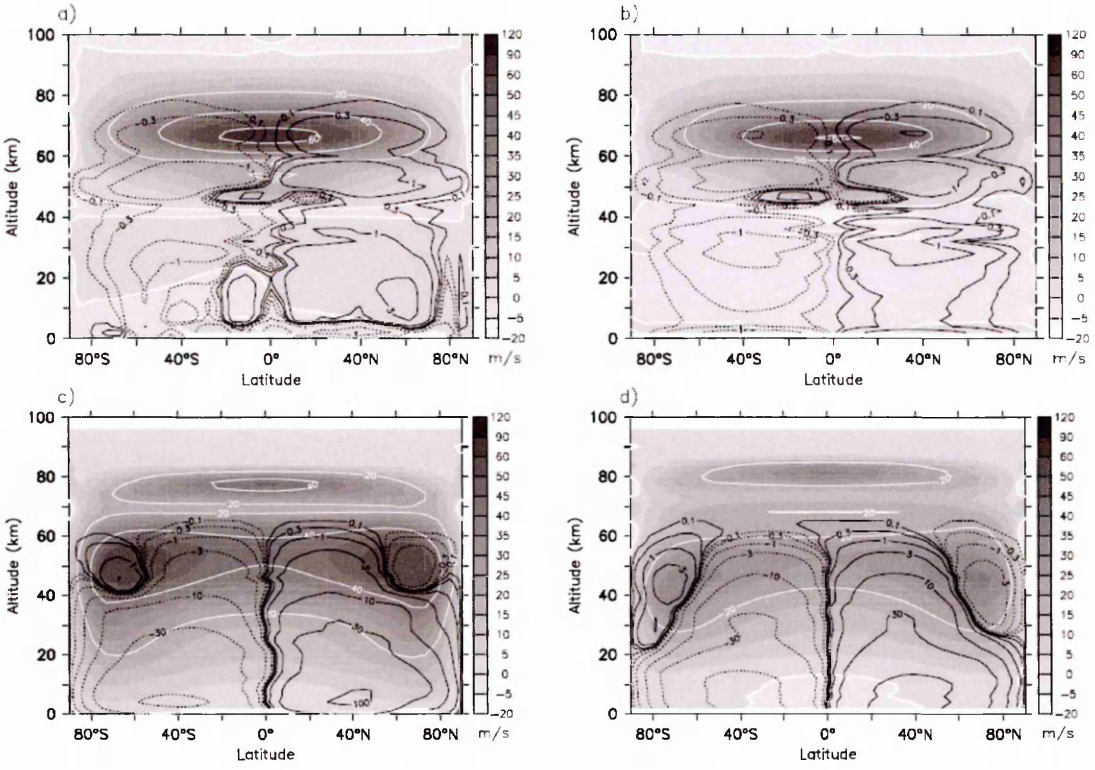

Figure 3.4: Wind and MMC plots from Lebonnois et al. (2010). (a) realistic radiative transfer and topography (b) as a) without topography (c) Newtonian cooling and forcing with topography (d) as c) without topography

3.3.11 The VSGCM, the model described in this document

A brief overview of the model is provided here; more technical details are in chapter 4.

The Open University Venus Simplified General Circulation Model (VSGCM) is a pseudo-spectral model. This is a model which stores its variables (temperature, vorticity, divergence, and log-surface pressure) as coefficients of Legendre polynomials in latitude and Fourier series in longitude (Hoskins and Simmons, 1975).

When the model needs to calculate the non-linear products of terms it is more efficient to transform to a real-space grid, calculate the non-linear products, and then transform the resulting tendencies back from the real-space grid to spectral coefficients. Linear calculations are more efficiently calculated in spectral space, since they can be applied to each coefficient individually and spatial differentials, such as Laplacians, are found easily and accurately. It is possible to have a purely spectral model, but the number of nonlinear products between different terms builds up rapidly as the resolution increases. This quickly becomes very prohibitive in terms of calculation and these types of model are very rarely used except as demonstrations, with all practical implementations using the transform technique for non-linear products.

In the vertical the model uses a sigma coordinate, which provides a terrain following capability, with a finite difference division into layers. The modelled atmosphere ranges from the surface to approximately 80 km altitude. This includes the cloud layers between approximately 45 and 65 km altitude which are important for the trapping and transfer of solar radiation into the atmosphere. The global model is simplified in that it does not contain a hydrological cycle, cloud physics, or detailed line-by-line radiative transfer code — instead using a Newtonian relaxation towards a prescribed temperature state.

The majority of experiments described in this thesis use a triangular truncation in spectral space at total wave number 21 (T21) intended to give broadly homogeneous resolution in each direction. At T21 resolution where there are 64 $\times$ 32 boxes (longitude and latitude) for each level, approximately equivalent to a 5.6° (600 km $\times$ 600 km, at the equator) resolution grid point model. In the vertical direction there are 50 levels from the surface to approximately 80 km altitude. Simulations were also performed with vertical resolutions with 32, 100 and 200 levels, and horizontal resolutions of T10 and T42.

The model is written in FORTRAN, and contains routines to solve the "primitive equations of meteorology" (Hoskins and Simmons, 1975). The variables stored are the temperature, vorticity, divergence and log-surface pressure. With these independent variables it is possible to calculate many dependent quantities such as the zonal and meridional winds and meridional circulation, which are shown for the experiments described in this dissertation. The solution of the "primitive equations of meteorology" is, like weather prediction, an initial value problem. The initial conditions used here were an atmosphere in which temperature only varied in the vertical (with pressure), at rest (zero zonal and meridional wind) and in co-rotation with the underlying planet (so the divergence was zero and the vorticity only that connected with the planet's steady rotation). Surface pressure was uniform for smooth runs and in hydrostatic balance for runs with topography. Parameters are given to the model by proscribing a restoration temperature to relax towards, at a rate which is itself a function of pressure/height, and a description of the basic planetary parameters (radius, rotation rate, specific gas constant). Further details are provided in chapter 4. Using those initial values a prediction is made of the state of the atmosphere one time step (typically 10–30 minutes) in the future. This prediction is then used as the initial conditions for another solution of the equations a further time-step into the future. This process is continued until the simulation comes to an end.

In order to begin use for the studies described in this thesis the model was first converted to Venus parameters. The temperature forcing was specified based on that used by Lee (2006) in a form suitable for use by the spectral code of the VSGCM. The topographical data from the Magellan mission was downloaded from the NASA website (Saunders et al., 1990), transformed from real space to spectral coefficients, smoothed and converted to a spectral file for use by the model. A diurnal cycle was coded, involving modification to many of the model subroutines, to provide a time-dependent temperature relaxation state rather than a static one.

3.4 Summary

This chapter was a review of many of the previous modelling studies of the atmosphere of Venus. Initially an experiment to possibly explain atmospheric motion driven by thermal motion and therefore super-rotation by Schubert and Whitehead (1969) was summarised. A description of the mechanism suggested by Gierasch (1975) was given, a mechanism which has been used and tested by many models.

Following this experiment and putative super-rotation mechanism, brief descriptions and summaries of the one and two-dimensional models used by a number of research groups up to the 1978 Pioneer spacecraft's arrival at Venus were given.

Following Pioneer Venus increasingly sophisticated three-dimensional models became common. Many of these models were summarised, where for each model a description of the model's intended use was given and the main results obtained from that model presented.

More recent models have become more realistic and sophisticated, particularly in

their radiative treatment. With radiative transfer code allowing consistent computation of the temperature field, cloud micro-physics routines and the inclusion of topography and the diurnal cycle. Models can now simulate super-rotation although in many the magnitude of the zonal wind and super-rotation is less than observed. There remain many uncertainties in the parameterizations used which can be investigated efficiently by simple models which require less computational expense. The simplified GCM described in this dissertation will allow many of these parameterizations to be tested and characterised prior to inclusion in more complex models.

Chapter 4

The Venus Simplified Global Circulation Model and Set up for Experiments

In this chapter the model and parameters common to all integrations that were performed are described. The chapter begins with a brief history of the model and its development; followed by a description of the model core and the truncation type, and the main types of global model now used for climate and atmospheric simulations and weather forecasting. The radiative temperature, from Lee (2006), used in the simulations is described and plots of the vertical profile of thermal forcing and equator to pole temperature profile are provided. The settings used for the experiments are then detailed beginning with the vertical levels and sigma levels used for the reference and later simulations. Some details of the sigma level to height conversion are provided. This information is followed by an explanation of the time-steps per day used, a discussion of the Venus rotation rate, tables of the planetary parameters, and details and justification for the restoration and friction timescales selected.

4.1 History of the model

The model code was originally developed by the Atmospheric Modelling Group at the University of Reading, using the integration technique described by Hoskins and Simmons (1975), for use as a terrestrial Global Circulation model (GCM). Subsequently the spectral core was used and developed by researchers at Oxford University, for successful modelling of Mars' atmosphere (Joshi et al., 1995; Collins and James, 1995; Lewis et al., 1996; Collins et al., 1996; Forget et al., 1999; Newman et al., 2002; Lewis and Read, 2003), and forms the basis for the UK Mars GCM (MGCM). It is now used by researchers at the Open University for Mars studies (e.g. Spiga et al., 2011).

The code was originally written in FORTRAN-77, although later versions of Fortran have been incorporated during later developments. The code has been well tested over the years by the many previous modelling groups and other researchers. The code is highly modular and allows certain features to be switched on or off depending on the desired experiment, for example features such as topography. The model can easily be customized for different planetary and atmospheric parameters, either by setting defaults in the code or by use of the input 'namelist' which is read each time the model is started. Using the namelist to set parameters saves the need to re-compile the code when making changes to the model settings.

The code for this version of the model has been set for Venus planetary and atmospheric parameters (see section 4.5) and this version is now known as the Venus Simplified Global Circulation Model (VSGCM).

4.2 The Spectral core

The VSGCM uses a spectral core, which solves the hydrostatic primitive equations of meteorology on a sphere, and represents the main atmospheric variables as a series expansion of spherical harmonics. The maximum wavenumber retained determines

the resolution. The VSGCM requires the non-linear terms and physical tendencies to be calculated in real space on a grid. The conversion between spectral space and grid-point space is performed by Fast Fourier Transform (FFT) routines included with the model code. Both the resolution and grid used can be easily changed with a simple setting in a file used for setting the model parameters prior to compiling the model code. The truncation is triangular.For the majority of this study the resolution used was T21, that is triangular truncation with maximum retained wavenumber 21. With this resolution the grid, on which non linear products are calculated in real space, is 64 x 32: that is 64 longitudes and 32 latitudes. Comparative runs have been performed at T10 and T42 resolution (see Chapter 7), with grids of 32 x 16 and 128 x 64 respectively.

4.3 Spectral models vs. Grid Point

For atmospheric modelling using global models and Numerical Weather Prediction (NWP), the other common type of model used is the grid-point model (Andrews, 2000; McGuffie and Henderson-Sellers, 2005). With this type of model the variables are computed at discrete points in longitude, latitude and height, in a grid of 'boxes'. Grid-point models can be further subdivided into 'finite difference' models and 'finite volume' models.

Grid-point models have the advantage that they do not require transforms between spectral and gridded space, which can introduce errors into a spectral model's solution. However, the approximations used in a grid-point model's equations can introduce a truncation error. Generally the magnitude of the overall computational error is larger than for spectral models of similar resolution (Andrews, 2000).

Spectral models calculate the linear quantities of the equations of motion exactly and are generally faster to run than grid-point models (Andrews, 2000), although as resolution is increased the speed advantage lessens (McGuffie and Henderson-Sellers, 2005).

4.4 Radiative temperature

The thermal forcing used is a simple linear thermal relaxation scheme based on Lee (2006). This provides a simple parameterization of the processes in the atmosphere which contribute to the heating and cooling, without the need for complex radiative transfer equations.

The radiative tendency of temperature (the difference in temperature between one model time-step and the next), at longitude λ, latitude ϕ and pressure level p, is given by:

$$\delta T_{\text{rad}}(\lambda, \phi, p, t) = -\frac{T(\lambda, \phi, p,) - T_0(\phi, p)}{\tau} \times \delta t \tag{4.1}$$

where $T_0(\phi, p)$ is the thermal structure and τ is the time constant for this forcing.

The thermal structure $T_0(\phi, p)$ is given by Lee (2006) as:

$$T_0(\phi, p) = T_{\text{ref}}(p) + T_1(p)(cos(\phi) - C) \tag{4.2}$$

where:

$T_{\text{ref}}(p)$ is a reference vertical temperature profile.

$T_1(p)$ is a term giving the peak equator to pole temperature difference, as chosen by Lee (2006) to reflect the peak in adsorption of insolation within the cloud deck.

The constant C is the integral of $cos(\phi)$ over the domain, equal to $\pi/4$

The value of τ, the relaxation timescale, is 25 Earth days for the lower levels, reducing in the upper levels to 22, 18 and 15 Earth days, respectively.

A plot of the vertical temperature profile at the equator is shown as the black line in figure 4.1, also shown is a profile using data from the Magellan satellite mission, as a purple line, extrapolated to the surface with a constant lapse rate from the lowest point reached by the satellite data (33 km).

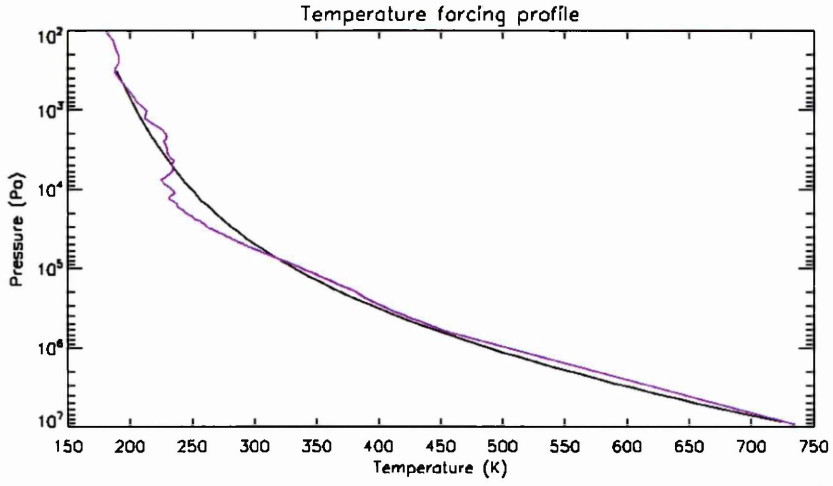

Figure 4.1: Vertical profile of thermal forcing

The equator-pole temperature difference (from Seiff et al., 1985) is shown graphically in figure 4.2. The plot shows the equator-pole temperature difference for latitude and pressure level.

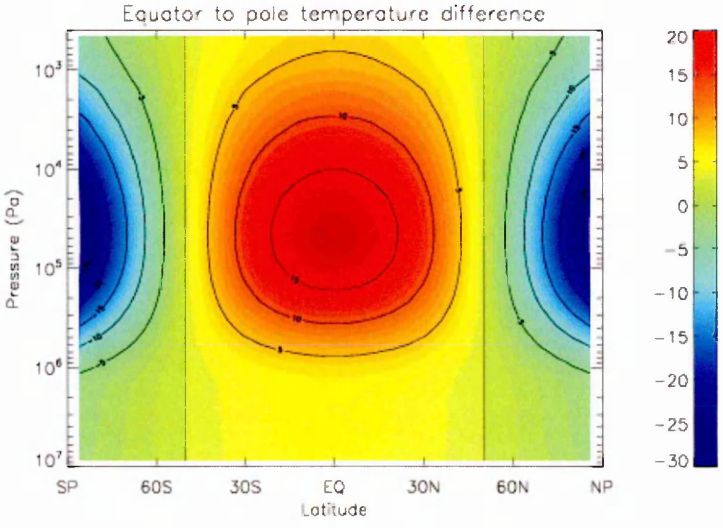

Figure 4.2: Equator - pole temperature

4.5 Settings for experiments

4.5.1 Vertical levels

The VSGCM can be configured to use any number of vertical levels. For each individual level a value for 'Rayleigh Friction', τ_F, which applies linear drag to the velocity components and for the 'restoration timescale', τ_R, which specifies linear Newtonian cooling towards a specified temperature state can be set.

The VSGCM was tested with the number of vertical levels between 10 and 200, to determine the accuracy and computation time required. The vertical levels range from the surface to approximately 80 km. Rayleigh friction was applied to the lowest model layer to simulate the atmospheric drag experienced and the four top layers provide a 'sponge layer', which applies Rayleigh friction to either all components or just eddy components of the flow, selectable by a switch in the input namelist, to dampen any upward-propagating wave reflections from the model top.

4.5.2 Sigma levels

In the vertical direction a pressure based co-ordinate is used by the model, known as sigma pressure. The sigma levels are defined as $\sigma = P/P_S$, where P is the pressure and P_S the surface pressure. Because the pressure is referenced to the surface pressure, sigma levels provide a terrain following capability.

The sigma levels were generated in the VSGCM code using a subroutine known as the Lewis-Hourdin level scheme (L-H scheme). This scheme calculates the sigma levels based on four values input into the code (the scale height; the height of the upper boundary of top free layer; the thickness of the lowest layer; and the number of levels in the upper sponge region). The sigma levels for 50 vertical levels (NL=50) generated using this scheme are shown in figure 4.3.

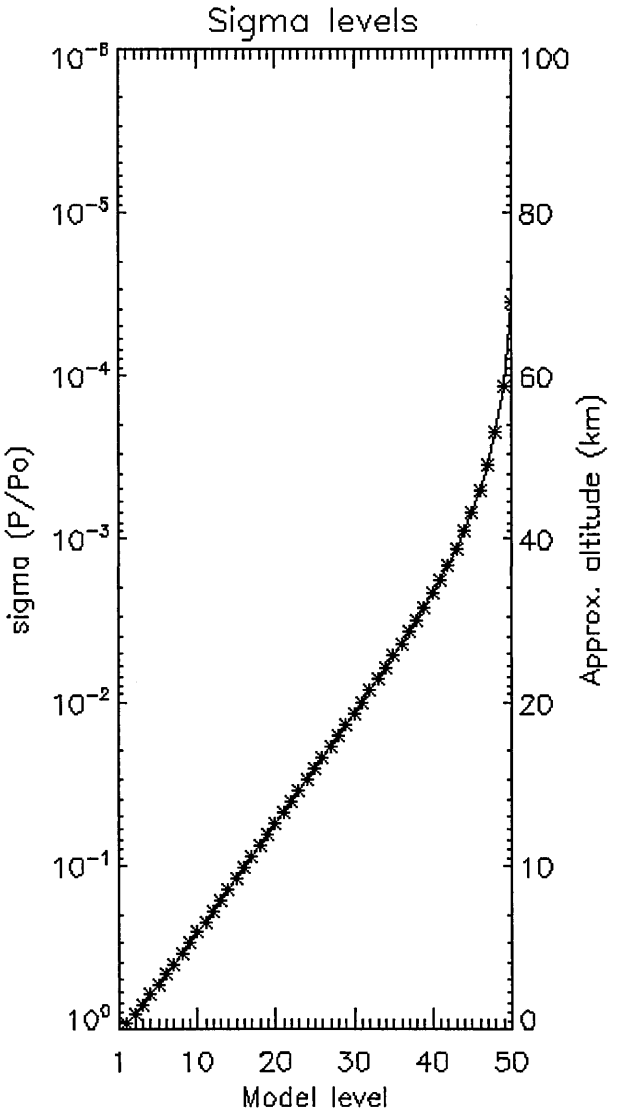

Figure 4.3: Sigma levels

For the majority of simulations 50 vertical levels were used in the VSGCM, ranging from close to the surface, $\sigma = 0.937$, a height of approximately 1 km, to the top of the atmosphere modeled at $\sigma = 2.265 \times 10^{-6}$, a height of approximately 77 km. At the upper levels the top 4 model levels are used as a sponge layer, where either all components of the flow or only the eddy terms are progressively reduced to zero, to damp vertically propagating waves preventing reflections from the model top.

For simulations with a different number of vertical levels (e.g. NL=32, NL=100 and NL=200) the sigma levels were interpolated from the 50 levels shown in figure 4.3 and recalculated for the required number of levels.

4.5.3 Sigma to Height conversion: Pseudo heights

Although the model uses pressure for the vertical co-ordinate, in some cases it is required or provides greater clarity to express the vertical axis in height or altitude (e.g. the cloud height). Where this is needed the pressure must be converted to a height. There are a number of commonly used methods for performing this conversion. One of these methods is integration of the hydrostatic equation:

$$-z = RT(P)/g \times (P/P_0) \tag{4.3}$$

where: z is height, R the gas constant, T temperature, P pressure and P_0 surface pressure. Assuming g is invariant over z and Height described as $-z$ because the gravity term acts in a downwards direction.

Alternatively the hydrostatic equation can be converted by:

$$z = -H(\ln p/p_s) \tag{4.4}$$

where: $H = RT_0/g$ and p/p_s is σ, which only the requires the surface temperature.

However using equation 4.4 can be inaccurate as the H term, the scale height, changes with increasing altitude. For better accuracy using this method the scale height, H, should be recalculated as the pressure reduces with altitude.

Each of the approximate conversions above gives slightly different results. The conversion used for the diagnostic plots and routines used for this thesis is the simple integration of the hydrostatic equation shown in equation 4.3.

4.5.4 Time-steps per day

The VSGCM integrates forward in time in time-steps, set to a time which is small enough to ensure an accurate and numerically stable solution of the primitive equations of meteorology, but sufficiently long for the running time to be achievable with the computing power available.

Due to the slow rotation rate for Venus the number of 'time-steps per day' (TSPD) has been set to 24,000. This is approximately equivalent to an Earth model integrating forward in time-steps of 1/4 hour (Earth or Mars configurations would typically use TSPD of $\sim$100 at the same horizontal resolution), which has been shown to provide the required acceptable compromise between accuracy and computing time when used with the Venus rotation rate.

4.5.5 Rotation rate

Venus rotates on its axis once every 243 Earth days, giving a rotation rate of $\omega = 2.99 \times 10^7 s$. The direction of rotation is retrograde when seen from above the Sun's North Pole (i.e. above the ecliptic plane) which suggests using a negative value for ω, however to ensure correct performance of the model's diagnostics a positive value was chosen.

The North Pole of any body in the solar system is defined by its rotation (Seidelmann et al., 2005) according to the 'right hand rule'. Using this definition the Venus North Pole is at the bottom (when viewed from above the ecliptic). The model places the North Pole at the top and so with ω positive used care must be taken when interpreting results where rotation is important such as the directions of $\bar{u}$ and v, the progression of the modeled sub-solar point and topographical features.

4.5.6 Planetary parameters

For use with a Venus atmosphere the following planetary parameters were set for the VSGCM:

Table 4.1: Parameters and values

Parameter	**variable**	**Value**	notes
Acceleration due to gravity, g (ms^{-2})	GA	8.87	NASA PDS (2009a)
Planetary radius (m)	RADEA	6052×10^3	NASA PDS (2009a)
Angular rotation, Ω (s^{-1})	WW	2.99243×10^{-7}	NASA PDS (2009a)
Gas constant, R ($Jkg^{-1}K^{-1}$)	GASCON	188.9	NASA PDS (2009b)
R/C_p	AKAP	208.9×10^{-3}	NASA PDS (2009b)

4.5.7 Restoration and Friction timescales

Restoration and friction settings are expressed in sidereal days. To convert to Earth days these figures are multiplied by 243, the number of Earth days Venus takes to orbit the Sun.

The values used for τ_{R}, the restoration timescales, are from Lee (2006). The values used for τ_{F}, Rayleigh friction, follow the values used by Newman and Leovy (1992).

Table 4.2: Restoration and Friction timescales

Level	τ_R	Earth days	τ_F	Earth days
1	0.062	15	0.0046	1.12
2	0.074	18	0.0057	1.39
3	0.091	22	0.0059	1.43
4	0.1029	25	0.007	1.70
5–btm+1	0.1029	25	0.0	0
btm (sfc)	0.1029	25	0.0123	3

Lee (2006) used values for Rayleigh friction, τ_F , and the sponge layer, which were very different. Lee (2006) used τ_F =32 Earth days for the bottom layer, which in his model was at $\sim$1 km above the surface. The three top levels were used as a sponge layer, with values between 100 and 0.01 Earth days , values decreasing with increasing height, and acting only on eddy components of the flow. For the sponge layer, other Mars simulations have used the top three levels with values of 2, 1 and 0.5 Earth days, values decreasing with increasing height, again acting only on the eddy terms.

4.5.8 Run length

The VSGCM was run for simulations of 500 and 250 Venus sidereal days starting from an initial state with the atmosphere at rest. Table 4.3 summarises some typical simulation run lengths, giving the equivalent times in Earth days and Earth years.

Starting with the atmosphere at rest is known as 'spinning-up', where the model output settles into an equilibrium state and large changes over short time scales will no longer be taking place.

Table 4.3: Run lengths

Venus days	Earth days	Earth years
10	2430	6.65
50	12150	33
100	24300	66.5
250	60750	116
500	121500	333

The output from the VSGCM was saved to a 'history' file 10 times per simulation day. The 'history' file was then used to diagnose the VSGCM output after averaging the last 4 days of the simulation, except for angular momentum where this was calculated for each day of the simulation.

4.6 Summary

In this chapter the model and parameters common to all integrations are described. The chapter begins with a brief history of the model and its development. Followed by a description of the model core, and the main types of global model now used for climate and atmospheric simulations and weather forecasting. The radiative temperature, from Lee (2006), used in the simulations is described and plots of the vertical profile of thermal forcing and equator to pole temperature profile are provided. The settings used for the experiments are then detailed beginning with the vertical levels and sigma levels used for the reference and later simulations. Some details of the sigma level to height conversion are provided. This information is followed by the time-steps per day used, a discussion of the Venus rotation rate, tables of the planetary parameters, and details and justification for the restoration and friction timescales selected.

Chapter 5

Results: Reference runs and Topography

In the first three sections of this chapter results of simulations performed with the VSGCM when using nominal settings will be presented. In the final two sections of the chapter details of the topography of Venus, the dataset used to generate a topography file for the VSGCM, and experiments including topography will be shown. The initial runs are the base-line simulations and will be used as reference simulations for later experiments. For these model runs the VSGCM was set-up as described in section 4.5, with 50 vertical levels and using the temperature state described in section 4.4, the N_4 forcing state (an explanation of the naming of the forcing states is given in section 6.0.1). For the base-line simulations the planet surface is assumed to be smooth and no topography or diurnal cycle was included.

For these simulations the VSGCM was run for 250 Venus days (Vdays). Diagnostics were produced from the output averaged over the last 4 Vdays. For the reference simulations two configurations of the sponge layer (see section 4.5.7) were used. Firstly with the sponge layer set to operate on eddy terms only, and secondly with the sponge layer set to operate on all terms.

For each simulation the total atmospheric angular momentum S was calculated at the end of each Vday of the simulation. S was normalised by dividing the calculated value by the value for S when the atmosphere is at rest, in co-rotation with the solid planet beneath (3.49×10^{27} kgm^{2}s^{-2}). The S shown is therefore S-1 (see equation 2.9). Graphs of the time development of S will be shown to help determine the equilibrium state of the simulations.

Plots will be presented for zonal wind ($\bar{u}$), local super-rotation index (s) calculated from the wind field (see equation 2.8), and mean meridional circulation (MMC) where any Hadley cells developed in the simulation are seen. The final plot for the reference simulations is the temperature minus the global mean temperature over all heights:

$$\Delta T(\lambda, p) = T(\lambda, p) - \bar{T}(\lambda, p) \tag{5.1}$$

where λ is longitude and p is pressure.

Known as the temperature anomaly (ΔT) these plots show the detail of the temperature state of the simulated atmosphere.

The following plots for $\bar{u}$, s, MMC and ΔT are presented with latitude on the x-axis, the South pole on the left, the equator central and North pole to the right. The y-axis represents vertical height and is shown as pressure, ranging from the surface at 9.2×10^6 Pa to 100 Pa ($\sim$ 100 km).

The cloud layers are important on Venus for the atmospheric circulation. The clouds play a significant role in the greenhouse effect and the highest wind speeds that have been measured by entry craft are just above the cloud layer. The base of the cloud layer on Venus is at an altitude of $\sim$45 km, equivalent to 2×10^5 Pa, the cloud tops are at $\sim$ 65 km, equivalent to 10^4 Pa. These levels are marked on the plots with dashed lines for reference however it should be noted that cloud physics are not included in

the model and the forcing profiles have no representation of the cloud heights. The graphics in figure 2.1 and figure 2.4 show the cloud layers.

For the topography simulation plots are presented for surface pressure and zonal wind minus the zonal wind from the reference simulation.

5.1 Base run with sponge layer on eddies only

5.1.1 Atmospheric Angular Momentum

The time evolution for S for the base-line run is shown in figure 5.1. The red line is the S calculated at the end of each Vday of the simulation, hence the first value plotted on the graph is slightly above 1, the value at the start of the first Vday of the simulation. The grey line is the same data with a simple smoothing function, which averages each value with its neighbouring values, applied to dampen the short term variation in S from day to day. Applying the smoothing more clearly indicates when a stable equilibrium has been achieved.

From this graph it can be seen how S increases from Vday 1 at the start of the simulation reaching a steady state after a little over 100 Vdays. There is some variation around the mean steady value but overall the S is no longer changing by a significant amount. The stable equilibrium value achieved is around 4.3. This indicates the simulation time of 250 Vdays is unnecessary, and that a valid result for the winds achieved would be obtained after a much shorter integration time.

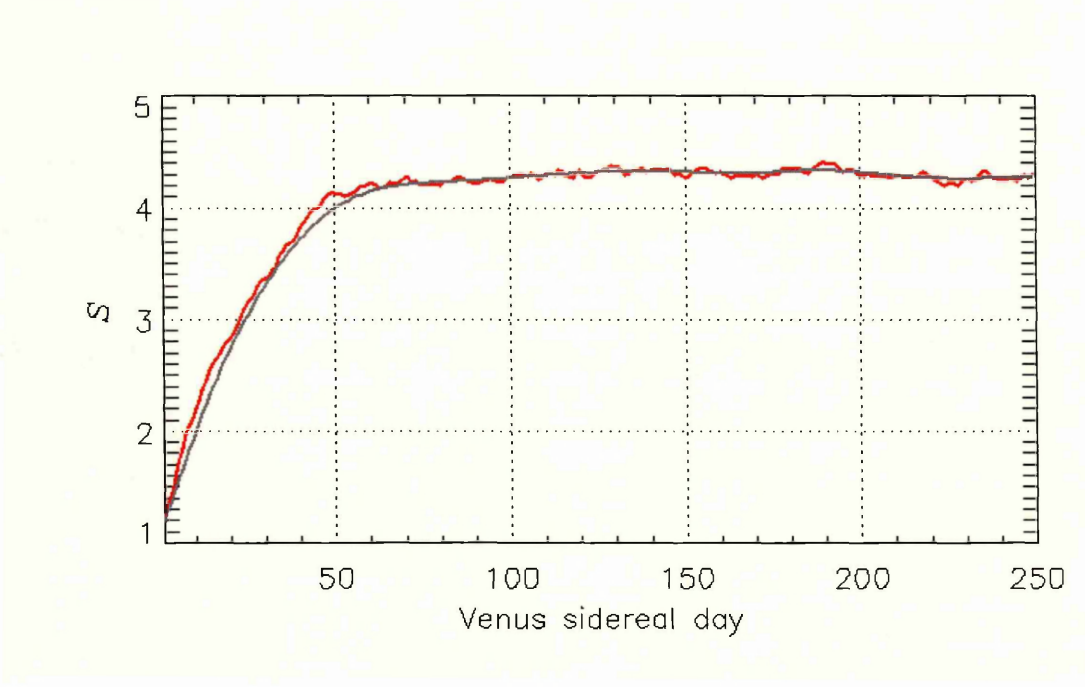

Figure 5.1: Time evolution of S for base run with sponge layer on eddy terms

5.1.2 Zonal wind

The zonally averaged zonal wind $\bar{u}$, for the base run with the sponge layer on eddies is shown in figure 5.2. The winds generated for this simulation are weaker than observed in Venus' atmosphere, with a maximum wind speed in the lower atmosphere (below the cloud tops) of $< 20\ \mathrm{m\,s^{-1}}$. Wind speeds of $> 50\ \mathrm{m\,s^{-1}}$ can be seen high in the atmosphere (above the clouds) in the two jet features at high latitudes.

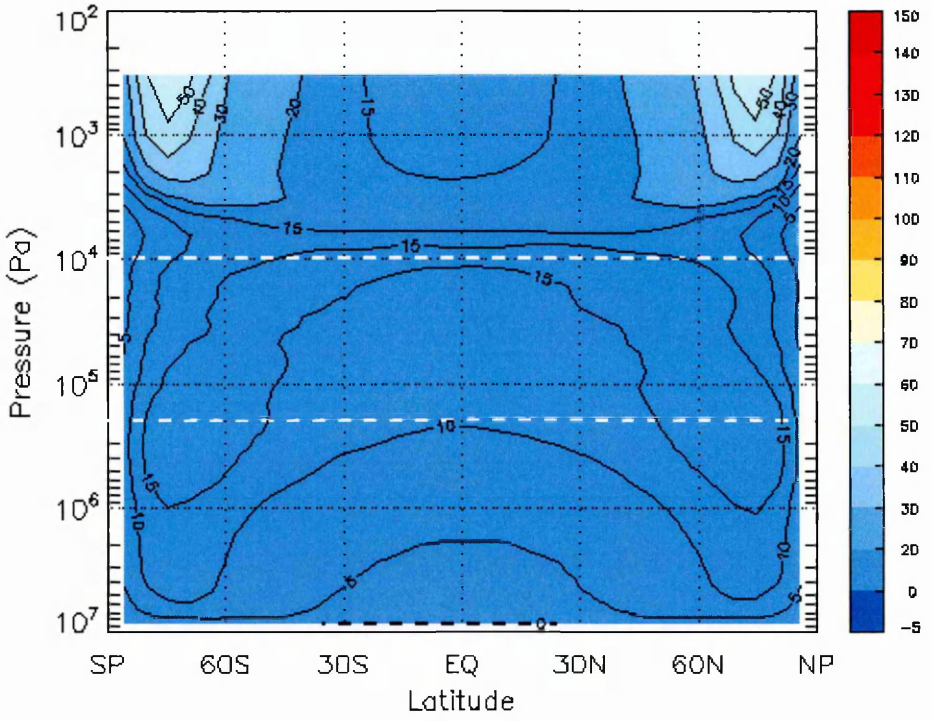

Figure 5.2: Zonal wind for base run with sponge layer on eddy terms only, averaged over final four Vdays of simulation, dashed lines indicate cloud levels.

5.1.3 Local super-rotation index

In addition to the winds it is interesting to consider the local super-rotation index, s, for the run (see equation 2.8 for a definition of the local super-rotation index). The local super-rotation index is shown in figure 5.3. This plot shows overall only weak super-rotation, with the strongest in an area between approximately $\pm 45°$ within the cloud layer, extending in latitude as height increases above the clouds. The maximum value of s for this simulation is 9.3, this is less than the super-rotation observed on Venus ($s \simeq 60$, calculated from the observed winds (e.g. Peralta et al., 2007; Sánchez-Lavega et al., 2008)), as would be expected because local super-rotation index is calculated using equation 2.7 which contains the $\bar{u}$ term, the longitudinally averaged zonal wind speed, which was weaker than observed.

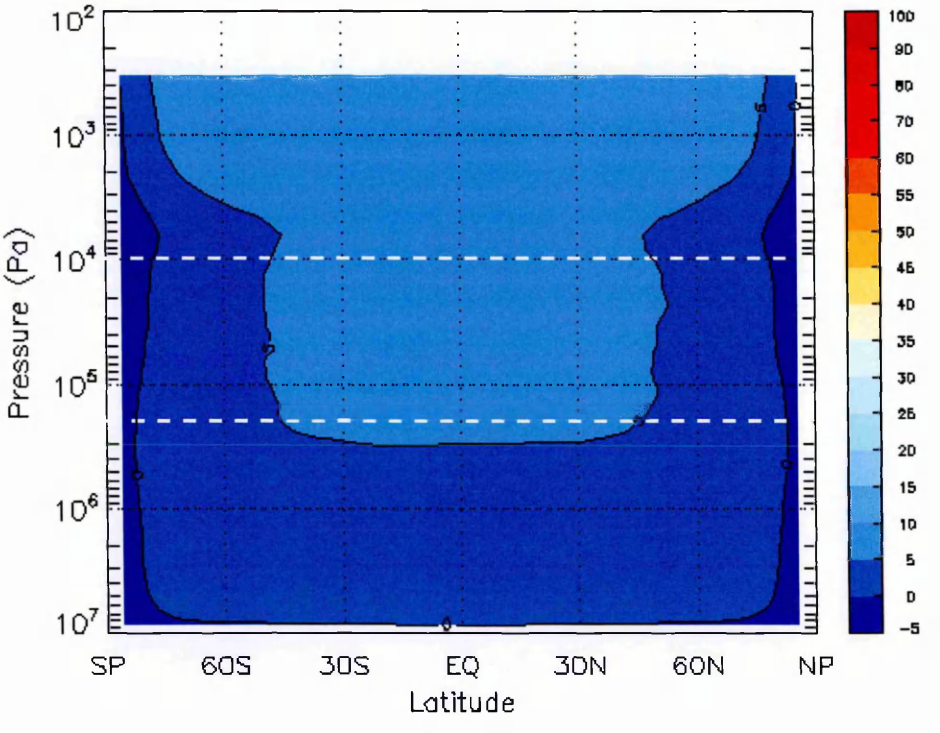

Figure 5.3: Plot of s for base run with sponge on eddy terms, averaged over final four Vdays of simulation, dashed lines indicate cloud levels. Note the colour scale used is chosen to be consistent with plots for $\bar{u}$.

5.1.4 Mean Meridional Circulation

The mean meridional circulation (MMC), also known as the mass stream function, is plotted on figure 5.4. The simulation has developed a large Hadley cell in each hemisphere, ranging from the equator to high latitudes close to the poles, as expected from theory (Held and Hou, 1980) and previous modelling for slowly rotating planets (see Covey et al., 1986). A much weaker circulation is seen close to the poles (latitude above $\sim$75°) rotating counter to the large low latitude cell, perhaps indicative of the polar cold collar (Taylor et al., 1980) and the possible atmospheric circulation observed on Venus described in Svedhem et al. (2007).

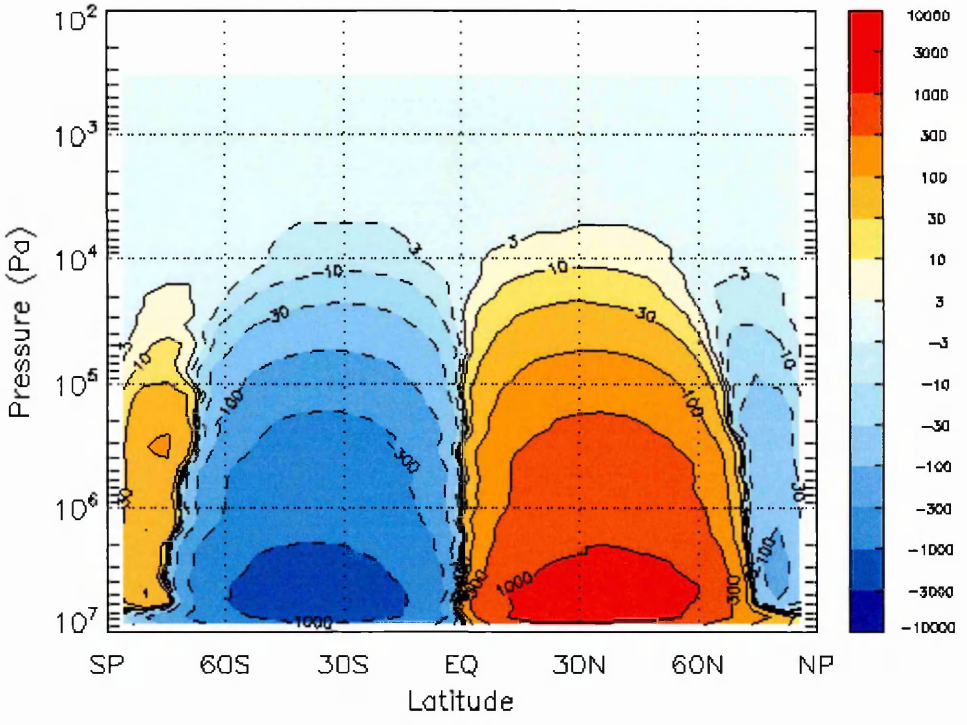

Figure 5.4: Mean Meridional Circulation for base run with sponge on eddy terms, averaged over final four Vdays of simulation.

5.1.5 Temperature anomaly

The temperature anomaly, ΔT, is shown in figure 5.5. This plot shows that cold poles have developed in the upper atmosphere above the clouds. No evidence is seen for the observed warm poles (Schofield and Taylor, 1983) and cold collar (Taylor et al., 1980) in this plot.

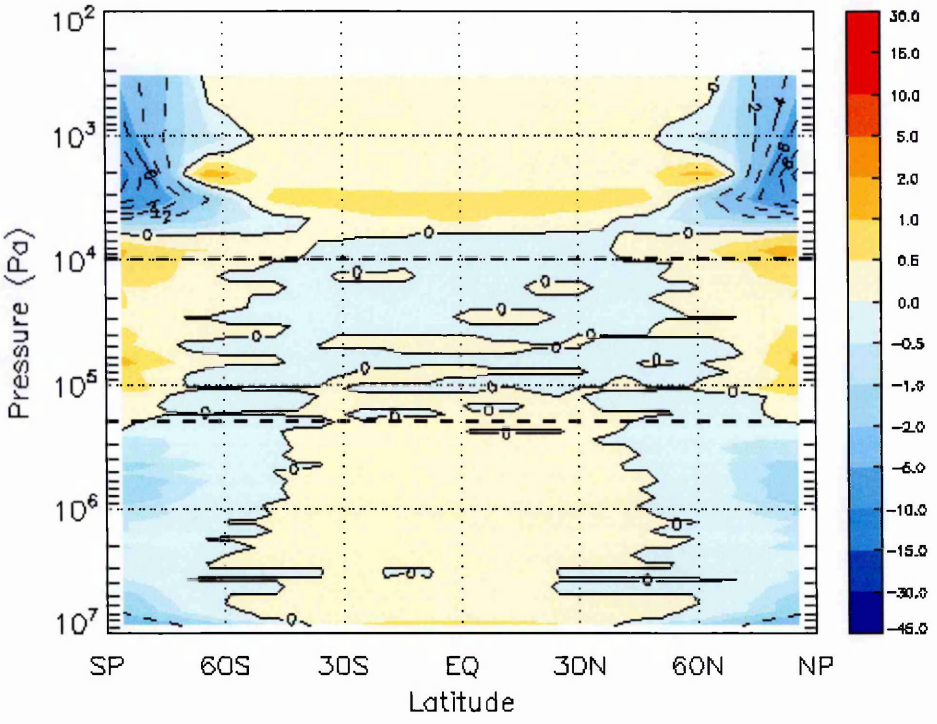

Figure 5.5: ΔT for base run with sponge on eddy terms, averaged over final four Vdays of simulation, dashed lines indicate cloud levels.

5.2 Base run with sponge layer on all terms

5.2.1 Atmospheric Angular Momentum

The time evolution of S (figure 5.6) shows a very similar profile to the sponge on eddies simulation. There is a small amplitude (0.15), long term (70 Vday) periodic variation in S, however an equilibrium has been reached with a value around 4.3. Equilibrium is achieved after approximately 90 Vdays, slightly faster than the sponge on eddies simulation.

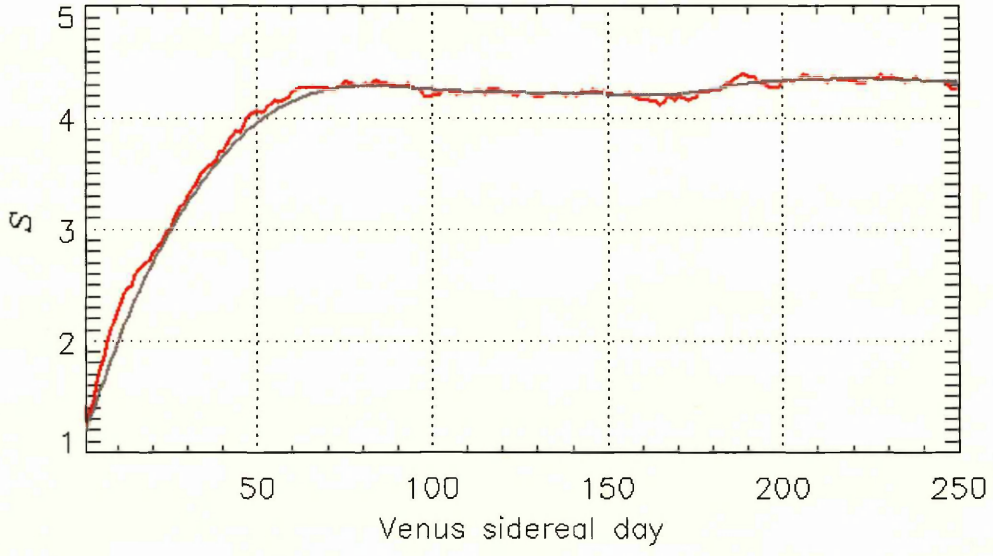

Figure 5.6: Time evolution of S for base run with sponge on all terms

5.2.2 Zonal Wind

Comparison of the results for zonal wind to those obtained using the same conditions but with the sponge layer applied to all terms (figure 5.7) shows a similar profile to the wind development below the cloud tops with winds of $< 20\ \mathrm{m\,s^{-1}}$ except for an area at 75° in the northern hemisphere at the cloud base where the wind speed is above 20 $\mathrm{m\,s^{-1}}$.

However above the clouds the winds are close to zero and even slightly negative (a negative wind is one flowing eastward, the prevailing flow on Venus is westward). The jet features seen in the simulation with the sponge layer applied only to eddy terms are absent. Significant features of the atmospheric circulation, such as the jets, are being suppressed when the sponge layer is applied to all terms when using these settings.

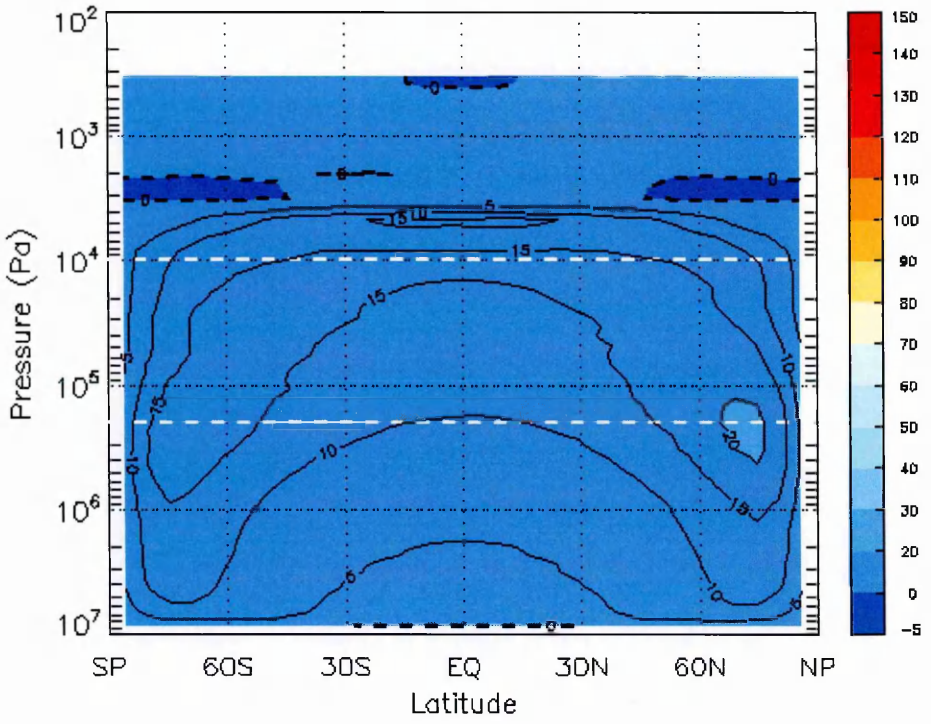

Figure 5.7: Zonal wind for base run with sponge on all terms, averaged over final four Vdays of simulation, dashed lines indicate cloud levels, dashed contours indicate $\bar{u} \leq 0\ \mathrm{m\,s^{-1}}$.

5.2.3 Local super-rotation index

The local super-rotation index s (figure 5.8) shows a super-rotation peak of 8.8 between $\pm 45°$ latitude within the cloud layers and slightly above the clouds. The super-rotation above 4×10^4 Pa is zero - or even slightly negative - due to the very low winds above this level.

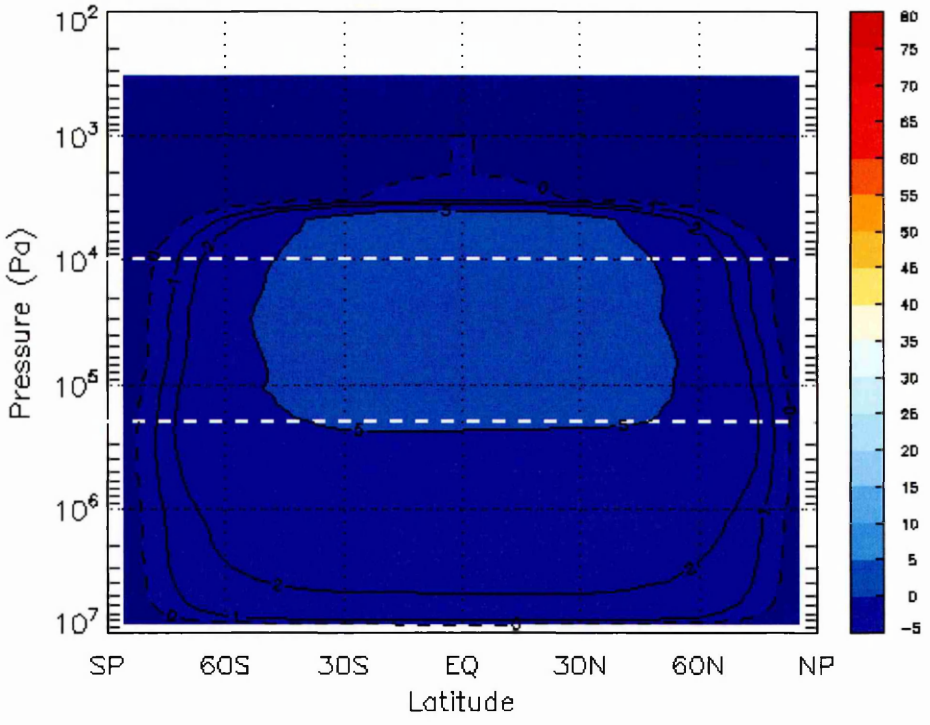

Figure 5.8: Plot of s for base run with sponge on all terms, averaged over final four Vdays of simulation, dashed lines indicate cloud levels.

5.2.4 Mean Meridional Circulation

The MMC is shown in figure 5.9. With the sponge layer on all terms the MMC is broadly unchanged from the simulation with the sponge layer on only eddy terms. Once again there is a large low latitude Hadley cell in each hemisphere and smaller, counter rotating polar cells.

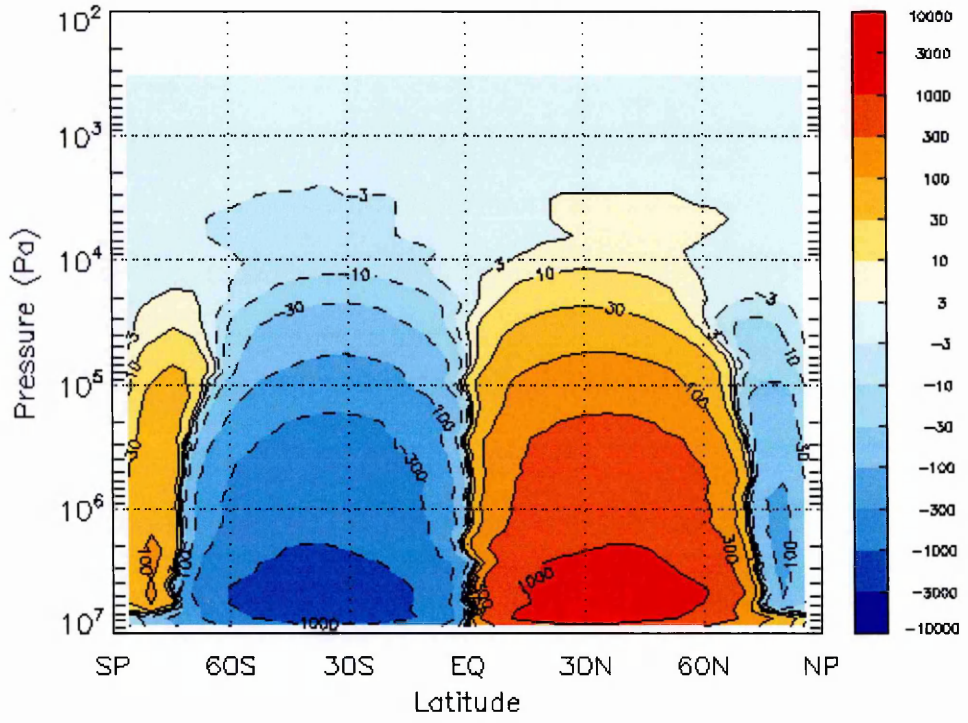

Figure 5.9: Mean Meridional Circulation for base run with sponge on all terms, averaged over final four Vdays of simulation.

5.2.5 Temperature anomaly

The temperature anomaly for the simulation with the sponge layer on all terms is shown in figure 5.10 and does show differences from the sponge layer on eddies simulation. A small amount of warming (<1 K) can be seen near the poles within and above the clouds. All variation is suppressed above $\sim 3 \times 10^3$ Pa. The upper atmosphere cold poles have not developed in this simulation.

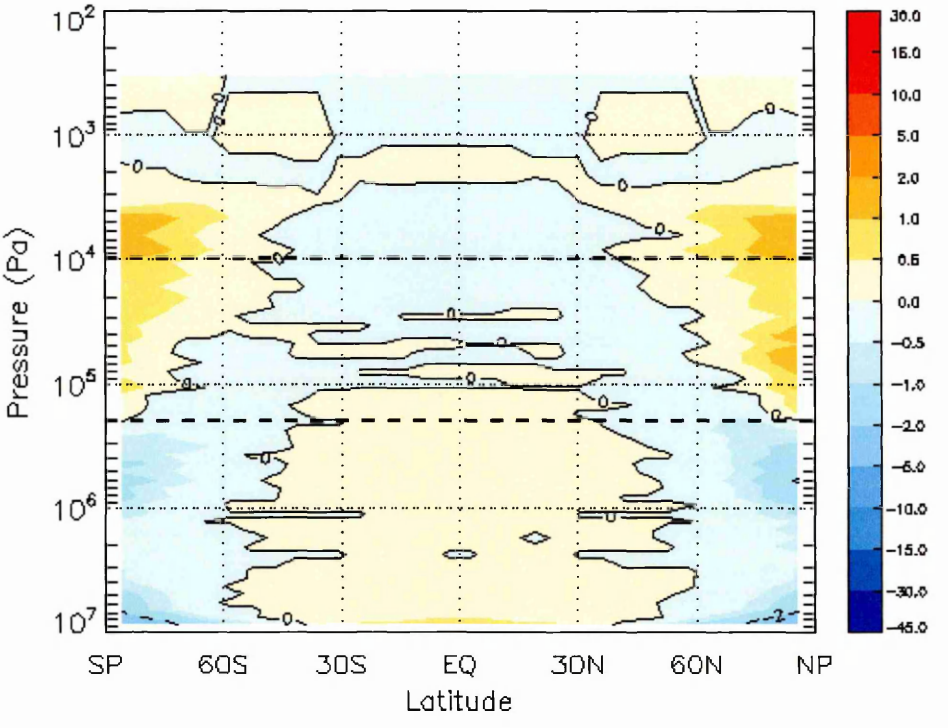

Figure 5.10: ΔT for base run with sponge layer on all terms, averaged over final four Vdays of simulation, dashed lines indicate cloud levels.

5.3 Summary of reference simulations

In this section results were presented for simulations using planetary parameters (radius, gravity, rotation rate and gas constant) appropriate for Venus. The temperature forcing was set by a simplified linear thermal relaxation scheme based on that used by Lee (2006). The VSGCM was set to use 50 vertical levels with sigma levels from

the L-H scheme. Restoration timescales were set as described in section 4.5.7 where values for the Rayleigh friction parameterization are also shown. The 'sponge' layer was set for the top 4 levels, and results were presented for simulations with the sponge layer operating only on the eddy terms of the flow and operating on all terms. The simulations were run for 250 Venus sidereal days.

For the simulation with the sponge layer on eddies only the zonally averaged zonal wind, $\bar{u}$, showed super-rotating winds with a maximum speed of $> 50\ \mathrm{m\,s^{-1}}$, in two jets at high latitudes in the upper atmosphere. Overall wind speed was much weaker than observed on Venus. Zonal wind results with the sponge layer on all terms showed very similar winds to the sponge on eddies simulation below the sponge layer. However in the upper atmosphere the winds were close to zero and the jets no longer evident.

The sponge layer is intended to prevent wave reflections from the model top, however when using these values for the sponge layer and setting it to operate on all terms the winds above the clouds are damped to zero. As noted in section 4.5.7 other researchers have used different restoration and friction timescales for the sponge layer and set it to act on eddy components of the flow. Due to these reasons following simulations will use the sponge layer set to operate on eddies only

Plots of the MMC showed similar flow and vertical profiles for both simulations with a large Hadley cell in each hemisphere, flow rising at the equator, flowing poleward at all levels, descending at high latitude and returning to the equator close to the surface. A second weaker cell was seen in each hemisphere counter-rotating to the main cell and confined to polar latitudes.

Diagnostic plots for s showed no significant super-rotation was achieved for either simulation, as expected from the wind results. s for the sponge on all terms simulation was suppressed close to zero in the sponge layer, the maximum s was equatorial in latitude and at the level of the cloud tops.

Graphs of the evolution of S showed both the simulations had reached equilibrium. Taking ~ 100 Vdays for the sponge layer on eddies and ~ 90 Vdays in the sponge on all terms simulation. Both simulations achieved the same value for S and the time evolution profile was very similar.

Temperature anomaly for the sponge on eddies simulation was shown with cold poles in the upper atmosphere. With the sponge layer on all terms < 1 K variation, above the cloud base at 2×10^5 Pa, was seen.

Lee et al. (2007) used a modification of the UK Meteorological Office Hadley Centre Atmospheric Model, HadAM3, a finite difference, grid-point model run with $5° \times 5°$ horizontal resolution which is approximately equivalent to the T21 model used for this study. With 32 vertical levels Lee et al. (2007) found a peak equatorial wind speed of $\simeq 35\ \mathrm{m\,s^{-1}}$. A strong meridional circulation was developed in the form of a single Hadley cell in each hemisphere. Zonal jets were produced with a maximum speed of $45\ \mathrm{m\,s^{-1}}$ at 60 km in each hemisphere at mid latitudes, with a peak equatorial wind of $35\ \mathrm{m\,s^{-1}}$, as shown in figure 3.3. This GCM also produced significant warm pole and cold collar features.

Yamamoto and Takahashi (2003b) used a T21 Spectral model with 50 vertical levels set for Venus parameters (see 3.3.5). Using this model the resulting wind speed achieved peaked at $100\ \mathrm{m\,s^{-1}}$ in two jets.

5.4 Topography

The surface of Venus was comprehensively radar mapped by the Magellan mission, using the synthetic aperture radar it carried (Saunders et al., 1990). A topographical map generated using those data, figure 5.11, is also marked with the significant surface features. The map has been coloured to indicate surface elevation with red for the highest levels, e.g. Ishtar Terra in the northern hemisphere ($\geq$ 8 km), yellow for highland regions ($\geq$ 4 km) and blue for the lower lying plains (-2 — +2 km). Note: The blue of the plains does not indicate the presence of water oceans.

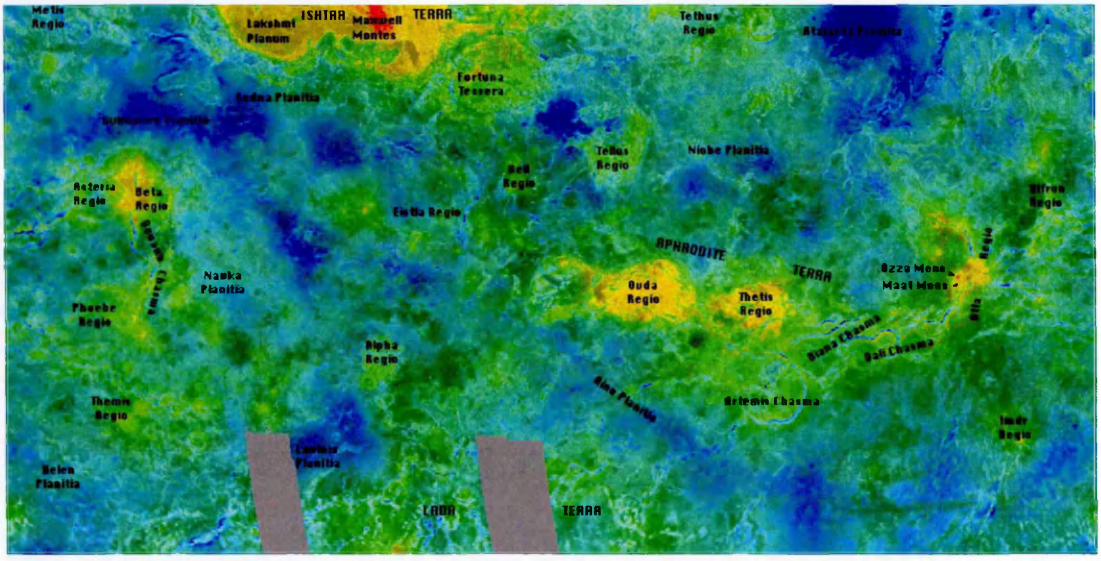

Figure 5.11: Topographic map of the Venusian surface.

The dense cloud cover on Venus had prevented Earth bound observers from observing the geological nature of the surface. Developments in radar telescopes and radar imaging systems orbiting the planet have made it possible to see through the cloud deck to the surface below. Four of the most successful missions in revealing the Venusian surface were NASA's Pioneer Venus mission (1978), the Soviet Union's Venera 15 and 16 missions (1983-1984), and NASA's Magellan radar mapping mission (1990-1994). As these spacecraft began radar mapping the planet the topographical details emerged.

The surface of Venus is relatively young geologically speaking and appears to have been completely resurfaced 300 to 500 million years ago. The Venusian topography consists of vast plains covered by lava flows and mountain or highland regions deformed by geological activity. Maxwell Montes in Ishtar Terra, in the Northern hemisphere, is the highest peak on Venus at 11 km above the mean elevation. The Aphrodite Terra highlands extend almost half way around the equator. The Magellan images of highland regions above 2.5 km are unusually radar bright, characteristic of a moist soil, however liquid water does not exist on the surface and so generally cannot account for the bright highlands. One theory suggests that the bright material might be composed of metallic compounds, such as iron pyrite also known as 'fools gold' (Fegley et al., 1997).

Venus is scarred by many impact craters distributed randomly over its surface. Small craters of less than 2 km are relatively rare, as the impactors burn up in the dense atmosphere. The exception occurs when large meteorites shatter just before impact, creating crater clusters.

Volcanoes and volcanic features are numerous with at least 85% of the surface covered with volcanic rock. Samples taken by the Venera 13 and 14 landers indicated a composition similar to leucite basalt found on the Earth. Huge lava flows have flooded the lowlands creating vast plains. More than 100,000 small shield volcanoes dot the surface along with hundreds of large volcanos. Lava flows from volcanos have produced long sinuous channels extending for hundreds of kilometers, with one extending nearly 7,000 km.

Giant calderas more than 100 km in diameter are found on Venus, in comparison calderas on Earth are usually only a few kilometers in diameter. Several features unique to Venus include coronae and arachnoids. Coronae are large circular to oval features, encircled with cliffs and are hundreds of kilometers across, thought to be the

surface expression of mantle upwelling. Arachnoids, so called due to their spider and cobweb like appearance, are circular to elongated features similar to coronae, which may have been caused by molten rock seeping into surface fractures and producing systems of radiating dykes and fractures.

5.4.1 Topography data

A high resolution topographical dataset, generated from data obtained from the Magellan spacecraft's radar mapping of Venus (Ford and Pettengill, 1992), is available from:

`http://pds-geosciences.wustl.edu/geo/mgn-v-rss-5-gravity-l2-v1/mg_5201/topo/`

The Magellan radar mapping data is presented from an orbit beginning above the ecliptic, hence the North Pole is lowermost in the data set. The data is a $1° \times 1°$ map of the topography of Venus from latitude -89.5° to 89.5°, and longitude from 240° to 240°.

The data set when re-plotted with the North pole uppermost (the Magellan team adopted this convention for all their cartographic products (Davies et al., 1992), a definition of the North Pole for Venus was given in section 4.5.5) and longitude from 0° to 360° shows a more conventional view of the Venus topography. The highest peak on Venus, Maxwell Montes, is upper left (65.2°N, 3.3°E), see figure 5.12.

5.4.2 Results with topography

The Magellan dataset was transformed into spherical harmonic components to make a 'spectral topography' file which could be used by the VSGCM. The VSGCM was then run for a simulation of 250 Vdays using this file. For this run the settings used were those described in section 4.5, with the sponge layer set to operate on eddy terms only. The temperature forcing profile used was N_4. The results for the run were plotted as an average of the final 4 Vdays of the simulation.

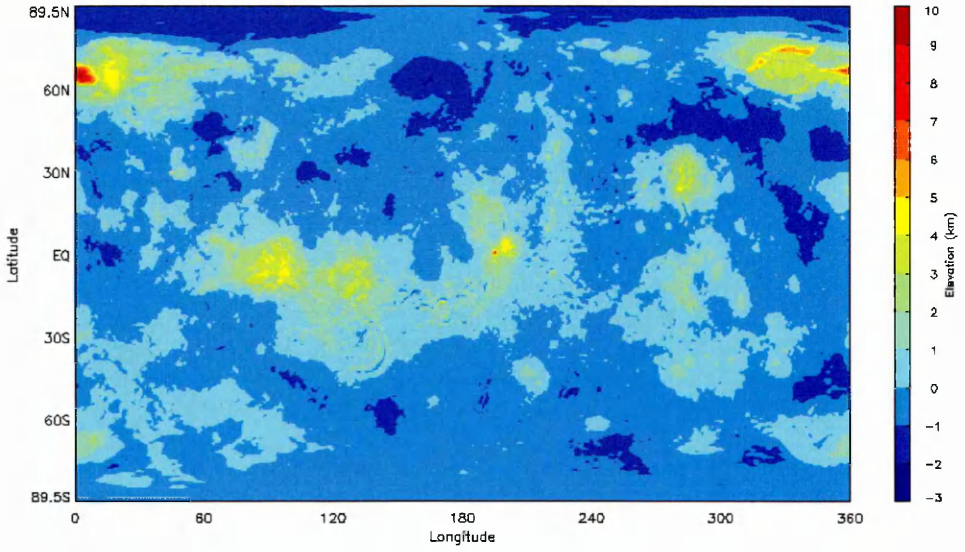

Figure 5.12: Plot of Magellan topographic dataset.

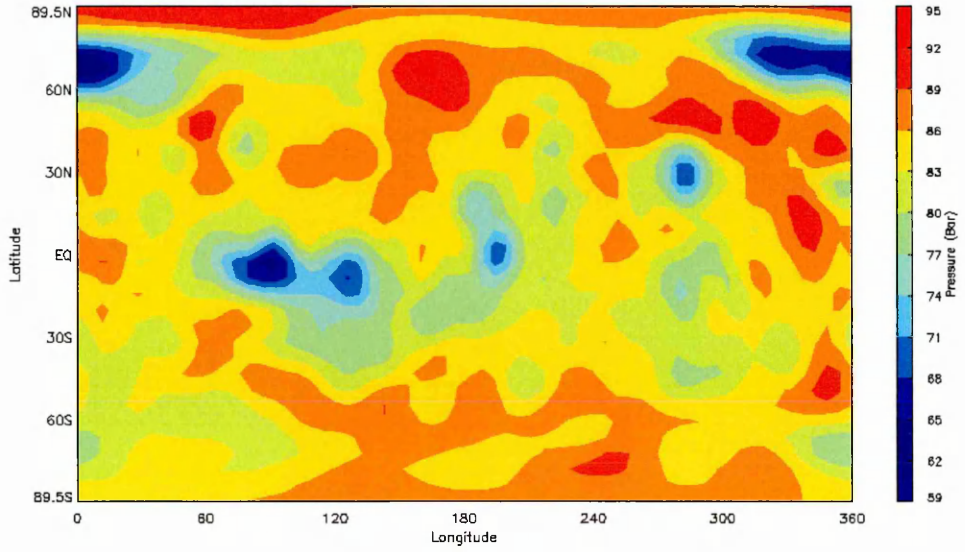

Figure 5.13: Surface pressure for simulation using topography at T21 resolution.

The surface pressure is shown in figure 5.13. The high elevation ground features of Ishtar Terra and Maxwell Montes in the Northern hemisphere of Venus, and Ouda and Thetis Regio at equatorial latitudes, can be seen in the plot as regions of reduced surface pressure.

5.4.3 Atmospheric Angular Momentum

The time development of S is shown in figure 5.14, the black line on the graph shows the evolution of S for the simulation with topography, with equilibrium reached very early in the simulation in ~ 20 Vdays, at a relatively low magnitude of 1.5. The reference simulation is also shown on the graph for comparison, as a dashed line, where equilibrium was reached in ~ 100 Vdays with a magnitude of 4.3.

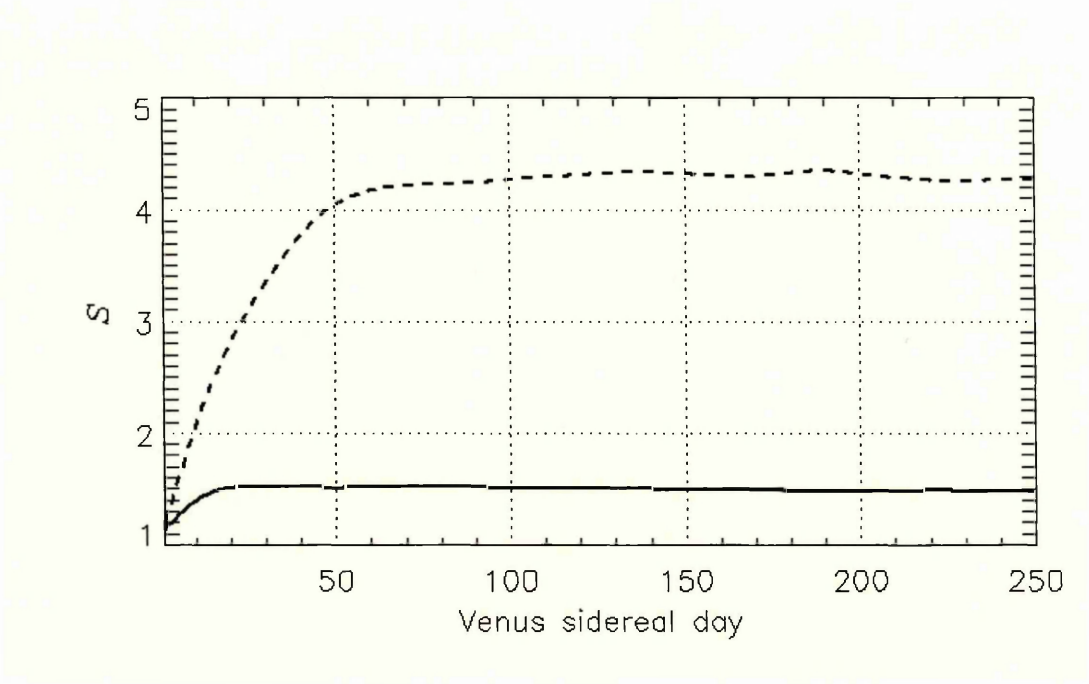

Figure 5.14: Time development of S. Solid line - with topography, dashed line - reference run without topography

5.4.4 Zonal wind

Figure 5.15 shows the $\bar{u}$ result. This plot is very similar to the initial reference run (figure 5.2) despite the much lower S developed. Maximum wind speeds for the experiment with topography are in two jets at the top of the atmosphere and the high latitude of $\pm 75°$. The maximum wind speed achieved was 57.1 $\mathrm{m\,s^{-1}}$, similar to the reference simulation where the maximum wind speed was 57.9 $\mathrm{m\,s^{-1}}$. The wind in the lower atmosphere is reduced compared to the reference simulation and shows areas of negative (eastward) wind below $\sim 10^6$ Pa (~ 28 km). The negative winds and reduced wind speed in the lower atmosphere when using topography are likely due to the additional drag resulting from the high level terrain close to the equator and the influence of the highest point on Venus, Maxwell Montes and Ishtar Terra.

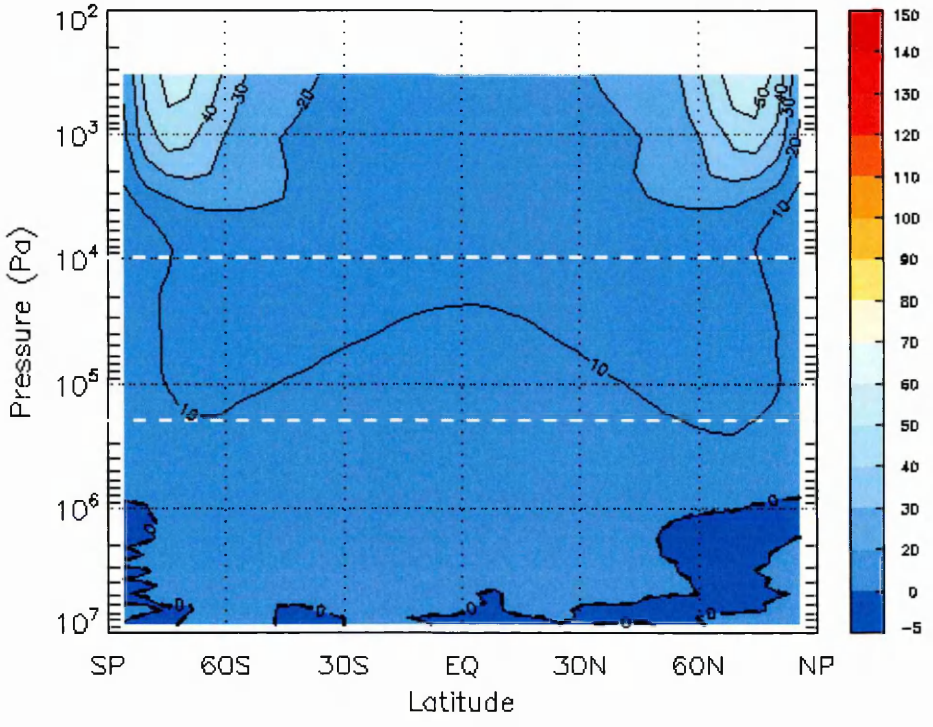

Figure 5.15: Zonal wind for simulation with topography, averaged over four Vdays, dashed lines indicate cloud levels, dashed contours indicate $\bar{u} \leq 0\ \mathrm{m\,s^{-1}}$.

The differences in zonal wind are highlighted in the plot at figure 5.16 which shows the result when the $\bar{u}$ output from the simulation with topography has the $\bar{u}$ from the reference simulation (figure 5.2) subtracted from it. From this plot it can be seen that the difference in winds above the cloud top show several areas with slightly higher wind speeds ($\sim 5\ \mathrm{m\,s^{-1}}$ maximum) for the simulation with topography, although generally the zonal wind above the cloud base is similar to the reference simulation. The main differences are low in the atmosphere at pressures greater than 10^5 Pa (50 km) and below the cloud layer. Wind speeds throughout the lower atmosphere are slightly reduced ($\leq 10\ \mathrm{m\,s^{-1}}$) when the reference simulation is subtracted with larger reductions ($\geq 10\ \mathrm{m\,s^{-1}}$) in two areas at high latitudes. At equatorial latitudes the wind speed for the simulation with topography is $\sim 5\ \mathrm{m\,s^{-1}}$ less.

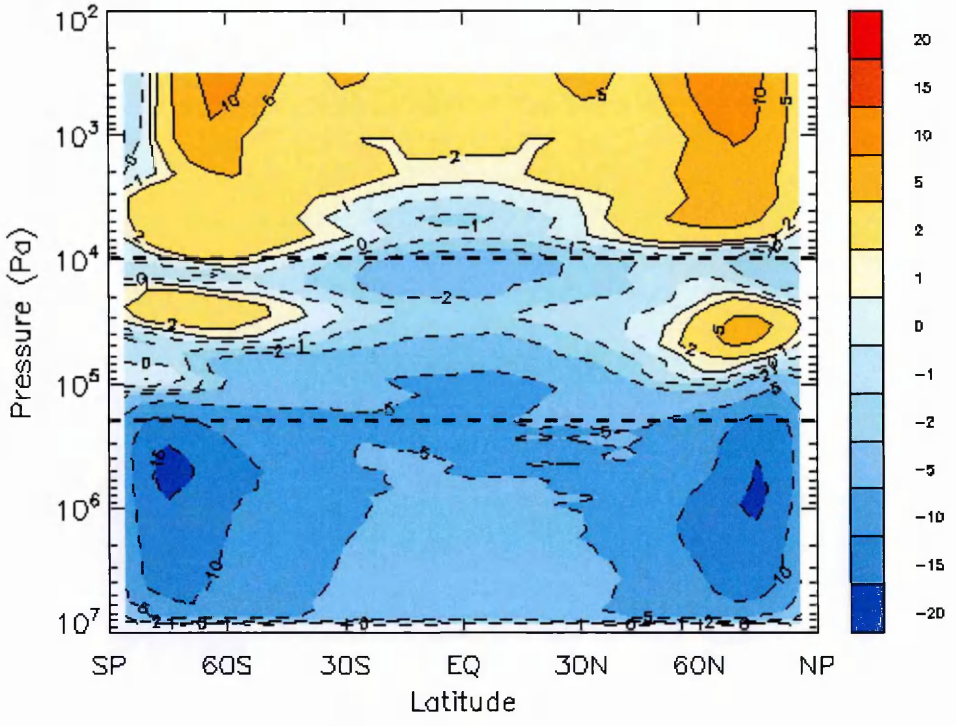

Figure 5.16: $\bar{u}$ with topography - $\bar{u}$ reference without topography, averaged over four Vdays, dashed lines indicate cloud levels.

5.4.5 Local super-rotation index

The local super-rotation index is shown in figure 5.17. This plot is again similar to the reference simulation, shown in figure 5.3, and shows a small (5-10) magnitude for s in the upper atmosphere with a peak of 10.3.

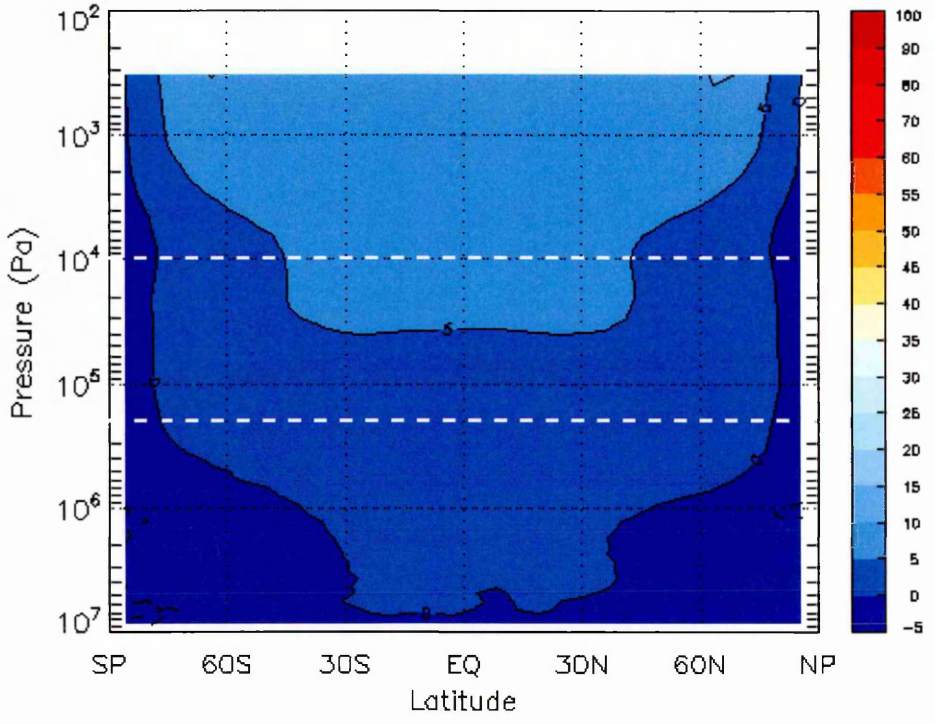

Figure 5.17: s for simulation with topography, averaged over four Vdays, dashed lines indicate cloud levels.

5.4.6 Mean Meridional Circulation

The mean meridional circulation, MMC, is shown in figure 5.18. The simulation with topography has produced two Hadley cells, one in each hemisphere. The MMC developed is much stronger than the reference simulation with a range from -5495 to 4815 kgs^{-1}, the reference simulation developed -1830 to 1865 kgs^{-1}. Two small indirect cells have developed in the northern hemisphere at approximately 50° and 70° below $\sim 10^6$ Pa, linked to the high terrain of Maxwell Montes at 65.2° N and Ishtar Terra.

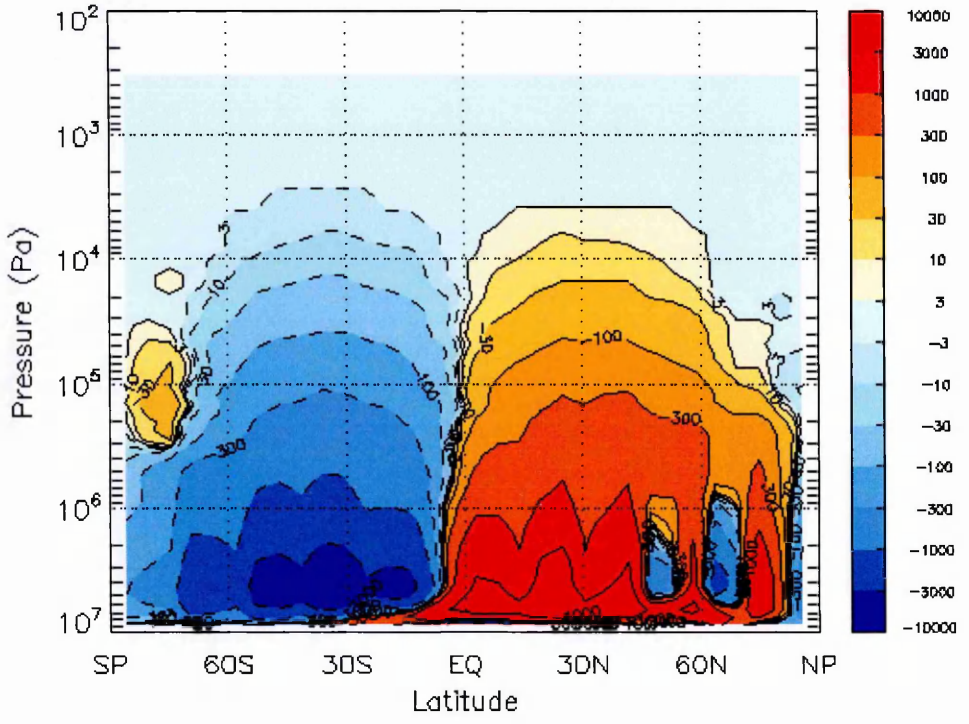

Figure 5.18: MMC for simulation with topography

5.5 Summary of topography experiments

In this section results were presented for a simulation made when using topography. The section began with information about the topography on Venus. This was followed by a description of the topographical data set from radar mapping by the Magellan satellite mission. The Magellan topographical data was used to generate a spectral topography file suitable for use by the VSGCM. The VSGCM was then run for a simulation using nominal settings and this topography file.

The magnitude of globally integrated angular momentum was very much less for the run using topography than that achieved by the initial reference run. The time taken to achieve equilibrium was shorter for the topography simulation, taking less than 20 Vdays rather than $\sim$ 100 Vdays for the reference run. Herrnstein and Dowling (2007) also found the time to reach equilibrium reduced when using topography.

The zonal winds generated by this simulation were presented. The plot showed very similar winds to the reference simulation in the upper atmosphere, however closer to the surface the influence of the topography could be seen with a larger region of retrograde winds. A plot of the difference between the wind generated by this simulation and the reference simulation showed that the wind speed had reduced in the majority of the atmosphere. The largest reduction, $\geq$ 15 $\mathrm{m\,s^{-1}}$, was below the clouds where the greatest mass of atmosphere is present. This reduction explains the difference in angular momentum between the topography experiment and the reference run.

The winds obtained with this simulation are in contrast to the results of Herrnstein and Dowling (2007) who found the zonal wind peak reduced when topography was added to the model they used for their simulations. Their peak wind was found in two jets which were lower in the atmosphere than those in the VSGCM, between approximately 10^4 and 10^5 Pa, within the cloud layers. Herrnstein and Dowling (2007) also found the jets to be asymmetric.

The LMDZ Venus GCM used by Lebonnois et al. (2010) using simplified radiative forcing and including topography developed a higher peak wind speed of over 40 $\mathrm{m\,s^{-1}}$. Without topography the model developed less than 40 $\mathrm{m\,s^{-1}}$.

This VSGCM simulation also produced a very strong MMC. Compared to the reference simulation the circulation was similar with hemispheric Hadley cells however the magnitude was significantly enhanced with topography ranging from -5495 to 4815 $\mathrm{kgs^{-1}}$, the reference simulation developed -1830 to 1865 $\mathrm{kgs^{-1}}$. Three indirect cells were seen due to the influence of the high surface features in Venus' Northern hemisphere.

The following chapter presents results for simulations with higher temperatures used for the global mean background temperature profile. In the final sections of the next chapter the addition of a simple diurnal cycle is described and results presented.

Chapter 6

Modified background stability & diurnal cycle

In the first three sections of this chapter the effect of changing the global-mean background temperature profile used to generate the restore state, the forcing profile, are investigated. In the following two sections the inclusion of a diurnal cycle is described. The results from an experiment using the diurnal cycle are presented.

Simulations were made using thermal forcing profiles with modified background stability (MBS), where the global-mean background temperature profile was increased over the standard N_4 forcing described in section 4.4. For the modified profiles the surface temperature remains fixed at the same value (735K) and the temperature increases more rapidly with height than it does in the nominal N_4 forcing state (section 4.4). The arbitrarily chosen maximum increase in temperature for the forcing profiles tested was 21K for N_5 , 42K for N_6 and 84K for N_9 .

For the MBS simulations the vertical temperature profiles tested are shown in figure 6.1. The equator-pole temperature difference was maintained at the same values in all cases. For these simulations the VSGCM was configured as described in section 4.5 and with 50 vertical levels. The model was run for a total simulation of 500 Vdays and diagnostics were produced at the end of the simulation.

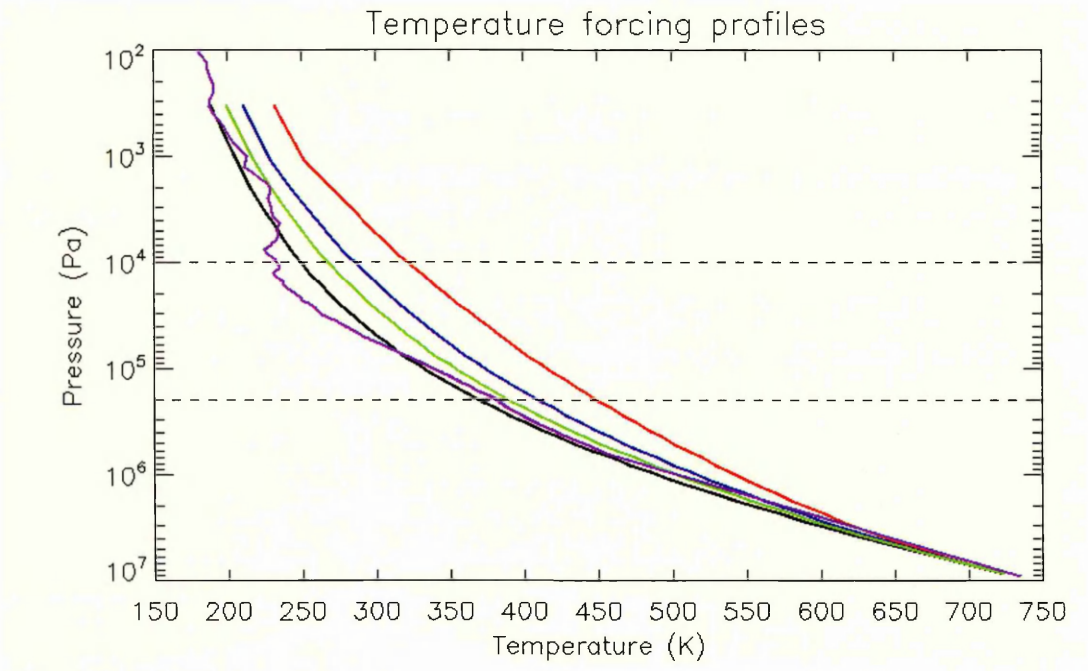

Figure 6.1: Vertical profiles of thermal forcing tested.
Black N_4 ; Green N_5 ; Blue N_6 ; Red N_9 ; Purple Magellan satellite data included for reference. Dashed lines indicate cloud heights

6.0.1 Stability

The Brunt-Viäsälä frequency, or buoyancy frequency, is the angular frequency at which a vertically displaced parcel of atmosphere will oscillate within a statically stable environment. It is given by:

$$N = \sqrt{\frac{g}{\Theta}\frac{d\Theta}{dz}} \tag{6.1}$$

where Θ is the potential temperature.

A measure of the stability of an atmosphere is given by N^2. If $N^2 > 0$ a parcel of atmosphere will oscillate about its initial level and the atmosphere is stable. If $N^2 < 0$ the parcel of atmosphere's displacement will increase and the atmosphere is unstable. N^2 was calculated for all four profiles tested and is plotted in figure 6.2. It can be seen from the graph that the lower atmosphere becomes increasingly stable as

the forcing temperature is increased. The different profiles are labelled by their value of N^2 at 10^6 Pa. The values of N^2 at 10^6 Pa are shown in table 6.1.

Table 6.1: Values of N^2 at $p = 10^6$ Pa

Profile label	$N^2(10^{-5}\ \mathrm{s}^{-1})$
N_4	3.6
N_5	4.9
N_6	6.3
N_9	8.9

The static stability profiles also give the name to the thermal forcing profiles used in this chapter, Modified Background Stability.

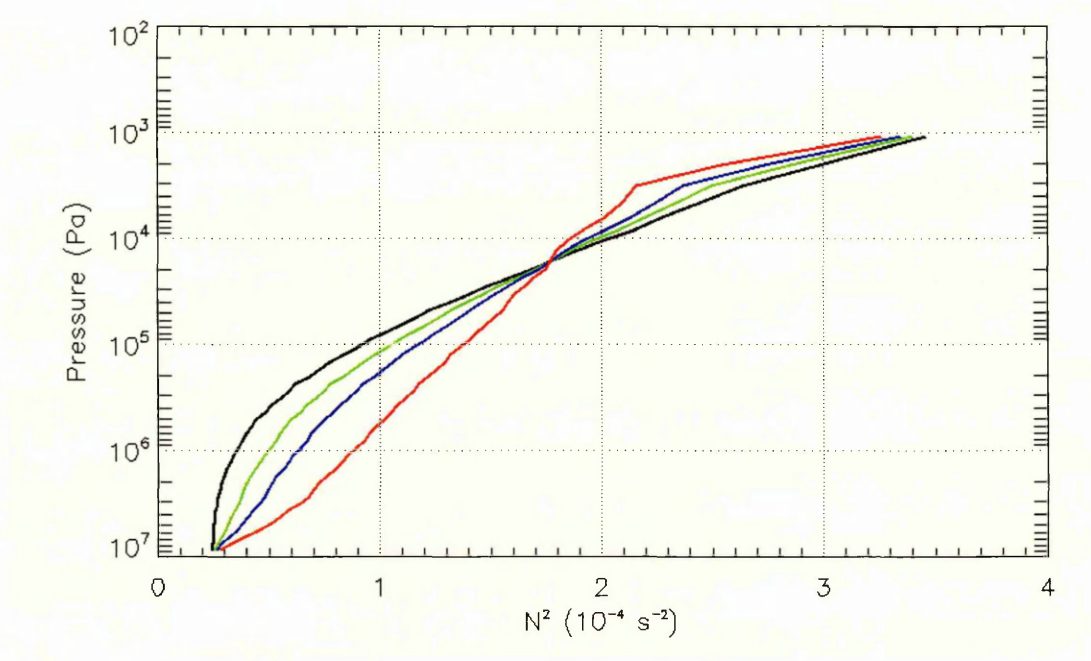

Figure 6.2: Brunt-Viäsälä frequency squared, N^2
Black N_4 ; Green N_5 ; Blue N_6 ; Red N_9

6.1 T21 experiments with modified background stability forcing

The thermal forcing profiles with modified background stability (MBS) were first tested at T21 horizontal resolution. The simulations were run for 500 Vdays. At the end of the simulation time diagnostics were produced for zonal wind ($\bar{u}$), local super-rotation index (s), mean meridional circulation (MMC), and temperature anomaly (ΔT).

6.1.1 Atmospheric angular momentum

The time development of S for the forcing states tested is shown in figure 6.3. It can be seen that an increased forcing temperature, and stability, results in both a larger value for S and a longer time taken to reach an equilibrium state. Table 6.2 summarises the time taken to reach equilibrium and the value for S at 500 Vdays.

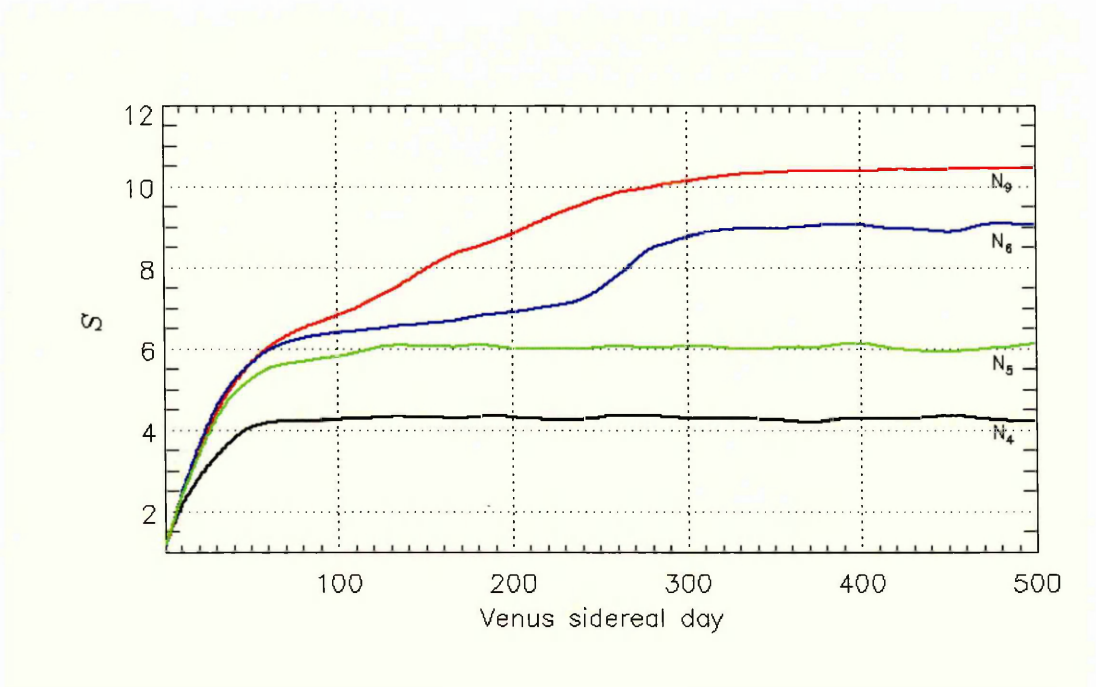

Figure 6.3: Time development of S with modified stability forcing.
Red line, N_9 ; Blue, N_6 ; Green, N_5 ; Black, N_4 .

All the forcing states begin development of S in a similar manner showing identical growth up to 10 Vdays when the N_5, N_6 and N_9 experiments continue to grow at the same rate until approximately 30 Vdays. S in the N_6 and N_9 experiments then continues to grow at the same rate until ~ 60 Vdays. All the simulations appear to have reached, or be close to, equilibrium at 100 Vdays, however S in all the experiments except N_4, which has reached equilibrium, continue to grow further.

The N_6 forcing simulation appears to be close to an equilibrium value from ~ 60 Vdays with the rate of change of S reducing, but the rate of change increases sharply between approximately 240 and 280 Vdays before reducing again and reaching the final equilibrium value at around 310 Vdays. The N_9 forcing experiment grows steadily from 60 Vdays until achieving equilibrium at ~ 400 Vdays.

Table 6.2: Equilibrium times and Values

Profile label	**Equilibrium time Vdays**	***S* value after 500 Vdays**
N_4	50	4.36
N_5	130	6.11
N_6	310	9.07
N_9	400	10.46

6.1.2 Zonal wind

The zonally averaged zonal wind ($\bar{u}$) for all four of the temperature states tested are shown in figure 6.4. The zonal winds increase as the forcing temperature (stability) is increased. The closest to the observed wind speeds were found for N_5 forcing at approximately 90 $\mathrm{m\,s^{-1}}$ at the cloud tops.

Using the N_4 forcing state equilibrium was reached in approximately 100 Vdays. The wind was weaker than observed with two high altitude high latitude jets. The peak wind speed in the jets was $\sim 50\ \mathrm{m\,s^{-1}}$.

The N_5 forcing experiment had reached equilibrium at approximately 130 Vdays. The winds had developed a peak above, and at the top of the cloud layer. Two jets were present between 30° and 60° in each hemisphere which were at lower altitude and lower latitude than the jets in the N_4 experiment. The peak wind speed in the jets was 93 $\mathrm{m\,s^{-1}}$, close to the observed value for the zonal winds on Venus (Peralta et al., 2007; Sánchez-Lavega et al., 2008).

Zonal winds when using N_6 forcing show a further increase in speed. For this experiment the strongest winds are at the cloud top level with the jets strengthening over the N_5 simulation. The peak wind speed in the jets was 142 $\mathrm{m\,s^{-1}}$.

The N_9 forcing simulation shows the highest wind speed for the temperature states tested. The winds in this simulation reached peak speeds of 150 $\mathrm{m\,s^{-1}}$ at 500 Vdays.

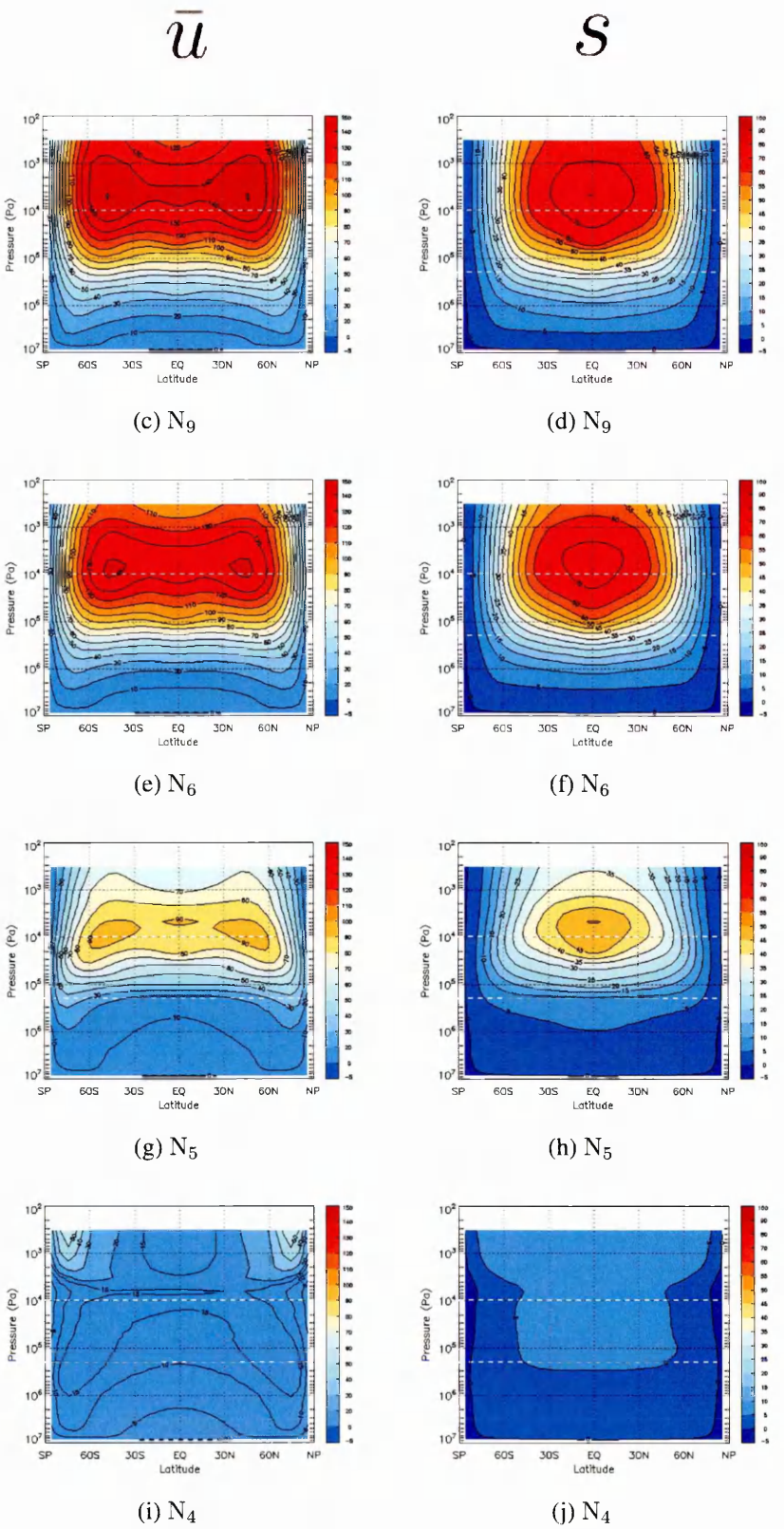

(c) N_9 (d) N_9

(e) N_6 (f) N_6

(g) N_5 (h) N_5

(i) N_4 (j) N_4

Figure 6.4: Zonal wind ($\bar{u}$) and local super-rotation index (s) for MBS forcing states at 500 Vdays, averaged over the final four Vdays, dashed lines indicate cloud levels.

6.1.3 Local super-rotation index

The local super-rotation index (s) was calculated for all the experiments performed with these temperature (stability) states and plots of s are shown together with $\bar{u}$ in figure 6.4. As with the zonal wind the super-rotation index increases as the forcing profile temperature and stability increases.

The N_4 forcing experiment shows only weak super-rotation with the maximum values in an area between $\pm 45°$, within the cloud layer and extending above. The maximum value of s was 9.3.

The N_5 experiment produced a zonal wind pattern which was closer to the observed value for Venus and thus shows more super-rotation than N_4. A definite peak is evident at the equator, slightly above the cloud top. The peak value was 50.5, close to the value of 60 calculated from the observed winds (Sánchez-Lavega et al., 2008).

When using N_6 forcing the stronger wind generated by this simulation leads to a higher s, again peaking at the equator and just above the cloud tops. After 500 Vdays the maximum had increased to 77.1.

The N_9 experiment developed s which was stronger still with a peak at 500 Vdays of 80.0.

6.1.4 Mean meridional circulation

Figure 6.5 shows the mean meridional circulation (MMC) at 500 Vdays. The plots for MMC show a single Hadley cell in each hemisphere, as would be expected from from theory (Held and Hou, 1980). The strength of the MMC reduces as the S and zonal winds increase when the stability for the forcing is increased.

When using the N_4 forcing state the MMC is at its strongest and the hemispheric Hadley cells are well defined throughout the depth of the atmosphere. Narrow areas of counter-rotating flow, much weaker than the main cells, can be seen close to the poles above $\pm 60°$ latitude for all the forcing states tested. As the forcing is increased these counter-rotating cells become weaker, less well defined and reduce in their vertical extent and thicken towards lower latitudes. With N_9 forcing the main cells are significantly flattened and have begun to develop a stacked structure.

The Gierasch (1975) mechanism transports a set amount of angular momentum to the equator which is opposed a transport by the MMC in the poleward direction. As the MMC reduces an 'excess' can build up at the equator, resulting in a higher $\bar{u}$ and a larger gradient in s, as seen in figures 6.4 and 6.5, where the zonal wind speed and local super-rotation index increase as the forcing temperature increases and the MMC reduces.

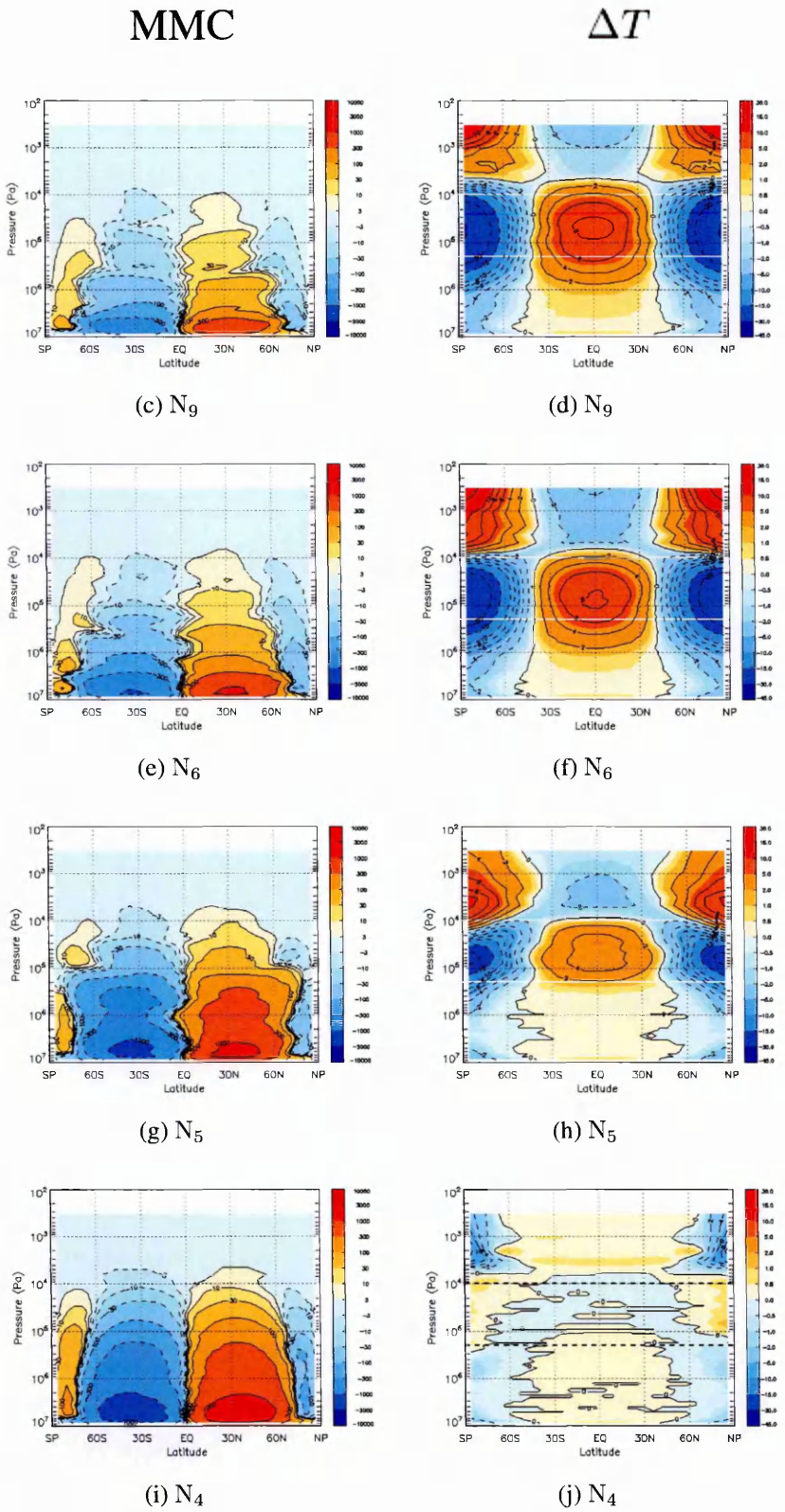

(c) N_9 (d) N_9

(e) N_6 (f) N_6

(g) N_5 (h) N_5

(i) N_4 (j) N_4

Figure 6.5: MMC and temperature anomaly (ΔT) for MBS forcing states at 500 Vdays, averaged over final four Vdays of simulation, dashed lines indicate cloud levels

6.1.5 Temperature anomaly

Also shown in figure 6.5 is the temperature difference from the global mean, ΔT. The plots for ΔT show warm poles in the upper atmosphere above the clouds, at $> \pm 60°$ latitude when using any of the MBS forcing profiles, the N_4 experiment shows only a cold area at the poles and above the clouds. The warm pole seen for the experiments with N_5, N_6 and N_9 forcing develops above the cloud layers rising to the top of the atmosphere as the forcing temperature is increased above the N_4 state. The warm pole peaks in temperature for the N_6 forcing simulation and then reduces slightly for the N_9 forcing experiment.

Warming is also seen within the cloud layers around the equator. The warm area is seen to develop in the N_5 forcing simulation, increasing in temperature for the N_6 and N_9 forcing simulations.

A cold area develops above the clouds, equatorially, at the top of the atmosphere, deepening as the forcing temperature is increased. In addition cold areas also develop mainly within the cloud layers, poleward of $\sim \pm 60°$ latitude, under the upper atmosphere warm poles. These cold areas deepen as the forcing temperature increases.

6.2 T42 experiments with modified background stability forcing

The T42 VSGCM was tested with the four forcing states used for earlier MBS experiments (see section 6.1). For these experiments the VSGCM was run for simulations of 250 Vdays. Results are presented for global atmospheric angular momentum (S), zonal wind ($\bar{u}$), local super-rotation index (s), and mean meridional circulation (MMC).

6.2.1 Atmospheric angular momentum

The time development of global atmospheric angular momentum (S) for the four forcing states tested at T42 is shown in figure 6.6. From this graph it can be seen that all four experiments have reached an equilibrium. The final value of S scales with the temperature and stability of the forcing state with a larger S for a higher temperature and stability forcing state used. The N_5 experiment shows an oscillation around the mean value of 3.5, an oscillation with a magnitude of ~ 0.17.

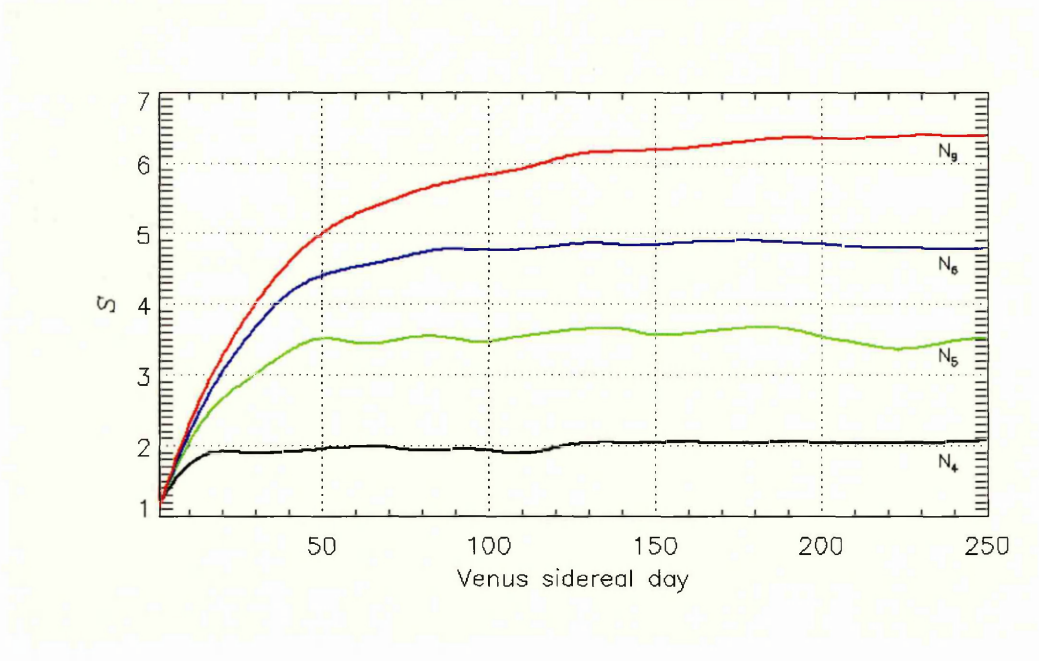

Figure 6.6: Time development of S for T42 with MBS forcing.
Black line, N_4 ; green, N_5 ; blue, N_6 ; red, N_9

6.2.2 Zonal wind

The zonal winds ($\bar{u}$) and local super-rotation index (s) for the T42 experiments using the MBS forcing profiles are shown in figure 6.7. For all the forcing states tested the zonal winds achieve maximum speed in two jets at the top of the atmosphere modelled and at $\pm 60°$ approximate latitude. In contrast to the results found with T21 resolution and shown in section 6.1.2, the wind speed does not increase as the forcing temperature (stability) used increases. For these T42 simulations the maximum wind speed is

highest for the N_4 forcing experiment, reducing for N_5 forcing and reducing further to reach a minimum with N_6 forcing, before increasing slightly with N_9 forcing. The peak values for wind speed are summarised in table 6.3. For all the simulations the jets, and the highest wind speed, are seen above the top of the clouds. Below the cloud tops the wind fields are very similar for all the forcing states with zonal wind speeds of <35 $m\,s^{-1}$. The wind reduces with reducing altitude and reaches zero at the surface. The wind contours show wind speeds lowest at the equator and highest at $\sim 75°$ latitude.

The peak of the jets are at a latitude of approximately 60°, with a small variation in latitude between the different forcing states. When using N_4 forcing the jets are at $\sim 55°$ latitude. When the forcing temperature is increased the jets move poleward, N_6 forcing exhibits the highest latitude jets at approximately 70° where they then move towards the equator as the forcing is further increased to N_9.

6.2.3 Local super-rotation index

The local super-rotation index (s) follows the same pattern as the wind speed results, with maximum s for N_4 forcing, reducing for N_5 forcing, reaching a minimum with N_6 forcing, and then increasing slightly for N_9 forcing. The super-rotation is strongest above the cloud tops and centred at the equator for all the forcing states. The magnitude of s developed in all the T42 experiments are shown in table 6.3.

6.2.4 Mean meridional circulation

The mean meridional circulation is also shown in figure 6.7. It can be seen that the meridional circulation has developed a single Hadley cell in each hemisphere. The MMC is strongest for N_4 forcing reducing in strength as the forcing temperature increases.

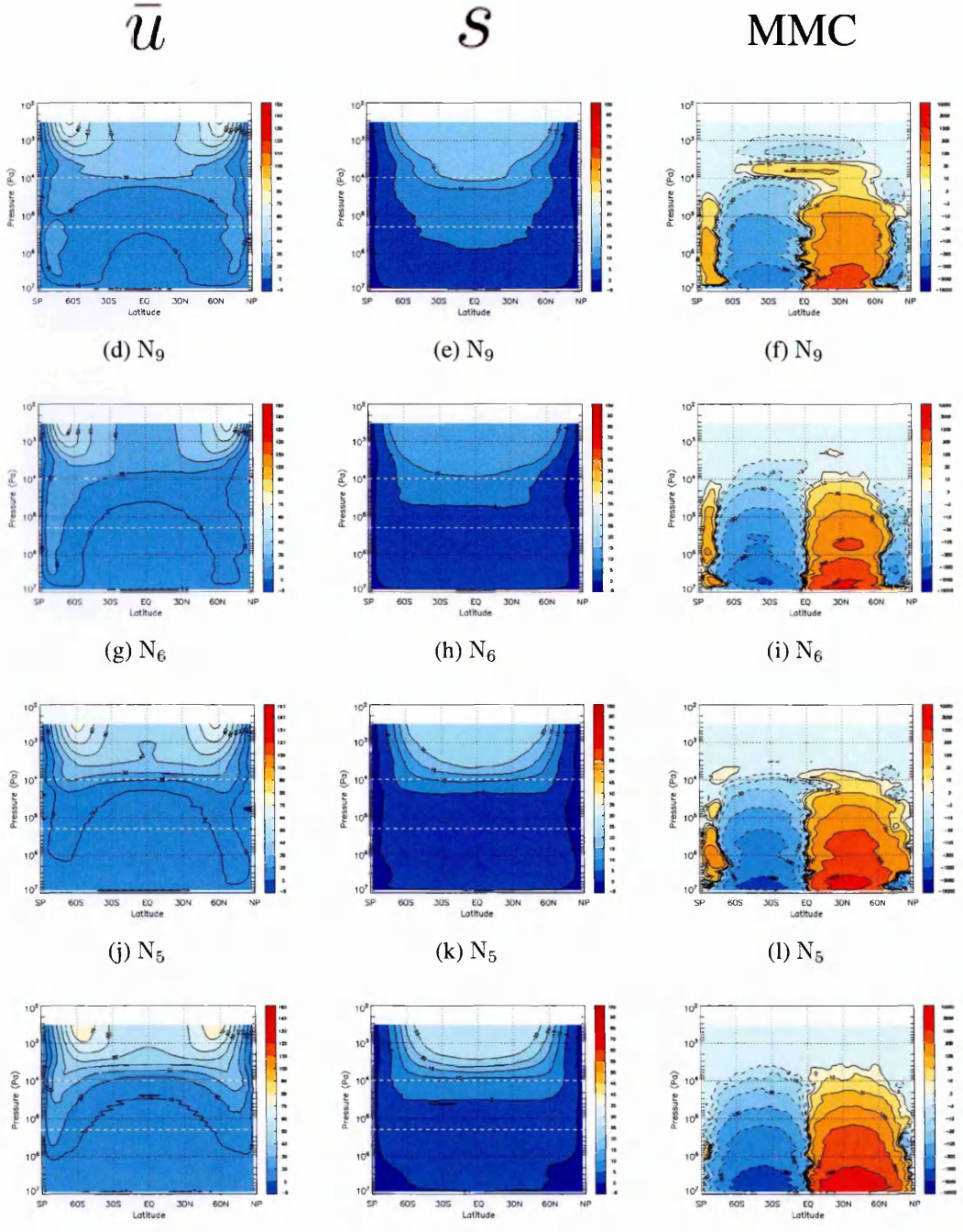

(d) N_9 (e) N_9 (f) N_9

(g) N_6 (h) N_6 (i) N_6

(j) N_5 (k) N_5 (l) N_5

(m) N_4 (n) N_4 (o) N_4

Figure 6.7: Zonal wind, super-rotation and meridional circulation for T42 with MBS forcing, averaged over four Vdays, dashed lines indicate cloud levels.

Table 6.3: Peak wind speed, local super-rotation index and peak meridional circulation for T42 horizontal resolution with MBS forcing

Profile label	**Peak wind ($m\,s^{-1}$)**	**Max. s**	**Peak MMC**
N_9	71.5	20	651
N_6	67.4	15	1380
N_5	73.5	23	1466
N_4	79.8	28	2579

6.3 Summary of modified background stability experiments

In this section the results for simulations performed with an increase in the temperature, and stability, of the thermal forcing profiles were presented. The stability was increased by using a relaxation temperature with a higher temperature in the upper atmosphere than N_4. The N_4 thermal forcing uses a reference vertical temperature profile based on observations by spacecraft and entry probes. The lapse rate for the forcing was increased by using a reference profile modified with higher temperatures as altitude is increased in the atmosphere. The profiles with a 'modified background stability' (MBS) are known as N_5, N_6, and N_9 in order of increasing temperature.

At T21 resolution it was seen that increasing the reference vertical temperature profile and stability used for the forcing results in a higher wind speed in the atmosphere. The wind speed is proportional to the temperature increase thus allowing a calculation of the temperature required for a given wind speed to be made. The most realistic wind speeds for Venus ($\sim 90\ m\,s^{-1}$) from the simulations performed were obtained with the N_5 forcing profile. The effect of increased atmospheric temperature on the wind speed and super-rotation generated in a GCM was noted by Yamamoto and Takahashi (2003a,b) in their simulations.

The increasing wind speed, increasing s and increasing S generated with increasing stability forcing is accompanied by decrease in MMC. The reduced MMC results in a reduction of the mean transport of angular momentum away from the equator in the upper levels of the atmosphere thus allowing more angular momentum to build up at the equator. The Gierasch mechanism can be used to explain how the transport of angular momentum towards the equator is opposed by transport of angular momentum by the MMC in the poleward direction.

The temperature anomaly shows a colder polar area in the lower atmosphere, at cloud heights, as the forcing stability increases. Similarly equatorially within the cloud layers a warm area appears and increases in its temperature as the forcing stability is increased. A warm pole was seen at the top of the atmosphere which rises to a peak with N_6 forcing and then reduces as the forcing stability is increased further.

Increasing the stability of the forcing generates higher zonal winds, increased super-rotation and increased temperature contrasts which can closely match observations of Venus' atmosphere. For the cases tested the most 'realistic' results were obtained with a forcing stability profile of N_5. It is reasonable to expect that a profile with a temperature increase set to a few degrees above N_5 would result in wind speeds and a corresponding super-rotation which would precisely match those observed.

It would be interesting to further test the effect of the temperature profile used for the forcing to see if similar results are obtained with profiles where the temperature increase is applied with a different vertical profile, such as increasing the temperature in either only the lower or upper atmosphere, possibly following the Magellan empirical values more closely.

A summary of the results for the T21 modified background stabilty simulations is shown in table 6.4.

Table 6.4: Summary of T21 simulation results at 500 Vdays

Profile label	**Temp** (K) **increase**	**Max. wind** ($\mathrm{m\,s^{-1}}$)	**Max.** S	**Max.** Δ**T** (K)	**Min.** Δ**T** (K)	**Max. MMC** ($\times 10^9$ kg $\mathrm{s^{-1}}$)
N_4	0	50	4.36	1.4	-10.8	710
N_5	21	93	6.11	10.6	-21	1106
N_6	42	142	9.07	17.2	-30	1291
N_9	84	150	10.46	14	-30.6	1865

Experiments were also performed at T42 horizontal resolution using all four forcing states tested in section 6.1 at T21 horizontal resolution. In these experiments the global atmospheric angular momentum (S) that developed reached equilibrium for all four forcing states tested, with higher stability forcing taking longer to reach equilibrium and reaching a higher value of S.

Despite the result obtained for S the results for zonal wind and local super-rotation index were relatively close for all four forcing states tested. The winds showed peak speeds in two jets at the top of the atmosphere modelled. The peak wind speed ranged from 79.8 $\mathrm{m\,s^{-1}}$ to 67.4 $\mathrm{m\,s^{-1}}$, with the maximum for N_4 forcing and the minimum for N_6 forcing.

The wind in the lower atmosphere, below the clouds, increased by a few $\mathrm{m\,s^{-1}}$ as the forcing stability increased. This is where the atmosphere is most dense and has the most mass thus accounting for the increase in S as the forcing stability increased.

Results for MMC were also presented. These results showed a single Hadley cell in each hemisphere with the strength of the circulation highest for N_4 forcing and decreasing as the forcing temperature profile was increased. This can be explained by the Gierash mechanism with the reduction in poleward transport of angular momentum by the Hadley cell leading to higher super-rotation.

6.4 Diurnal cycle

A simple diurnal cycle was added to the VSGCM, by first making a four dimensional (λ, ϕ, p, t) temperature restoration state to relax towards. In a 2D (ϕ, p) restore file used without a diurnal cycle the temperature state is saved once. For this four dimensional restoration state the temperature data is saved for each longitude, 64 values for a T21 resolution file.

The 4D restore state has basic temperature values similar to the two dimensional restore state used for the N_4 simulations. To simulate the change in insolation as Venus rotates around the Sun the longitude is incremented as the day progresses. An increase in temperature is applied as the longitude is incremented giving a progressively higher temperature from the local sunrise at 0° , to reach a peak value at local midday at 90° . The temperature then falls progressively for the next longitudes reaching the basic temperature again at 180° , the local sunset. The following 180° have the basic temperature applied for the local night-time. The value of the basic temperature is reduced by a factor of $1/\pi$ from the N_4 temperature to ensure that the mean temperature across all longitudes is the same as that for a two dimensional N_4 restore state without a simulated diurnal temperature variation. A Gaussian latitude factor is applied to the temperature increase, to smoothly reduce the equatorial maximum to the base value at the poles.

The diurnal restoration temperature data for the lowest vertical level is shown in figure 6.8, a similar profile is applied to the higher vertical levels with lower temperatures. The 'bump' of the simulated sub-solar point is centred latitudinally on the equator, which is ideal for Venus as the planet has an axial tilt of 177°, no significant seasons and the sub-solar point is always close to equatorial at any time during Venus' orbit of the Sun. When used with the diurnal cycle the restore state propagates around the planet following the sub-solar point.

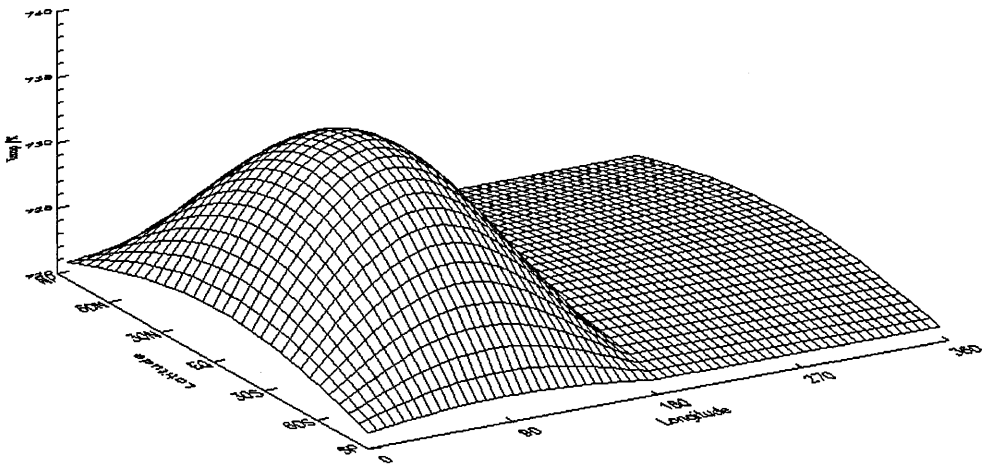

Figure 6.8: Temperature for the restore state for lowest model level

The VSGCM code was modified to use the four dimensional restoration state file by incrementing the longitude selected, and therefore the temperature profile used, as the solar day of the run progressed. A solar day on Venus is 116.75 Earth days in duration, 0.48 Venus sidereal days, 11520 model time-steps with the settings described in section 4.5. The longitude was required to increment though 64 longitudes during the solar day, so the increment interval would be every 180 time-steps. If different settings were to be used, such as a different number of time-steps per day or a higher resolution with more longitudes, the number of time-steps per increment can be calculated from: ((TSPD*(116.75/243))/no. of longitudes).

The VSGCM was tested using this simple diurnal cycle with a maximum temperature increase of 100K over the mean value. This is a larger day-night temperature difference than observed for Venus where many instruments have found the day-night variation to be <10K.

For this simulation the sponge layer was set to eddies only, all other settings were as described in section 4.5. The model was run a 250 Vdays (60,750 Earth days) simulation.

6.4.1 Atmospheric Angular Momentum

The global atmospheric angular momentum (S) developed in this experiment is shown by the black line in figure 6.9. The angular momentum is continuing to grow at the end of the simulation and has not yet reached an equilibrium state. The magnitude of S developed is very similar to that found when using the N_9 forcing state, which is also shown on figure 6.9 as a dashed red line. The development of S for this diurnal cycle experiment is very closely mirrored by the N_9 forcing experiment for the first 110 Vdays when the diurnal cycle experiment shows a small increase in S to the end of the simulation.

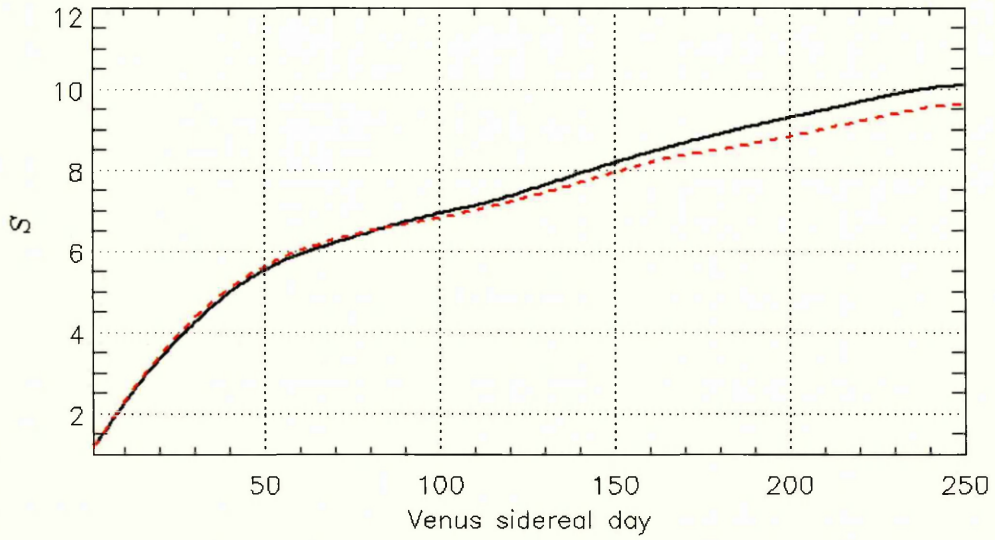

Figure 6.9: S for diurnal cycle with max. T = 100K

6.4.2 Zonal wind

The zonal wind is shown in figure 6.10. The peak wind speed was 149 $\mathrm{m\,s^{-1}}$ at the cloud tops, in two jets at mid latitudes ($\pm 45°$). The wind speed reduces progressively as the altitude reduces, reaching zero at the surface. The wind at all altitudes reduces to below 20 $\mathrm{m\,s^{-1}}$ as the poles are approached.

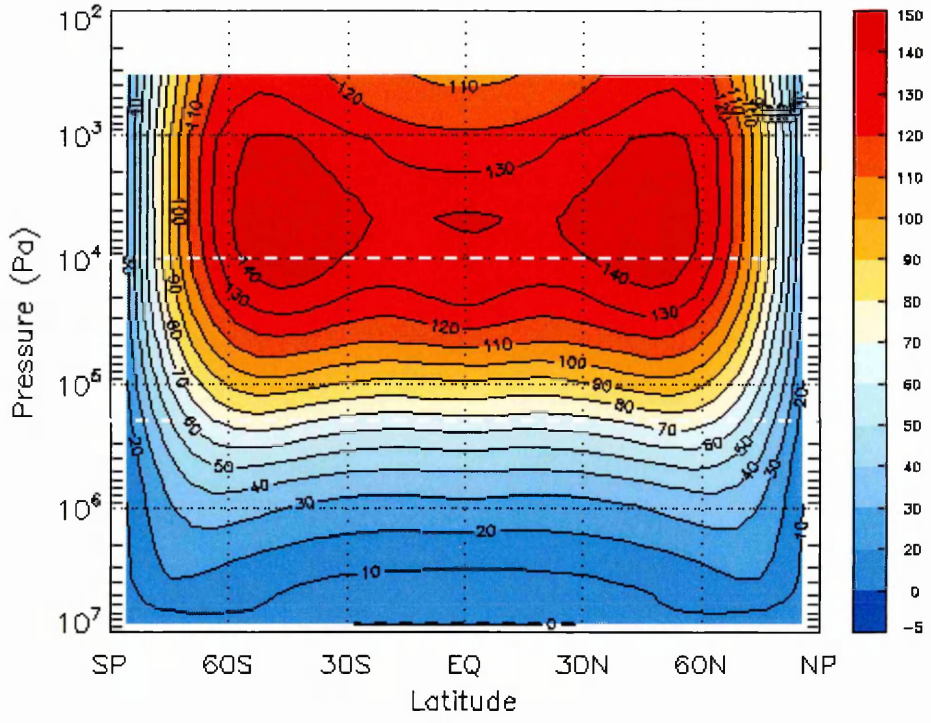

Figure 6.10: Zonal wind for diurnal cycle with max. T = 100K, dashed lines indicate cloud levels

The zonal wind developed by this simulation is very similar to the result found using $\mathrm{N_9}$ forcing with a 2D restore state as shown in figure 6.4c. To highlight the similarities a plot was made of difference between this simulation and $\mathrm{N_9}$ forcing at 250 Vdays. Shown in figure 6.11 it can be seen the winds are slightly greater (up to 6.3 $\mathrm{m\,s^{-1}}$) within the clouds, close to the equator; up to 12.7 $\mathrm{m\,s^{-1}}$ less at the top of the atmosphere in the diurnal cycle simulation; everywhere below the cloud tops the zonal wind is within 10 $\mathrm{m\,s^{-1}}$ of the $\mathrm{N_9}$ experiment.

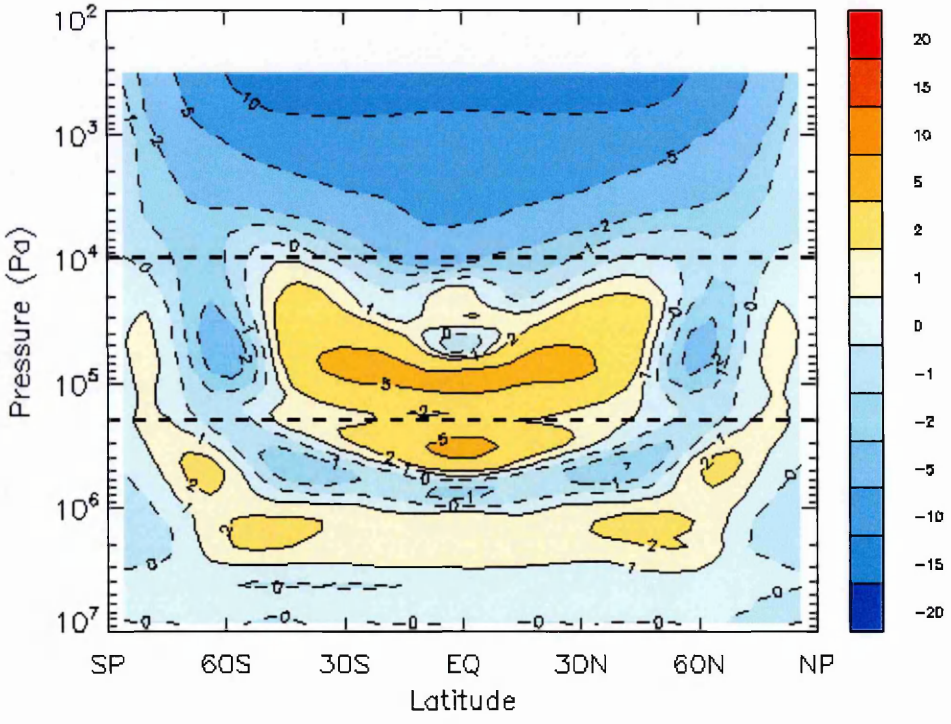

Figure 6.11: Zonal wind difference from N_9 forcing using diurnal cycle at 250 Vdays, dashed lines indicate cloud levels

6.4.3 Local super-rotation index

The local super-rotation index (s) is shown in figure 6.12. The peak in s is at the cloud top and the equator. The peak magnitude of s is 78, reducing monotonically to zero at the surface and the poles. This result is also very similar to that found with N_9 forcing shown in figure 6.4d.

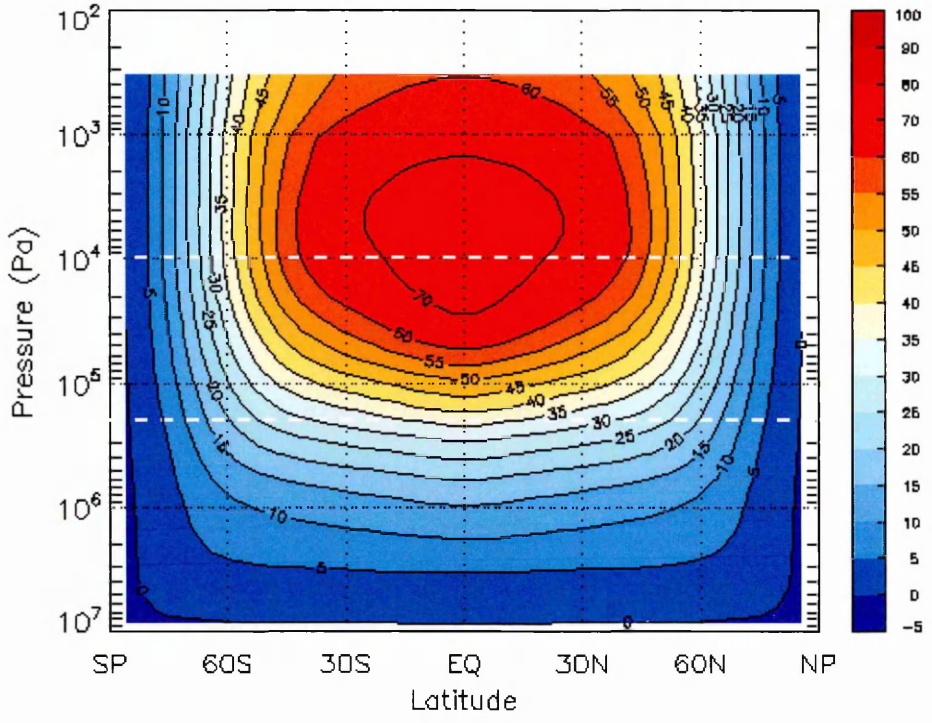

Figure 6.12: Super-rotation index for diurnal cycle with max. T = 100K, dashed lines indicate cloud levels

6.4.4 Mean Meridional Circulation

The meridional circulation is shown in figure 6.13. The meridional circulation shows a dominant Hadley cell in each hemisphere, with a second cell close to the pole circulating in the opposite direction. Similar meridional circulation was seen when testing the model with enhanced temperature used for the forcing. See the plot for the N_9 forcing state in figure 6.5c.

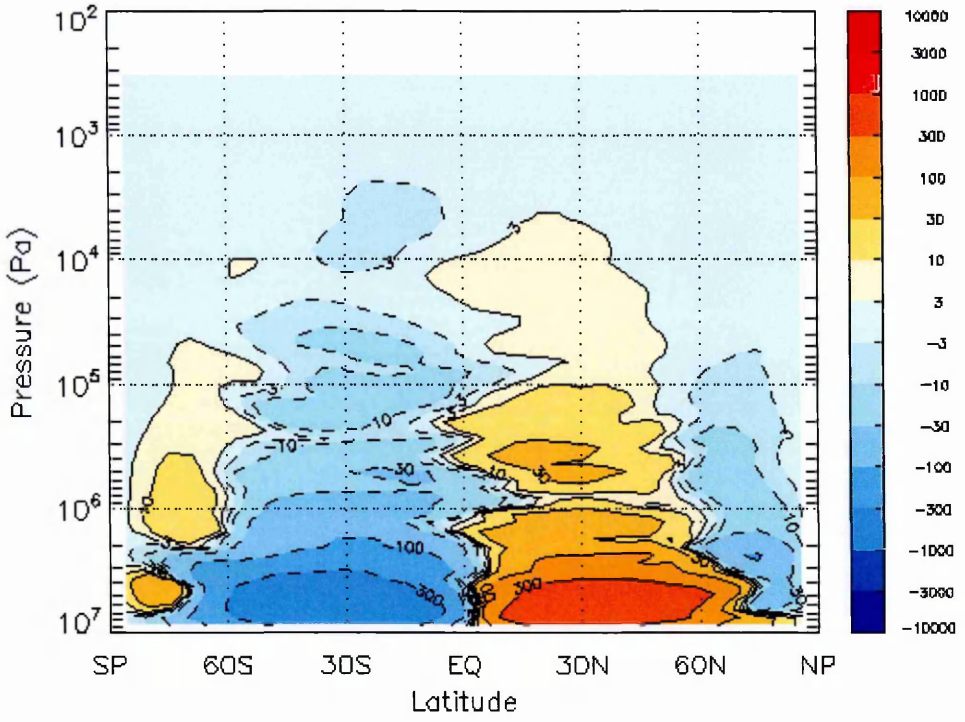

Figure 6.13: Mean Meridional Circulation with diurnal cycle, max. T = 100K

6.4.5 Temperature anomaly

The temperature anomaly (ΔT), defined in equation 5.1, is shown in figure 6.14. The ΔT shows warm poles in the upper atmosphere and cold poles at the cloud levels. This result is, like that for zonal wind, local super-rotation index and meridional circulation, similar to that achieved for the N_9 forcing shown in figure 6.5d.

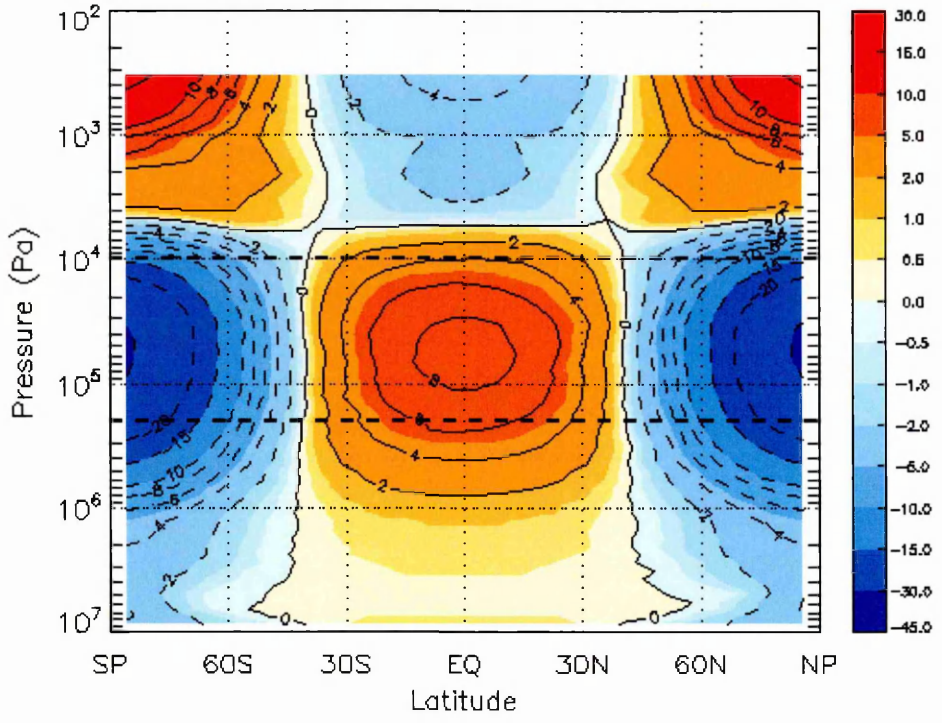

Figure 6.14: Temperature anomaly using diurnal cycle, max. T = 100K, dashed lines indicate cloud levels

6.5 Summary of diurnal cycle experiments

In this section the simple diurnal cycle was described. A description was given of how the diurnal cycle was implemented with a 4D restore state. This restore state was tested for a simulation of 250 Vdays with a maximum increase in local midday temperature of 100K. It was noted that this is much more than the observed day-night temperature variation on Venus.

Results were presented for global atmospheric angular momentum, zonal wind, local super-rotation index, meridional circulation and temperature anomaly. The results showed strong angular momentum and zonal wind results, as was seen in the experiments when using the 2D N_9 forcing profile and shown in chapter 6.

The similarity between the diurnal cycle results and those found when using enhanced temperature with a 2D restore state indicate that it is only necessary to increase the forcing temperature for a limited time during the simulation in order to achieve a 'realistic' result. It is likely that the temperature increase can be tuned in order to achieve results which match observations of the Venus atmosphere.

It was shown earlier in the chapter how the static stability increased when an enhanced temperature profile was used to generate the forcing state. With this simple diurnal cycle the temperature, and therefore stability, is progressively increased to simulate the change in insolation during a 'day'. The maximum temperature increase used here is similar to that for the N_9 forcing state suggesting that increasing the stability in 'pulses' is equivalent to a continuous increase from a 2D restoration state without a diurnal cycle.

The following chapter details experiments with different resolutions. The results for runs with a different number of vertical levels, using two forcing states are presented. The chapter also includes a number of simulation with different horizontal resolutions, again each resolution with two forcing states.

Chapter 7

Resolution

The response of the VSGCM to the resolution used was tested with a number of simulations. In the first section of this chapter the vertical resolution is tested. Following these tests the horizontal resolution is varied and the effect on the model output presented.

7.1 Vertical resolution

The effect on the model output of changing the vertical resolution was investigated by performing experiments using the N_4 and N_9 forcing states with 32, 50, 100 and 200 vertical levels each. For these experiments the sigma levels required were generated by interpolation of the original L50 sigma levels (shown in figure 4.3) with the highest and lowest levels remaining at the same values in order that the height of the modelled atmosphere and the thickness of the boundary layer remained the same for all experiments. The interpolated levels are evenly spaced between the original L50 levels thus retaining the same profile as shown in figure 4.3.

7.1.1 Vertical resolution with N_9 forcing

The vertical resolution was first investigated using N_9 forcing. Results will be presented for S, $\bar{u}$, *and* s.

7.1.2 Atmospheric Angular Momentum

The time evolution of S is shown in figure 7.1. From this graph it can be seen that S for L200 and L100 is no longer increasing with time after 250 Vdays. For the L50 and L32 experiments S continues to increase at the end of the 250 Vdays simulation time.

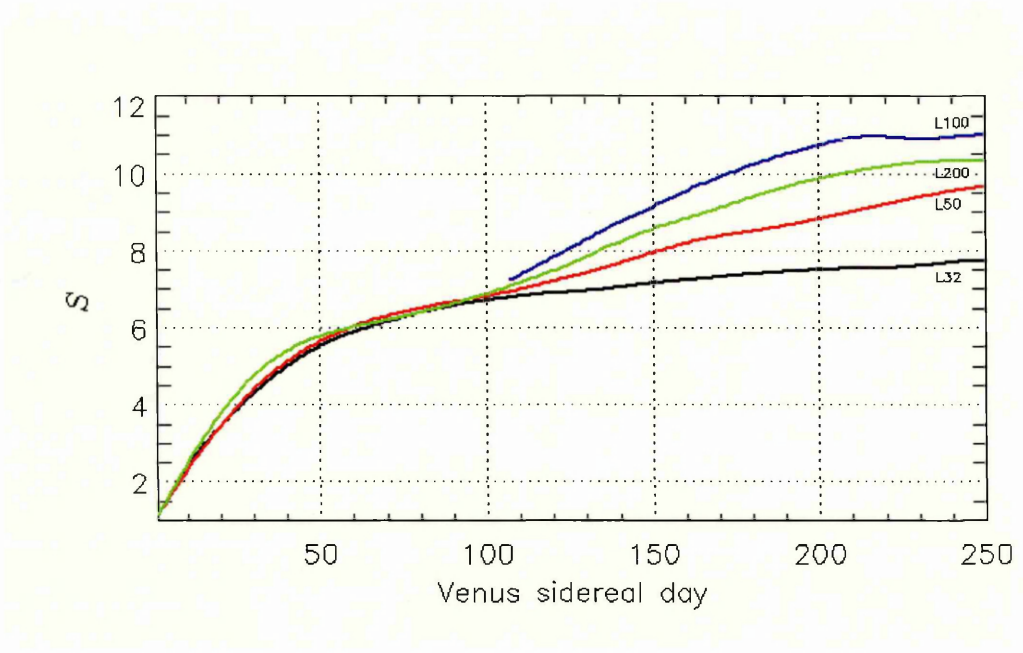

Figure 7.1: Time development of S for NL experiments with N_9 forcing.
Blue line, L200; green, L100; red, L50; black, L32.

The magnitude of S at the end of the 250 Vday simulation time increases as the number of vertical levels is increased. For all the vertical level experiments S initially develops in an almost identical manner for the first 100 Vdays then the values of S diverge with a greater rate of increase for a greater number of vertical levels.

It was shown in chapter 6 that N_9 forcing with L50 (the red line in figure 6.3, also the red line in figure 7.1) reached a stable value of 10.46 in $\sim$400 Vdays, approximately the equilibrium value reached for L100 and L200. This suggests that if the L32 simulation was run for a longer time it would also reach an equilibrium with $S \simeq 10.5$. The final values of S at the end of the 250 Vday simulation are summarised in table 7.1.

7.1.3 Zonal wind

The zonal wind, shown in figure 7.2, increases in magnitude as the number of vertical levels used is increased. L32 developed a maximum of 115.7 $\mathrm{m\,s^{-1}}$ slightly more than is observed on Venus, however the atmospheric angular momentum was still increasing so the winds would be expected to strengthen were the simulation to run for longer. The L50 experiment reached a peak of 150.8 $\mathrm{m\,s^{-1}}$ but as was shown for L32, the magnitude of S was still increasing. Figure 6.3 showed S for L50 had reached equilibrium during a 500 Vdays simulation and increased in magnitude by only 0.84. The peak zonal wind (figure 6.4c) was almost unchanged at 150.0 $\mathrm{m\,s^{-1}}$.
L100 achieved a peak wind speed of 152.3 $\mathrm{m\,s^{-1}}$ and L200 a little higher at 162.0 $\mathrm{m\,s^{-1}}$.

For all the experiments the peak in wind speed was at $\sim$ 1400 Pa, just above the cloud layers. The peak winds developed in two jets, one in each hemisphere, at around $\pm 50°$ latitude. The general form of the winds below the cloud layers was similar for all simulations with L50 or more vertical levels, however for L32 the winds below the clouds were reduced compared to the other simulations.

7.1.4 Local super-rotation index

The local super-rotation index plots, also shown in figure 7.2 with the zonal wind plots, show a peak in s just above the clouds and centred on the equator in all cases. The local super-rotation index at 250 Vdays increases in magnitude as the number of vertical levels is increased.

The values of global atmospheric angular momentum (S), peak zonal wind ($\bar{u}$) and local super-rotation index (s) at the end of the 250 Vday simulation are summarised in table 7.1.

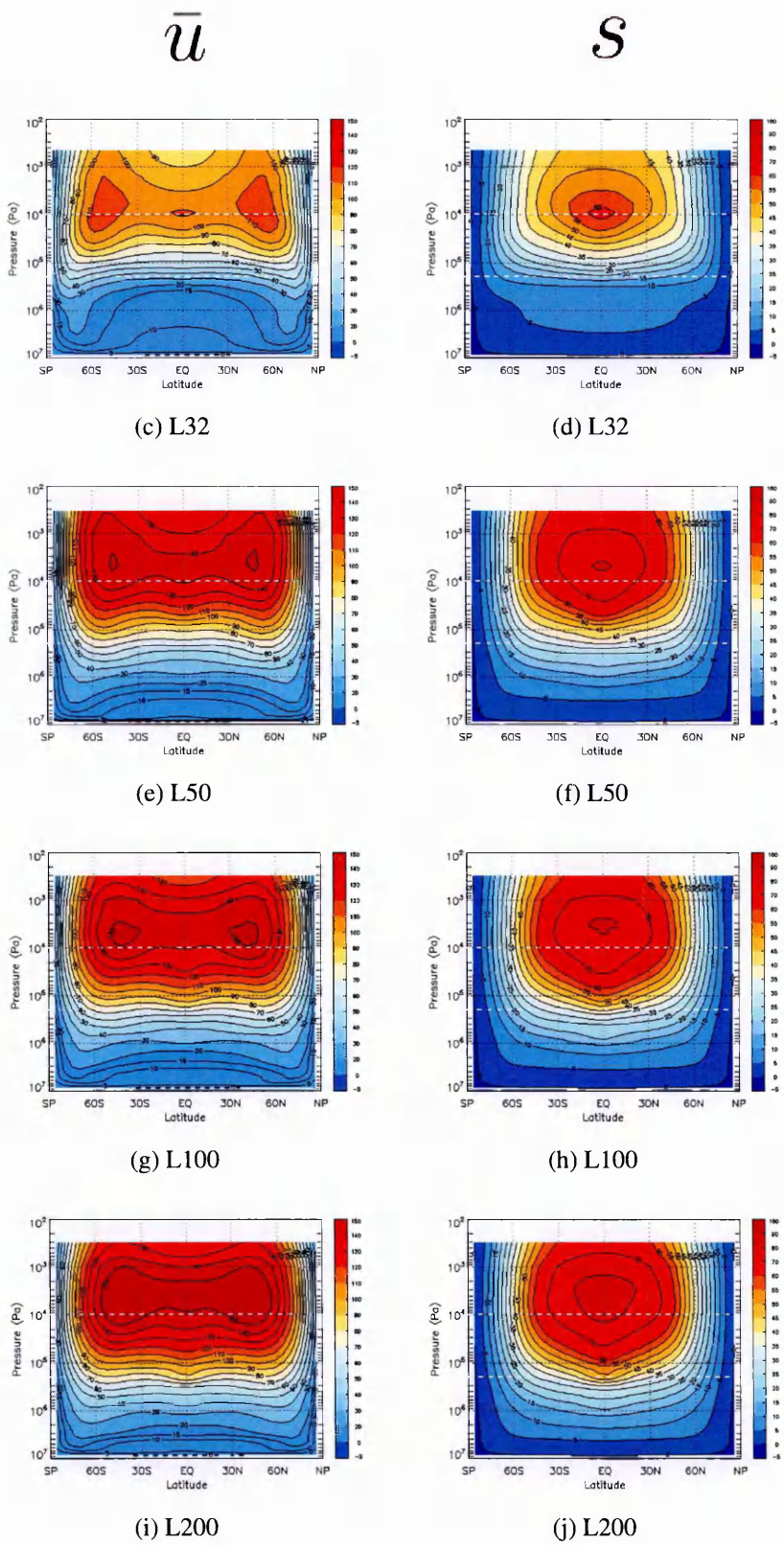

(c) L32 (d) L32

(e) L50 (f) L50

(g) L100 (h) L100

(i) L200 (j) L200

Figure 7.2: $\bar{u}$ and s for vertical level experiments with N_9 forcing, averaged over final four Vdays of simulation, dashed lines indicate cloud levels.

7.1.5 Vertical resolution with N_4 forcing

The vertical resolution was investigated using N_4 forcing. Results will be presented for S, $\bar{u}$, *and* s.

7.1.6 Atmospheric Angular Momentum

The time evolution of S for the vertical level experiments using the N_4 forcing state is shown in figure 7.3. This graph shows that for all the vertical levels tested equilibrium has been reached. Overall the magnitude of S is lower than seen with N_9 forcing and unlike that found with N_9 forcing the correlation between increased S (at 250 Vdays) and the number of vertical levels is not seen. With L100 having the largest value of $S = 4.78$, L200 similar but slightly less $S = 4.51$ and L50 a little less again $S = 4.27$. L32 is much lower ($\sim$ half, $S = 2.54$) than that found with more vertical levels. L100 and L200 show a small amplitude oscillation around their mean values. The mean values of S for the final 10 Vdays of the simulations are summarised in table 7.2.

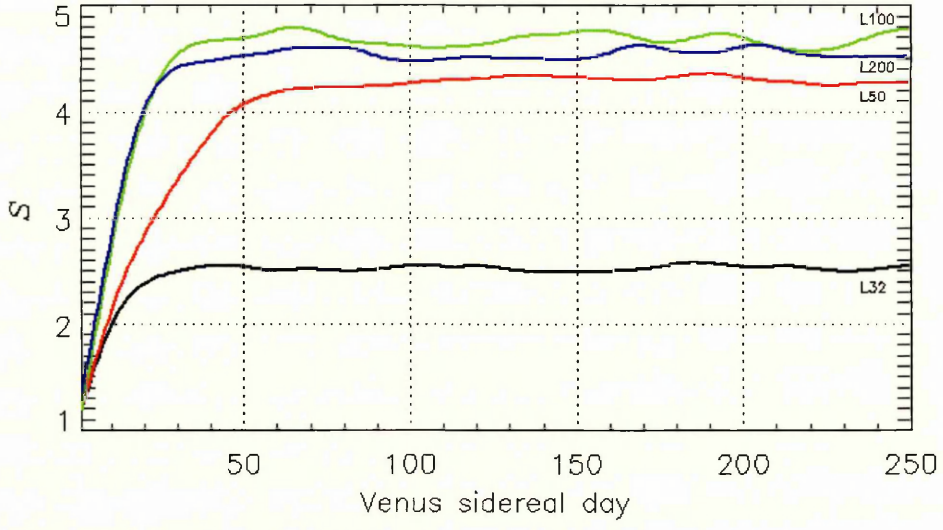

Figure 7.3: Time development of S for NL experiments with N_4 forcing.
Blue line, L200; green, L100; red, L50; black, L32.

7.1.7 Zonal wind

The wind results for the experiments using N_4 forcing again differ from N_9 forcing with the highest wind speeds generated for the L32 simulation. Lower maximum wind speeds, although similar to L32, are seen for a greater number of vertical levels, with a minimum for the L100 simulation. In all cases the wind field is broadly similar with two jets in the upper atmosphere at approximately $\pm 75°$, a higher latitude than the approximately $\pm 50°$ seen when using the N_9 forcing profile. The jets weaken in peak wind speed as the number of vertical levels increases up to L100 from 61.7 to 51.0 $\mathrm{m\,s^{-1}}$, and then strengthen slightly for L200 to 52.2 $\mathrm{m\,s^{-1}}$.

In the lower atmosphere wind speeds of $\leq 20\ \mathrm{m\,s^{-1}}$ are seen except for L200 which has two 'jets' of $20 - 30\ \mathrm{m\,s^{-1}}$ at latitudes of $\sim \pm 70°$. The middle atmosphere winds, around the cloud layers, decrease as NL increases from L32 to L100 and then increase slightly for L200.

7.1.8 Local super-rotation index

The local super-rotation index (s) for the N_4 forcing state experiments are shown in figure 7.4. Overall s is weak and has a peak value centred on the equator within the cloud layers and above. The peak values show a decrease in s from L32 ($s = 11.8$) to L100 ($s = 8.0$), and then an increase for L200 ($s = 9.0$).

The peak wind speed and maximum value of s for the vertical level simulations with N_4 forcing are shown in table 7.2.

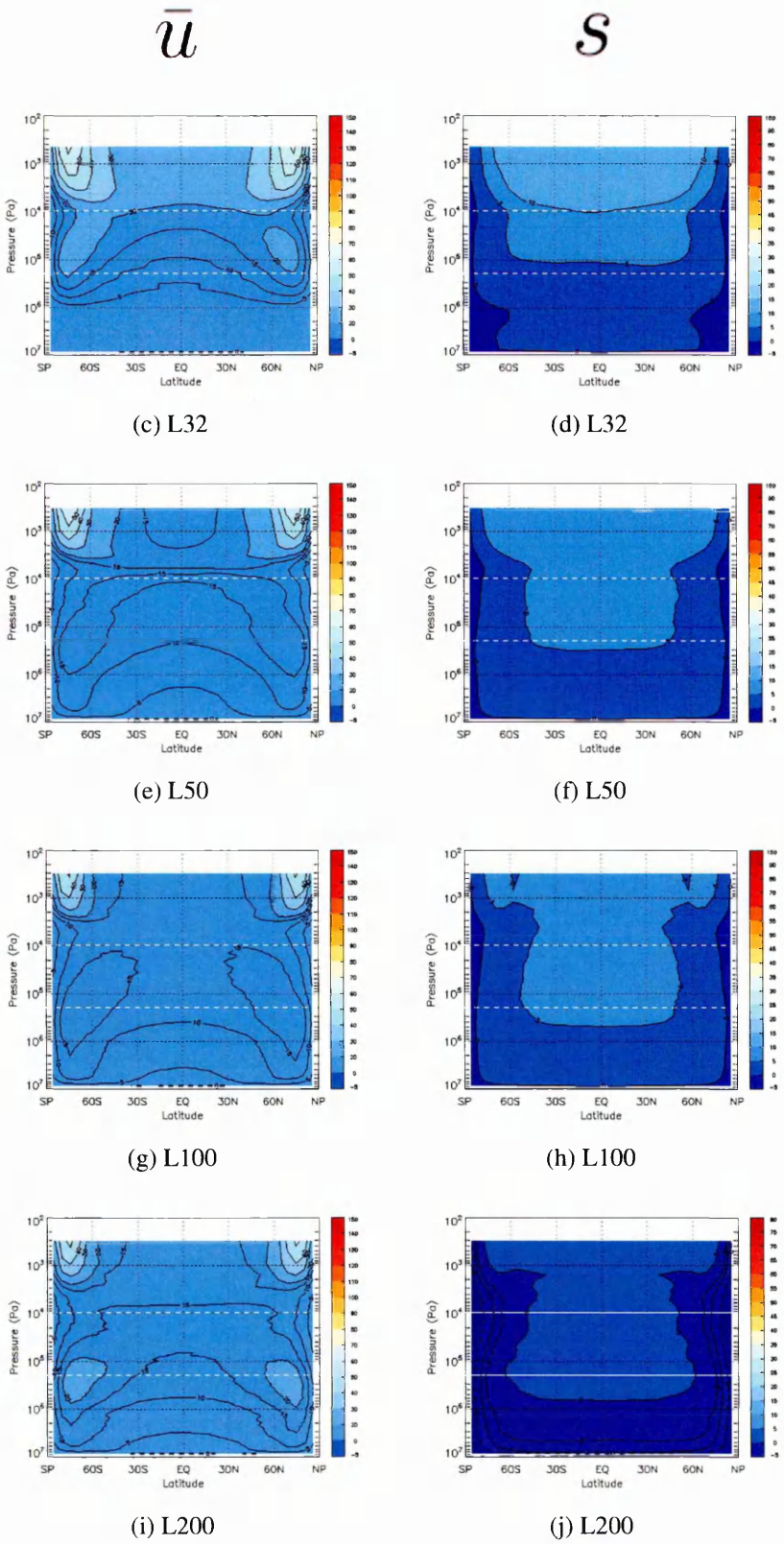

(c) L32 (d) L32

(e) L50 (f) L50

(g) L100 (h) L100

(i) L200 (j) L200

Figure 7.4: $\bar{u}$ and s for vertical level experiments with N_4 forcing, averaged over the final four Vdays of simulation, dashed lines indicate cloud levels.

7.2 Summary of vertical resolution experiments

In this chapter results were presented for simulations to test the VSGCM's response to different vertical resolutions. Tests were performed with N_9 and N_4 forcing, for each forcing state the number of vertical levels (NL) was set for 32, 50, 100 and 200. Results for S, zonal wind and s were shown for these experiments.

Experiments with the N_9 forcing state showed the time evolution of S indicating that L100 and L200 had reached equilibrium within the 250 Vday simulation time. L50 was still increasing, however it was seen in section 6.1 that equilibrium was achieved for this simulation in ~ 400 Vdays at a similar magnitude to the L100 and L200 experiments. L32 was increasing slowly at 250 Vdays, the possibility was suggested that if this simulation was run for a longer time it would and reach equilibrium with a similar value to the simulations with 50 or more vertical levels.

The computer time required for the simulations scales with the number of levels, with a simulation with double the number of levels taking twice as long for the simulation to run. So L50 reaching equilibrium at 400 Vdays would be equivalent to L100 in 200 Vdays, L200 in 100 Vdays and L32 in 625 Vdays; hence L50 is the most efficient in terms of computer time for the experiments performed with N_9 forcing used.

The zonal wind results with N_9 forcing showed L200, L100 and L50 to have developed similar wind profiles with the peak wind speed developing in two jets, one in each hemisphere, at $\sim \pm 50°$ latitude, just above the cloud tops. The peak wind speeds were within a 12 $\mathrm{m\,s^{-1}}$ band centred on 156 $\mathrm{m\,s^{-1}}$. The local super-rotation index was also similar with L200, L100 and L50 within $s = 9$ with a median value of $s = 81.75$. L32 had lower wind speeds with a peak of 115.7 $\mathrm{m\,s^{-1}}$ and peak s of 61.4. Results which

are close to the observed values for Venus. The results fo S, peak $\bar{u}$ and maximum s are summarised in table 7.1.

Table 7.1: S, peak wind and s values at 250 Vdays for NL simulations N_9 forcing

Levels (NL)	**Mean S**	**Peak wind speed** $(\mathrm{m\,s^{-1}})$	**Peak s**
32	7.74	115.7	61.4
50	9.62	150.8	77.5
100	10.33	152.3	81.9
200	10.70	162.0	86.0

The situation with N_4 forcing was very different. All the experiments had reached equilibrium by 100 Vdays although at different final values and at a much lower magnitude than with the N_9 forcing state. A large increase was seen between L32 and L50 with L50, L100 and L200 separated by less difference. The similarity for levels L50 and above would again suggest L50 to be the best to use in terms of required computer time.

For N_4 forcing all the experiments developed their peak zonal wind in two jets high in the atmosphere (with the centre of the jet above 6×10^3 Pa). The jets were at a higher latitude ($\pm 75°$) than the N_9 forcing experiments. The peak wind speeds ranged from 61.7 to 51.0 $\mathrm{m\,s^{-1}}$ with the maximum for L32 and the minimum for L100. Local super-rotation index showed a similar trend with a maximum for L32 and the minimum for L100.

The results for the vertical level experiments with N_4 forcing are summarised in table 7.2 where it can be seen that peak $\bar{u}$ and s were inversely correlated to S.

Table 7.2: Mean S, Peak wind and s values for NL simulations with N_4 forcing

Levels (NL)	**Mean S last 10 Vdays**	**Peak wind speed** ($\mathrm{m\,s^{-1}}$)	**Peak s**
32	2.54	61.7	11.8
50	4.27	57.9	9.3
100	4.78	51.0	8.0
200	4.51	52.2	9.0

7.3 Horizontal resolution

Three different horizontal resolutions were tested to investigate the influence of the horizontal resolution on the VSGCM output. Resolutions tested were T10, T21 and T42, where the highest retained wave number was 10, 21 and 42 respectively. All the resolutions were tested with the the N_9 forcing state and the nominal N_4 temperature forcing state. All the experiments comparing horizontal resolutions were performed with 50 vertical levels (NL=50).

The model applies horizontal diffusion/damping with an eighth-order Laplacian (∇^8) diffusion scheme on vorticity, divergence and temperature. The diffusion timescale was set for 0.00204 in all cases, equivalent to 0.5 sidereal days. With this setting the diffusion coefficient used by the model changes with the horizontal resolution selected. The diffusion coefficients for the resolutions tested were:

T10 = $2.9 \times 10^{41}\,\mathrm{m^8 s^{-1}}$

T21 = $9.2 \times 10^{38}\,\mathrm{m^8 s^{-1}}$

T42 = $4.0 \times 10^{36}\,\mathrm{m^8 s^{-1}}$

7.3.1 Horizontal resolution with N_9 forcing

The horizontal resolution was first tested with N_9 forcing. These simulations were run for 500 Vdays.

7.3.2 Atmospheric Angular Momentum

The time development of S is shown in figure 7.5. From these results it can be seen that the T42 simulation has reached a stable equilibrium with $S = 6.4$ in approximately 200 Vdays (the blue line in figure 7.5). The T21 experiment has reached an equilibrium of $S = 10.4$ in $\sim$400 Vdays (the red line in figure 7.5, also shown in the red line in

figure 6.3). The T10 simulation has developed stronger $S = 20.0$ in ~ 380 Vdays (the green line in figure 7.5). The equilibrium values for S are shown in table 7.3 together with the time taken to reach equilibrium.

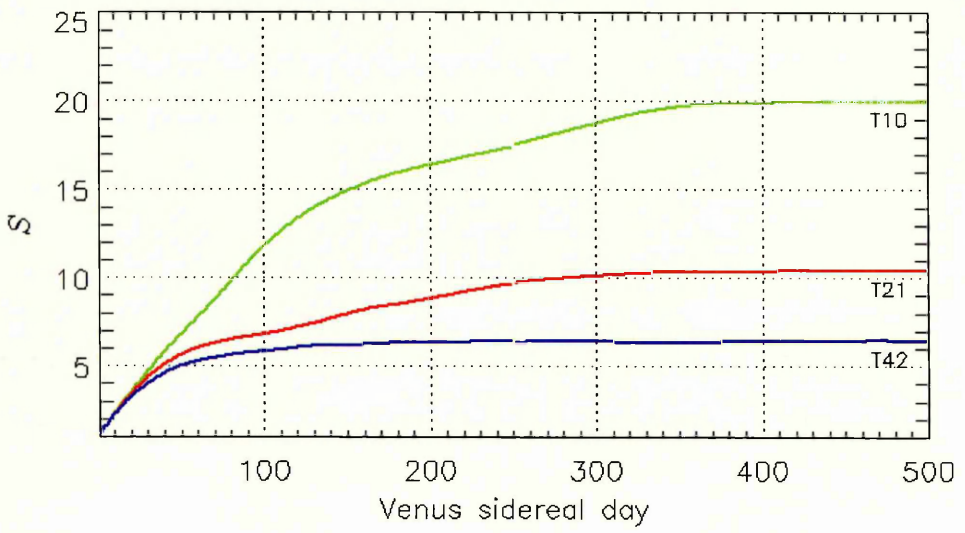

Figure 7.5: Time development of S for horizontal resolutions with N_9 forcing. Green line, T10; red, T21; blue, T42.

Table 7.3: S for horizontal resolutions with N_9 forcing

Resolution	S	**Time to eqbm**
T10	20.0	380
T21	10.4	410
T42	6.4	200

7.3.3 Zonal wind and super-rotation

The winds developed in this experiment are shown in figure 7.6 together with plots for s, the local super-rotation index. The T10 simulation has developed strong winds with a maximum wind speed of over 180 $\mathrm{m\,s^{-1}}$. The wind peaks in two jets at $\sim \pm 45°$ latitude close to the top of the atmosphere modelled. The wind speed above the clouds is over 150 $\mathrm{m\,s^{-1}}$ for the majority of the atmosphere, steadily reducing to 50 $\mathrm{m\,s^{-1}}$ poleward of 60°. Below the cloud tops the wind reduces progressively reaching zero at ground level.

The local super-rotation index for this simulation shows a strong peak in s of > 90 at 2×10^3 Pa above the cloud tops at the equator. The super-rotation steadily reduces to zero away from the peak with areas of $s < 0$ at the poles and below 10^6 Pa.

The plots for zonal wind and local super-rotation index at T21 resolution were shown previously in figures 6.4c and 6.4d. Figure 7.6e shows the zonal wind at 250 Vdays. Like the T10 simulation the winds peak in two jets at $\sim \pm 45°$ but lower in the atmosphere at $\sim 3 \times 10^3$ Pa, just above the top of the cloud layers. The peak wind speed was 151 $\mathrm{m\,s^{-1}}$ with the speed reducing monotonically to zero at the surface. In the lowest levels of the atmosphere, below 10^6 Pa, the zonal wind shows a higher speed at the equator than at $\pm 75°$ whereupon the wind gradient increases as the poles are approached.

In the T21 simulation, s peaks at the equator and $\sim 3 \times 10^3$ Pa, again lower in the atmosphere than found with T10 horizontal resolution. The local super-rotation index, s, steadily reduces to zero away from the peak with areas of $s < 0$ at the poles and below 10^6 Pa.

With T42 resolution the zonal wind developed in the simulation (figure 7.6g) shows two jets at the very top of the atmosphere at $\sim \pm 60°$ latitude. The peak wind speed for this simulation is found in the jets at 72 $\mathrm{m\,s^{-1}}$. The winds in the cloud layers and below are < 30 $\mathrm{m\,s^{-1}}$, less than those developed with T10 or T21 resolution, but as in those simulations reduce to zero at the surface. The winds below the cloud tops are highest at the equator reaching a minimum at $\sim \pm 75°$.

The local super-rotation index for T42 shows little s throughout the atmosphere. The highest s is above the clouds centred on the equator. At the poles, ranging from the surface to the top of the atmosphere, $s < 0$.

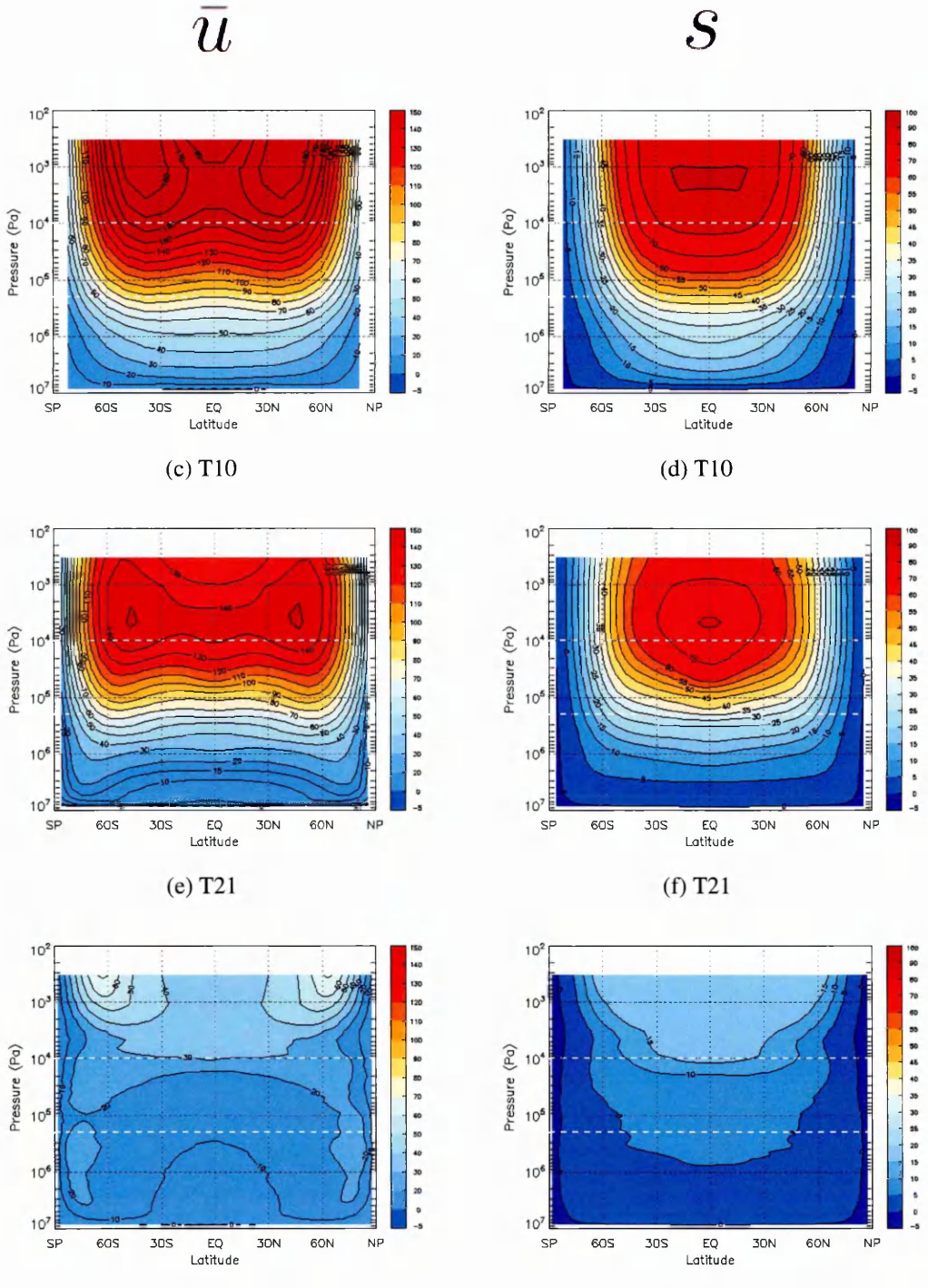

(c) T10 (d) T10

(e) T21 (f) T21

(g) T42 (h) T42

Figure 7.6: $\bar{u}$ and s for horizontal resolutions using N_9 forcing at Vday 250

7.3.4 Horizontal resolution with N_4 forcing

The horizontal resolution for T10, T21 and T42 were also tested with N_4 thermal forcing. These experiments were run for 250 Vday simulation times.

7.3.5 Atmospheric Angular Momentum

To ensure the runs are reaching a statistical equilibrium the time development of S was calculated and plotted for each model run. The time evolution of S for all the horizontal resolutions tested are shown in figure 7.7.

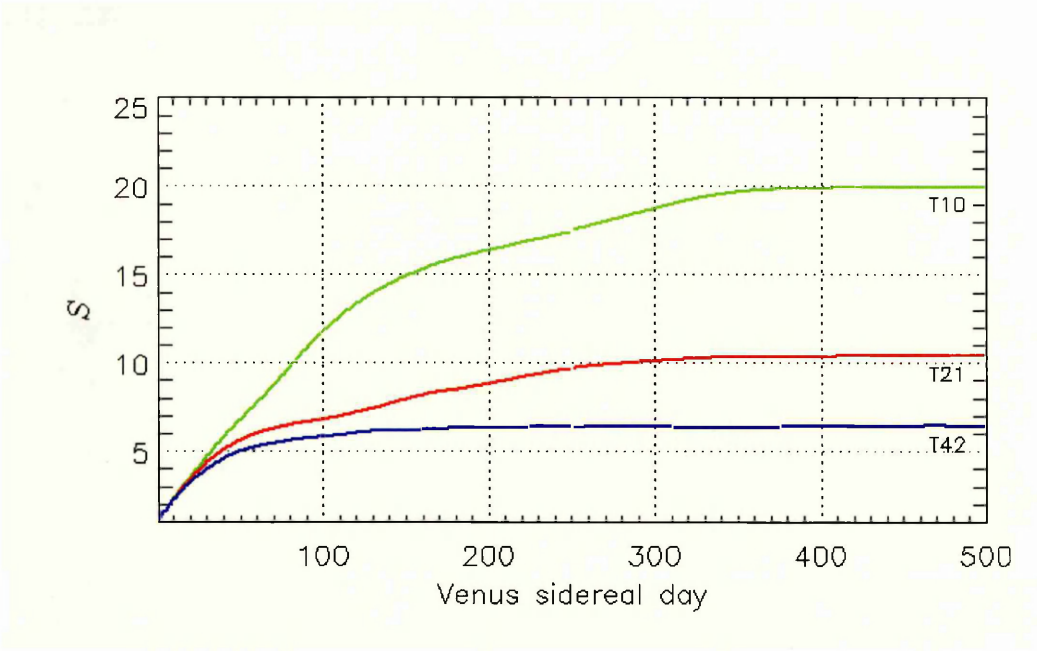

Figure 7.7: Time development of S for horizontal resolutions with N_4 forcing. Green line, T10; red, T21; blue, T42.

For all three of the resolutions tested it can be seen that an equilibrium has been reached and the S value has stabilised. The final value of S and the time taken to reach equilibrium is strongly dependent on the horizontal resolution. Higher resolution simulations reach equilibrium faster and with a lower final S than those simulations with lower resolutions. The approximate times taken to reach equilibrium and the values of S developed are shown in table 7.4.

Table 7.4: S and equilibrium time for horizontal resolutions with N_4 forcing

Resolution	**Approx. Time to eqbm**	**Final S**
T10	230	14
T21	70	4.4
T42	15	2.1

7.3.6 Zonal wind and super-rotation

Results for zonally averaged zonal wind $\bar{u}$ together with plots of the local super-rotation index s for all the horizontal resolutions tested are shown in figure 7.8. The relatively high value for global super-rotation, S, found in the T10 simulation is reflected in the winds and local super-rotation generated with a peak wind speed of over $100\ \mathrm{m\,s^{-1}}$ and peak local super-rotation index, s, of 71.3, both of which are very much higher than the T21 simulation with maximum $s = 9.3$ and the T42 simulation with maximum $s = 28.0$.

The T21 and T42 simulations both show peak wind speeds in two jet like features at the top of the atmosphere, at latitudes of $\pm 75°$ for the T21 experiment and $\pm 45°$ for the T42 experiment. The T21 simulation has a peak zonal wind of $58\ \mathrm{m\,s^{-1}}$ in the jets, reducing to zero at the surface. At lower levels, below the cloud tops, higher winds are seen at high latitudes, above $\pm 60°$.

The T42 simulation has a wind speed $> 40\ \mathrm{m\,s^{-1}}$ between $\pm 75°$ latitude and at $p \leq 5 \times 10^3$ Pa. The peak in the jets is $80\ \mathrm{m\,s^{-1}}$ reducing toward the poles. The wind below the clouds is positive almost everywhere with higher winds at high latitudes, above $\pm 60°$.

Figure 7.8d, for local super-rotation index shows the T10 simulation has produced strong s with a peak of 71.3 centred on the equator and at 3×10^4 Pa, above the cloud tops at 10^4 Pa. Data from entry probes and cloud tracking gives a measured wind speed and the s which is implied is $\simeq 60$ for Venus.

The local super-rotation for T21 is much weaker with peak $s = 9.3$. The plot for s, figure 7.8f, shows some super-rotation above the cloud top and also within the cloud layer between $\pm 45°$. s is dominated by the jet like features at high latitudes in the upper atmosphere producing the strongest s above the clouds.

The T42 simulation shows a defined local super-rotation peak at the equatorial cloud tops. Although the magnitude is lower than that of the observed Venus atmosphere at $\simeq 28.0$. The super-rotation below the cloud top is less well developed than the T10 or T21 cases with a large region of light super-rotation below the cloud tops.

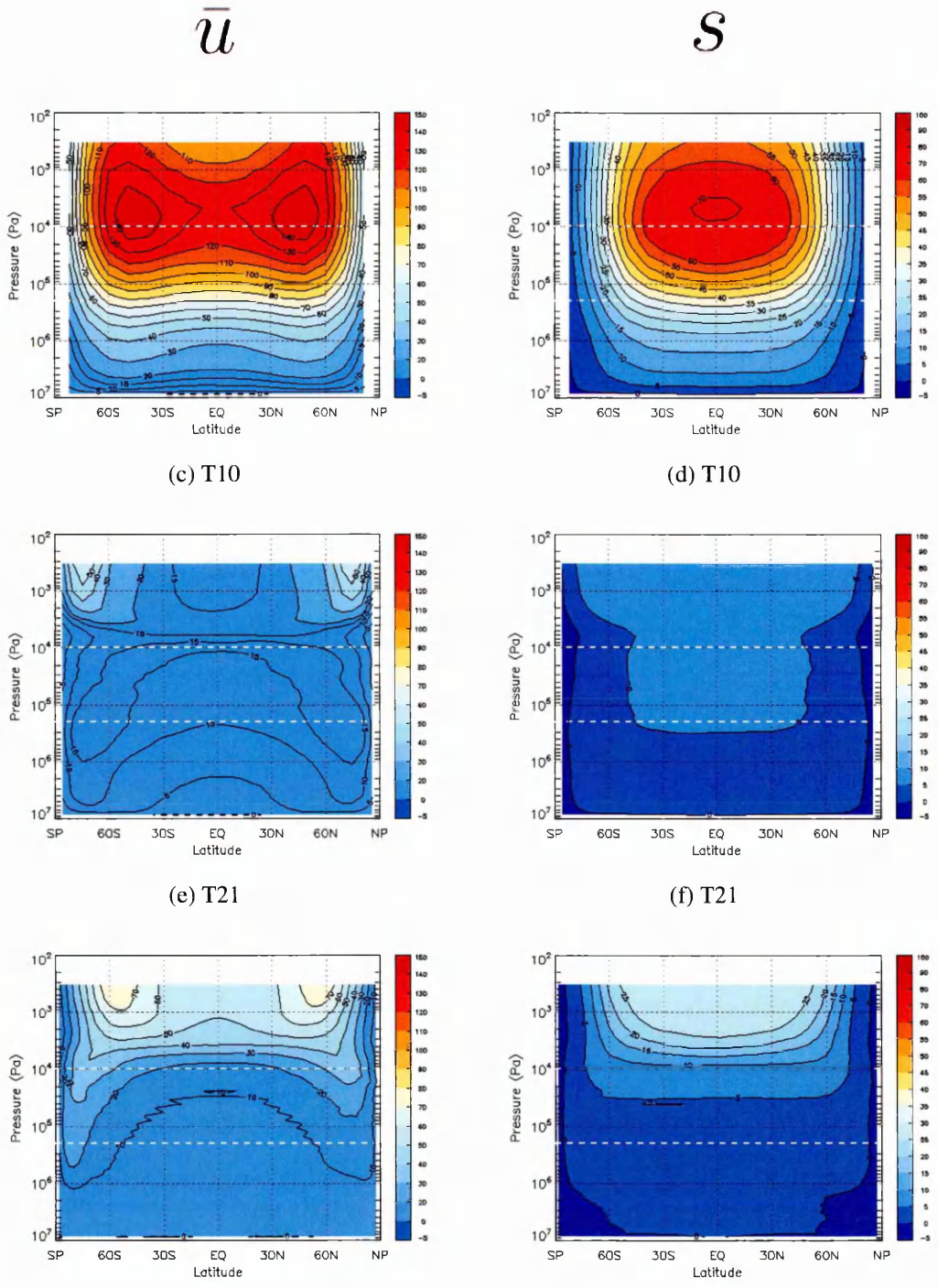

(c) T10 (d) T10

(e) T21 (f) T21

(g) T42 (h) T42

Figure 7.8: $\bar{u}$ and s for horizontal resolutions using N_4 forcing

7.4 Summary of horizontal resolution experiments

In this section the effect on the model output of runs using the same parameterizations, N_9 and N_4 temperature forcing and different horizontal resolutions were tested. The horizontal resolutions tested were T10, T21 and T42.

The simulations using the N_9 forcing temperature profile developed global atmospheric angular momentum which had stabilised at the end of the simulations with $S = 6.4$ for T42 horizontal resolution, $S = 10.4$ for T21 horizontal resolution and $S = 20.0$ for T10 horizontal resolution. Values which were reflected in the zonal wind, $\bar{u}$ and local super-rotation index, s, developed in the simulations. The peak magnitude of $\bar{u}$ and s are summarised in table 7.5.

Table 7.5: Zonal wind and local super-rotation index with N_9 forcing for horizontal resolutions

Resolution	**Max. wind** ($\mathrm{m\,s^{-1}}$)	s
T10	189.8	90.8
T21	150.8	77.5
T42	71.5	19.9

Tests were also performed with N_4 temperature forcing, the results showed S had stabilised for all resolutions within 250 Vdays. The magnitude of S was much greater for the T10 simulation than either T21 or T42. T10 ($S = 14.0$) was over double that of T21 ($S = 4.4$), and four times that of T42 ($S = 2.1$), suggesting that the T10 and T21 runs may have produced unrealistically strong results. This indication was confirmed, in the case of the T10 experiment, when the wind speeds were considered, with a peak zonal wind for T10 of over 140 $\mathrm{m\,s^{-1}}$, whereas the T21 and T42 simulations both produced peak zonal winds of $\simeq 50\ \mathrm{m\,s^{-1}}$, less than the winds observed on Venus, but

with wind profiles which show many similarities between the two simulations.

The super-rotation produced by these simulations showed strong super-rotation for T10, as would be expected from the wind results. The super-rotation for T21 and T42, although much weaker than for T10, showed a peak centred on the equator above the cloud tops. The T42 simulation in particular showed a stronger equatorial peak above the cloud top level. This, and the peak local super-rotation index obtained of 24, showed that the wind and super-rotation index get progressively higher as the resolution is increased beyond T21.

Higher horizontal resolutions lead to reduced global atmospheric super-rotation, suggesting that parameterized, sub-grid scale processes (processes which reduce in significance as the grid size reduces with increased resolution) are responsible for much of the horizontal angular momentum transport.

Chapter 8

Summary and discussion

8.1 Summary

A GCM for modelling the Mars atmosphere, described by Joshi et al. (1995); Lewis et al. (1996) and other papers, based on the terrestrial model originally developed by Hoskins and Simmons (1975), has been converted to Venus parameters and used to develop a simplified GCM for Venus.

This document describes the work done to make the model, known as the Venus simplified GCM (VSGCM) and the results from a number of test runs. This dissertation began with an introduction to Venus and the key parameters for the planet. The atmosphere and atmospheric dynamics were presented in chapter 2. The greenhouse effect effect is significant on Venus with its thick CO_2 atmosphere and high surface temperature of 735K. The physics of the greenhouse effect were discussed. Details of the evolution and super-rotating circulation of the atmosphere were given. Significant features and waves observed in the clouds were presented and discussed before a definition of super-rotation (from Read, 1986a,b; Lewis and Read, 2003) was given with an example calculation based on a simplified wind field.

The next chapter was concerned with many of the previous modelling studies performed for the Venusian atmosphere. The major theories proposed to explain the atmospheric circulation were briefly summarised followed by the modelling studies. For each study details of the model used were given and the results obtained from that model. A brief discussion of some of the 'future' modelling efforts suggested by the authors of the more recent studies ended the chapter.

Chapter four discusses the model used in this study, its history and type. The configuration settings and parameters set for the VSGCM were given. The radiative temperature state used to generate the restoration file (the restore state) for the model was described in detail. The terrain following sigma levels were shown and a discussion of some methods of converting vertical pressure to height. The time steps for the model integrations, planetary rotation rate, restoration timescales and Rayleigh friction timescales were given. Finally in chapter four the restoration and Rayleigh friction timescales used by other researchers were noted.

The model was tested using a thermal forcing profile as used by Lee (2006) with a temperature structure based on data from Seiff et al. (1985). The forcing profile was identified by its value of static stability at 10^6Pa, N_4 for this 'nominal' profile. Rayleigh friction was applied to the lowest model layer to simulate the atmospheric drag experienced and to the four top layers provide a 'sponge layer', to dampen any upward-propagating wave reflections from the model top. For each simulation the total atmospheric angular momentum (S) was calculated at the end of each Vday and plots were presented for the zonally averaged zonal wind ($\bar{u}$), local super-rotation index (s), mean meridional circulation (MMC), and temperature anomaly (ΔT).

The model was tested with a reference or base-line simulation with the sponge layer set to operate on eddy terms of the flow only. The zonal wind showed weaker winds than observed (Peralta et al., 2007; Sánchez-Lavega et al., 2008) with a peak

wind speed of approximately 50 $\mathrm{m\,s^{-1}}$ in two jets high in the atmosphere. The local super-rotation index, which is closely linked to $\bar{u}$, was also showed weaker than observed with a maximum value of 9.3 compared to $\simeq 60$ calculated from the observed winds. The MMC for this simulation showed a large Hadley cell in each hemisphere ranging for the equator to close to the pole with a smaller counter-rotating cell at the pole. The temperature anomaly showed cold poles above the clouds 10^4pa althouth the temperature anomaly throughout the rest of the atmosphere was within $\pm$1K.

Further experiments were made with the sponge layer operating on all terms. Notable in this simulation was the 'sponge layer' reducing the winds in the upper atmosphere close to zero and the absence of the jets. Otherwise the simulation yielded similar results to the sponge on eddies simulation.

The topography of Venus was introduced in section 5.4. A topographical dataset from the Magellan spacecraft's radar mapping of Venus (Ford and Pettengill, 1992) was used to make a spectral topography file for the model. An experiment made to test the influence of topography on the model's output using the $\mathrm{N_4}$ forcing profile.

The simulation reached equilibrium faster than the reference but with a lower magnitude of S. The results for zonal wind were similar to the reference simulation. Some negative (westward) flow was seen in the lower atmosphere below 10^6 Pa. A plot of the difference between the topography experiment and the reference simulation showed the zonal wind to be reduced below the clouds and generally increased above the clouds. The local super-rotation index was similar to the reference although with some $s<0$ below 10^6 Pa. MMC was stronger than reference with counter cells developing above the high elevation features of Ishtar Terra and Maxwell Montes in the Northern hemisphere.

In the next chapter experiments were performed with higher temperatures used for the forcing profiles. Four profiles were tested, the nominal N_4 used for the reference simulation and three with a higher temperature, especially in Venus' upper atmosphere. The stability was checked by calculating the Brunt-Viäsälä frequency (N) for each profile. It was seen how the stability increased with the temperature used for the forcing. The profiles were identified by their values of N^2 at 10^6Pa.

The experiments with modified background stability forcing were performed for simulations of 500 Vdays at resolutions of T21 at T42.

At T21 resolution, the graph of the time development of S showed how the magnitude of S and the time taken to reach equilibrium both increased as the stability increased. N_6 forcing showed a sudden increase in S between 240 and 280 Vdays before reaching equilibrium at approximately 310 Vdays, showing the importance of performing the simulation over a long enough time to ensure a stable equilibrium has been reached. The peak zonal winds increased as the stability increased, developing two jets at just above the cloud tops at latitudes of $\pm 45°$. The wind speeds which match observations most closely were found with N_5 forcing. The local super rotation index also increased in magnitude as the stability was increased. s showed a peak centred on the equator, also just above the cloud tops. The peak value for the N_5 forcing simulation was 50.5. The increase in $\bar{u}$ and s with increased stability indicated that simulation could be tuned to match the observed values precisely by changing the temperature used for the forcing and therefore the stability. The MMC weakened as the was stability increased, reducing the mean transport of angular momentum away from the equator in the upper levels of the atmosphere allowing the higher zonal wind to develop.

For the simulations at T42 resolution, which were run for 250 Vdays, all four of the forcing states had reached an equilibrium, taking a longer time to reach equilibrium

and a achieving higher magnitude of S for higher stability forcing. Although the magnitude was smaller than that found in the T21 experiments. The results for zonal wind and local super rotation index were relatively close for all four forcing states tested with the peak wind speed between 67.4 and 79.8 $\mathrm{m\,s^{-1}}$ and the maximum value for s between 15 and 28. MMC showed a monotonic reduction from N_4 to N_9 forcing.

Next a diurnal cycle was added to the model code. The 4D forcing profile required (long, lat, z, time) was described and results presented when the diurnal cycle was run with a maximum temperature increase of 100K over the basic N_4 temperatures. The results were very similar to those found for N_9 forcing (84K maximum increase) at T21 resolution shown earlier in the chapter. This indicated that the higher temperature used for the forcing and therefore the higher stability only needed to be applied for part of the simulation day in order to achieve the same result as would be found with 2D forcing and a constant higher temperature.

In the final results chapter the resolution was tested. First by varying the vertical resolution with 200, 100, 50 and 32 vertical levels used and then varying the horizontal resolution with simulations at T10, T21 and T42 with 50 vertical levels.

The experiments with changing vertical resolution were tested with both N_9 and N_4 forcing. With N_9 forcing the simulations with 50, 100 and 200 vertical levels reached equilibrium with $S \simeq 10.5$. L32 was still increasing slowly at the end of the 250 Vday simulation. It was suggested that this simulation would also reach equilibrium with $S \simeq 10.5$ were the simulation to run for longer.

The required computer time for the simulation was considered. The required time scales with the number of levels used, double the number of levels takes double the time. The L32 experiment had not reached equilibrium but using this scale would be expected to finish in 625 Vdays. In terms of computer time required L50 was therefore determined to be the most efficient number of vertical levels.

The zonal wind developed by the simulations were relatively close for 50 levels and greater, at 151 to 162 $\mathrm{m\,s^{-1}}$. The L32 experiment, which had not reached equilibrium, had developed a maximum wind speed of 116 $\mathrm{m\,s^{-1}}$, close to the observed value. All the simulations developed their peak wind in two jets at the cloud tops. The local super-rotation index was also relatively close for $\geq$ L50 (s= 78 to 86), L32 was again closer to the observed value at $s = 61$.

For N_4 forcing the total atmospheric angular momentum (S) developed was much lower than with N_9 forcing and all the simulations reached a statistical equilibrium within $\sim$ 100 Vdays. L32 had the lowest value of S (2.6) with L50, L100 and L200 much larger, developing 4.3, 4.8 and 4.5 respectively.

The zonal winds for these experiments all showed peak wind speed in two hemispherical jets at the top of the atmosphere modelled. Peak wind speeds were inversely correlated with S. L32 the highest at 62 $\mathrm{m\,s^{-1}}$, L50, L100 and L200 at 58, 51 and 52 $\mathrm{m\,s^{-1}}$ respectively. The wind speeds in the lower atmosphere were $\leq$ 30 $\mathrm{m\,s^{-1}}$ in all the experiments. Local super-rotation index was also weak and followed the same pattern as S and $\bar{u}$ with $s = 12$ for L32, $s = 9$ for L50, $s = 8$ for L100 and $s = 9$ for L200.

The simulations with varying horizontal resolutions were also performed with N_9 and N_4 forcing. With both forcing states the final value of S, time taken to reach equilibrium, the magnitude of the zonal wind and super-rotation were much higher for the T10 and T21 simulations than for T42. The zonal winds for the T10 simulations developed peak speeds in two jets at the cloud tops and $\pm 50°$ latitude for both forcing states. T21 developed cloud top jets only for N_9 forcing. When tested with N_4 forcing the jets were at the top of the atmosphere and at $\pm 75°$ latitude. The simulations at T42 horizontal resolution were quite similar for N_9 and N_4 forcing, with peak wind speeds of 72 and $\sim$ 80 $\mathrm{m\,s^{-1}}$. The peak speed developed in two jets at the top of the atmosphere at $\pm 60°$ latitude.

The magnitude of S and zonal winds developed for the experiments with T10 and T21 horizontal resolution compared to T42 suggest that the T10 and T21 simulations have produced unrealistically strong results. Possibly due to sub-grid scale processes whose effects reduce in significance with higher resolutions.

The final value of S and the time taken to reach equilibrium is strongly dependent on the horizontal resolution. The T42 simulations reached equilibrium in S in less time than lower resolutions which would allow the simulations to be run for a shorter time, offsetting the additional computing time required.

8.2 Rationale and key science

The aim of this research was to find out if atmospheric super-rotation could be reproduced in a Venus-like state when using a simplified model, and if so how robust it was to the choice of parameters. It was also an aim to gain an insight into the mechanisms that might support super-rotation. The details of the mechanisms which support super-rotation are impossible to quantify from the present, sparse observations of the planet but may be diagnosed from a model in a more straightforward manner.

In order to achieve these goals a global circulation model was developed, based on established code which was known to perform well at relatively low resolution. The lower resolution was necessary due to the very long thermal timescales in the Venus atmosphere and the necessity to run the model for long periods in order to achieve a statistical equilibrium. Simplified models, without a large computing overhead required, can be useful for testing changes to fundamental parameters (e.g. planetary radius, rotation rate, thermal forcing form and timescales) or to the setup of the model (e.g. initial conditions, resolution, dissipation, etc.). For this research tests of changes to the forcing function would be of particular interest. This was partly motivated as

Yamamoto and Takahashi (2003a) had found that super-rotation in their model was sensitive to the altitude at which the atmospheric temperature forcing peaked.

Super-rotation, a circulation of the atmosphere faster than the underlying planetary rotation, is a very notable feature of the Venus atmosphere, and is also known to occur on Titan, another slow rotator. As was shown in section 2.7, global super-rotation exists when an atmosphere has more total axial angular momentum than it would if in solid body rotation with the underlying planet. Local super-rotation is when somewhere in the atmosphere the zonal mean flow has more angular momentum about the planet's rotation axis than it would if the same air were at rest at the equator. Although the underlying mechanism(s) driving super-rotation cannot be uniquely determined immediately as a result of this research it was important that the model developed was able to reproduce super-rotating winds of a reasonable magnitude. Other Venus General Circulation Models (e.g. Yamamoto and Takahashi, 2003a, 2004; Lee et al., 2005; Lee and Richardson, 2010; Lebonnois et al., 2010; Mendonça et al., 2012) have produced super-rotation, but not with a magnitude which matched observations without the use of artificially strong forcing. It was also useful to gain a better understanding of how sensitive the model developed for this study was to the implementation of the model dynamics, the horizontal and vertical resolution used, the use of topography, the initial state, and the precise form of the forcing function used.

To begin the development, a pseudo-spectral model, derived from the model described by Hoskins and Simmons (1975), and a distant relation to the forecast model used by the ECMWF (European Centre for Medium range Weather Forecasting), and most recently the dynamical core of the model used for successful modelling of the Mars atmosphere (Read and Lewis, 2004, and references therein), was converted to Venus parameters. The Venus model was then tested to determine the optimum settings and sensitivity to various functions that can be set and switched within the code. The FORTRAN code for a routine to calculate the atmospheric heights from the Mars

Climate Database (MCD) was incorporated into the Venus model.

A temperature forcing state was generated from an atmospheric temperature profile as used by Lee (2006). The vertical temperature profile was very similar to that measured by the Magellan spacecraft suitably smoothed to reflect the vertical resolution that was available in the model. Settings for the strength of the surface friction and sponge layer were based on the ISSI inter-comparison protocol (Lebonnois et al., 2013). The sponge layer is included in the model in order to prevent waves from reflecting off the top of the model and growing resonantly within the domain. Therefore these reflections need to be suppressed without affecting the zonal mean flow.The sponge layer takes the form of enhanced linear dissipation in the upper four levels (increasing strongly with height) that acts only on the eddy terms and not on the zonal mean terms.

The model was then first tested with the simplest possible configuration. These tests were made at T21 resolution with 50 vertical levels with no additional functions enabled such as topography or the diurnal cycle. The tests were made to determine the sensitivity to whether the sponge layer was set to operate on all terms or only the eddy terms. Set-up with this configuration the model generated only weak super-rotation at $\sim 50\,\mathrm{m\,s^{-1}}$, in two jets high in the atmosphere. It was found that with the sponge layer set to operate on all terms the winds in the top of the atmosphere were entirely suppressed. Routines were written to calculate the total atmospheric angular momentum (AAM) and this was used as a primary diagnostic which allows simple comparison between different model configurations and different models. The AAM was calculated for these tests to provide a baseline for later tests.

Following these first tests it was decided to perform later experiments with the sponge layer set to operate on eddies only, due to the wind in the upper atmosphere. Other researchers also have used the sponge layer set to operate on eddies only (e.g.

Lewis and Read, 2003; Lee et al., 2007)

A spectral topography file was generated from detailed topography data from the Magellan mission's radar mapping of the surface of Venus. The model was then run using this spectral topography file at T21 resolution with 50 vertical levels and the sponge layer set to operate only on the eddy terms. The wind results were similar in the upper atmosphere to the previous simple configuration tests however the effect of the topography could be seen in the lower atmosphere, especially the effect of the high ground in the region of Maxwell Montes at $\sim 65.2°$ N. A large reduction in AAM was seen. Difference plots of the zonal wind, with the non-topography simulation, showed that this was due to the lower strength of the wind near the surface.

Temperature restoration states with increased temperature and modified gradients and lapse rates were made, which were found to result in increased static stability (Brunt-Väisälä frequency squared, N^2) in the lower atmosphere. Values for N^2 were calculated, and used to describe the restoration states. Super-rotation was much stronger with higher temperature and therefore higher stability. The increase in zonal wind was accompanied by a weakening in the strength of the MMC. It was found that the zonal wind could be tuned by adjusting the vertical lapse rate of the atmospheric temperature used for the restore state, and therefore the atmospheric static stability.

A diurnal cycle was coded and added to the model. This included a stronger cycle forcing towards a 100K temperature increase over the zonal-mean temperature state at local mid-day. It has been suggested that diurnal thermal tides may be responsible for forcing the super-rotation (e.g. Kido and Wakata, 2009). Also tides have been shown to be primarily responsible for the local-super rotation on Mars (Lewis and Read, 2003). The strength of the diurnal cycle was varied to test the relative impact of tides on Venus. The results were very similar to those found for N_9 forcing (described in chapter 6) which has a higher temperature permanently applied.

The sensitivity to the vertical resolution was tested with runs with at 32, 50, 100 & 200 vertical levels. The results for these experiments indicated < 32 vertical levels was insufficient with AAM low. At > 32 vertical levels, 50, 100 and 200 ultimately reach equilibrium at approximately the same magnitude of AAM. The most computationally efficient was to use 50 vertical levels.

Sensitivity to horizontal resolution was tested at T10, T21 & T42. Simulations at T10 gave unrealistically strong super-rotation. It was concluded that when performing experiments at T10 resolution that the model scale-selective dissipation was overestimating the momentum transport by non-resolved eddies which are resolved explicitly in higher resolution experiments, ultimately leading to the strong super-rotation. Experiments at T21 resolution showed the previously described large difference between the N_4 & N_9 forcing states. For T42 resolution the differences between the N_4 & N_9 forcing states were much less. In general, the results were less sensitive to arbitrary model parameters at higher horizontal resolution, however the runtimes were longer. A compromise needed to be made between resolving as larger range of scales as possible and the time available for the experiment. It should be noted that when changing the resolution the artificial diffusion also changed and this impacts the super-rotation observed in the model, suggesting that much of the strong super-rotation at low resolutions is a direct result of parametrised dissipation and that at higher resolutions the model took longer to reproduce this transport with better resolved eddies at a range of horizontal scales.

8.3 Aims of the research

The model developed and described in this thesis did produce super-rotation although weaker than is observed on Venus when using realistic forcing. Super-rotation which

matched observations could be achieved by increasing the temperature profile used for the forcing, which increases the stability in the lower atmosphere.

The sensitivity of the model to vertical and horizontal resolution was tested. It was concluded that 50 vertical levels was sufficient to achieve good results with different forcing profiles used. The horizontal resolution should be as high as possible for the available computer resources.

Topography was included in the model and found to make little difference to the super-rotation although the time taken to reach equilibrium was reduced. The meridional circulation was strengthened and the effect of high elevation topographical features could be seen in the circulation.

Experiments with a thermal tide were performed by adding a diurnal cycle. Tests were performed with enhanced temperature used for the forcing with results which matched the non-diurnal tests very closely. Due to limitations in the diurnal cycle code preventing a restart and the settings used, storing the model data every Vday rather than more frequently, the waves generated could not be diagnosed.

8.4 Future work

Suggestions for possible future work could include the following:

The VSGCM code contains an ECMWF (European Centre for Medium Range Weather Forecasting) angular momentum conserving scheme. Some tests could be done for angular momentum to test this scheme and identify the magnitude of any errors. Global S can only vary through:

1. Rayleigh friction in the surface layer.

2. The sponge layer if it is applied to zonal terms as well as eddies.
3. Mechanical forcing from topography.
4. Explicit diffusion on zonal terms.
5. Numerical no conservation issues.

1 and 4 can be calculated, choosing a model run with the sponge layer set only for eddy terms and with no topography will mean 2 and 3 are zero. By running the VSGCM with the output saved to the 'history' file many times per day (200) once in equilibrium then finding dS/dt the contribution from the diffusion and numerical terms can be checked and quantified.

In order to improve the VSGCM as a model for the atmosphere of Venus and allow further tests of the dynamics and features of the circulation several refinements could be made. The maximum altitude could be increased. Currently the maximum is 77 km, slightly above the top of the troposphere at 65 km. Many other researchers have used $\sim$ 90 km in their models (e.g. Yamamoto and Takahashi, 2003a; Lee et al., 2007). Alternatively 110 km would include the mesosphere totally.

It was shown in chapter 7 that running the model with more than L50 gives no significant difference in super-rotation or S developed at any of the horizontal resolutions tested or with any of the forcing profiles used. For efficiency of computer time required L50 can be selected for future simulations. Run time for the model is not increased with the use of topography or the diurnal cycle so these features can also be retained.

The horizontal resolution was shown in section 7.3 to produce robust results at T42 resolution with no penalty in computing time required. Also the influence of sub-grid scale processes appeared reduced. The horizontal resolution can be set for higher resolutions than used for this study, T63 or T85 to investigate whether this trend continues and to give finer detail in the model output.

Lebonnois et al. (2010) describe the method used by the LMDZ GCM for calculating the value of the specific heat, C_p, which varies from 738 J/kg/K at 100 km altitude to 1181 J/kg/K near the surface (values from the Venus International Reference Atmosphere (VIRA), Seiff et al., 1985). The variation in C_P with temperature (altitude) can be approximated by:

$$C_p(T) = C_{p0} \times \left(\frac{T}{T_0}\right)^{\nu} \tag{8.1}$$

where: $C_{p0} = 1000$ J/kg/K, $T_0 = 460$ K, and $\nu = 0.35$

This variation of C_p with temperature needs to be taken into account in order to get realistic adiabatic lapse rates in the whole atmosphere and should be incorporated into the VSGCM.

The diurnal cycle implemented in the VSGCM does not allow a simulation to be stopped and restarted. This prevents a simulation from being 'spun up' to an equilibrium and then parameters modified before a restart. To save required computer time and the need to start simulations from rest the code should be updated to allow restarting of an already spun up simulation.

Further work with the code for the diurnal cycle should include testing with different forcing. Generating a 4D forcing profile which only has a temperature increase at the cloud tops would more accurately simulate the insolation received by Venus. The changes proposed for the diurnal cycle would allow experiments with thermal tides to be performed, as stated in the original aims for the research.

Bibliography

Andrews, D. G. (2000). *Atmospheric Physics*, pages 229–+. Cambridge University Press.

Arakawa, A. (1966). Computational Design for Long-Term Numerical Integration of the Equations of Fluid Motion: Two-Dimensional Incompressible Flow. Part I. *Journal of Computational Physics*, **1**:119–+.

Bougher, S. W.; Alexander, M. J. and Mayr, H. G. (1997). Upper Atmosphere dynamics: global circulation and gravity waves. In S. W. Bougher; D. M. Hunten and R. J. Philips, editors, *Venus II: Geology, Geophysics, Atmosphere, and Solar Wind Environment*, pages 259–291.

Collins, M. and James, I. N. (1995). Regular baroclinic transient waves in a simplified global circulation model of the Martian atmosphere. *Journal of Geophysical Research*, **1001**:14421–14432.

Collins, M.; Lewis, S. R.; Read, P. L. and Hourdin, F. (1996). Baroclinic Wave Transitions in the Martian Atmosphere. *Icarus*, **120**:344–357.

Covey, C.; Pitcher, E. J. and Brown, J. P. (1986). General circulation model simulations of superrotation in slowly rotating atmospheres - Implications for Venus. *Icarus*, **66**:380–396.

Crespin, A.; Lebonnois, S.; Hourdin, F.; Eymet, V.; Fournier, R. and Forget, F. (2006). Simulations of the Dynamics of Venus' Atmosphere with the LMD Venus General Circulation Model. In *Bulletin of the American Astronomical Society*, volume 38 of *Bulletin of the American Astronomical Society*, pages 515–+.

Davies, M. E.; Colvin, T. R.; Rogers, P. G.; Chodas, P. W.; Sjogren, W. L.; Akim, E. L.; Stepaniants, V. A.; Vlasova, Z. P. and Zakharov, A. I. (1992). The rotation period, direction of the north pole, and geodetic control network of Venus. *Journal of Geophysical Research*, **97**:13141–+.

de Bergh, C.; Moroz, V. I.; Taylor, F. W.; Crisp, D.; Bézard, B. and Zasova, L. V. (2006). The composition of the atmosphere of Venus below 100 km altitude: An overview. *Planetary and Space Science*, **54**:1389–1397.

del Genio, A. D. and Rossow, W. B. (1990). Planetary-scale waves and the cyclic nature of cloud top dynamics on Venus. *Journal of Atmospheric Sciences*, **47**:293–318.

del Genio, A. D. and Zhou, W. (1996). Simulations of Superrotation on Slowly Rotating Planets: Sensitivity to Rotation and Initial Condition. *Icarus*, **120**:332–343.

del Genio, A. D.; Zhou, W. and Eichler, T. P. (1993). Equatorial superrotation in a slowly rotating GCM - Implications for Titan and Venus. *Icarus*, **101**:1–17.

Donner, L. and Large, W. (2008). Climate modeling. *Annual Review of Environment and Resources*, **33**:1–17.

Fegley, B., Jr.; Klingelhöfer, G.; Lodders, K. and Widemann, T. (1997). Geochemistry of Surface-Atmosphere interactions on Venus. In S. W. Bougher; D. M. Hunten and R. J. Philips, editors, *Venus II: Geology, Geophysics, Atmosphere, and Solar Wind Environment*, pages 591–636.

Ford, P. G. and Pettengill, G. H. (1992). Venus topography and kilometer-scale slopes. *Journal of Geophysical Research*, **97**:13103.

Forget, F.; Hourdin, F.; Fournier, R.; Hourdin, C.; Talagrand, O.; Collins, M.; Lewis, S. R.; Read, P. L. and Huot, J.-P. (1999). Improved general circulation models of the Martian atmosphere from the surface to above 80 km. *Journal of Geophysical Research (Planets)*, **104**:24155–24176.

Gierasch, P. J. (1975). Meridional circulation and the maintenance of the Venus atmospheric rotation. *Journal of Atmospheric Sciences*, **32**:1038–1044.

Gierasch, P. J.; Goody, R. M.; Young, R. E.; Crisp, D.; Edwards, C.; Kahn, R.; Rider, D.; del Genio, A.; Greeley, R.; Hou, A.; Leovy, C. B.; McCleese, D. and Newman, M. (1997). The General Circulation of the Venus Atmosphere: an Assessment. In S. W. Bougher; D. M. Hunten and R. J. Philips, editors, *Venus II: Geology, Geophysics, Atmosphere, and Solar Wind Environment*, pages 459–+.

Goody, R. M. and Robinson, A. R. (1966). A Discussion of the Deep Circulation of the Atmosphere of Venus. *Astrophysical Journal*, **146**:339–+.

Goody, R. M. and Yung, Y. L. (1989). *Atmospheric radiation : theoretical basis*. Atmospheric radiation : theoretical basis, 2nd ed., by Richard M. Goody and Y.L. Yung. New York, NY: Oxford University Press, 1989.

Haberle, R. M.; Pollack, J. B.; Barnes, J. R.; Zurek, R. W.; Leovy, C. B.; Murphy, J. R.; Lee, H. and Schaeffer, J. (1993). Mars atmospheric dynamics as simulated by the NASA AMES General Circulation Model. I - The zonal-mean circulation. *Journal of Geophysical Research*, **98**:3093–3123.

Held, I. M. and Hou, A. Y. (1980). Nonlinear Axially Symmetric Circulations in a Nearly Inviscid Atmosphere. *Journal of Atmospheric Sciences*, **37**:515–533.

Herrnstein, A. and Dowling, T. E. (2007). Effects of topography on the spin-up of a Venus atmospheric model. *Journal of Geophysical Research (Planets)*, **112**:4–+.

Hide, R. (1969). Dynamics of the Atmospheres of the Major Planets with an Appendix on the Viscous Boundary Layer at the Rigid Bounding Surface of an Electrically-Conducting Rotating Fluid in the Presence of a Magnetic Field. *Journal of Atmospheric Sciences*, **26**:841–853.

Hollingsworth, J. L.; Young, R. E.; Schubert, G.; Covey, C. and Grossman, A. S. (2007). A simple-physics global circulation model for Venus: Sensitivity assessments of atmospheric superrotation. *Geophysical Research Letters*, **34**:5202–+.

Hoskins, B. J. and Simmons, A. J. (1975). A multi-layer spectral model and the semi-implicit method. *Quarterly Journal of the Royal Meteorological Society*, **101**:637–655.

Hussey, T. (1832). On the rotation of Venus. *MNRAS*, **2**:78–+.

Ip, W.-H. and Fernandez, J. A. (1988). Exchange of condensed matter among the outer and terrestrial protoplanets and the effect on surface impact and atmospheric accretion. *Icarus*, **74**:47–61.

Joshi, M. M.; Lawrence, B. N. and Lewis, S. R. (1995). Gravity wave drag in three-dimensional atmospheric models of Mars. *Journal of Geophysical Research*, **1002**:21235–21246.

Kalnay de Rivas, E. (1975). Further numerical calculations of the circulation of the atmosphere of Venus. *Journal of Atmospheric Sciences*, **32**:1017–1024.

Kasting, J. F. (1988). Runaway and moist greenhouse atmospheres and the evolution of earth and Venus. *Icarus*, **74**:472–494.

Kido, A. and Wakata, Y. (2009). Multiple Equilibrium States Appearing in a Venus-like Atmospheric General Circulation Model with Three-dimensional Solar Heating. *SOLA*, **5**:85–88. ISSN 1349-6476.

Lebonnois, S.; Hourdin, F.; Eymet, V.; Crespin, A.; Fournier, R. and Forget, F. (2010). Superrotation of Venus' atmosphere analyzed with a full general circulation model. *Journal of Geophysical Research (Planets)*, **115**:6006–+.

Lebonnois, S.; Lee, C.; Yamamoto, M.; Dawson, J.; Lewis, S. R.; Mendonca, J.; Read, P.; Parish, H. F.; Schubert, G.; Bengtsson, L.; Grinspoon, D.; Limaye, S. S.; Schmidt, H.; Svedhem, H. and Titov, D. V. (2013). Models of Venus Atmosphere. In L. Bengtsson; R.-M. Bonnet; D. Grinspoon; S. Koumoutsaris; S. Lebonnois and D. Titov, editors, *Towards Understanding the Climate of Venus*, page 129.

Lee, C. (2006). *Modelling the Atmosphere of Venus*. DPhil. thesis, University of Oxford.

Lee, C.; Lewis, S. R. and Read, P. L. (2005). A numerical model of the atmosphere of Venus. *Advances in Space Research*, **36**:2142–2145.

——— (2007). Superrotation in a Venus general circulation model. *Journal of Geophysical Research (Planets)*, **112**:4–+.

——— (2010). A bulk cloud parameterization in a Venus General Circulation Model. *Icarus*, **206**:662–668.

Lee, C. and Richardson, M. I. (2010). A general circulation model ensemble study of the atmospheric circulation of Venus. *Journal of Geophysical Research (Planets)*, **115**:4002–+.

Leovy, C. B. (1973). Rotation of the upper atmosphere of Venus. *Journal of Atmospheric Sciences*, **30**:1218–1220.

Lewis, S. R.; Collins, M.; Read, P. L.; Forget, F.; Hourdin, F.; Fournier, R.; Hourdin, C.; Talagrand, O. and Huot, J.-P. (1999). A climate database for Mars. *Journal of Geophysical Research*, **104**:24177–24194.

Lewis, S. R. and Read, P. L. (2003). Equatorial jets in the dusty Martian atmosphere. *Journal of Geophysical Research (Planets)*, **108**:5034–+.

Lewis, S. R.; Read, P. L. and Collins, M. (1996). Martian atmospheric data assimilation with a simplified general circulation model: orbiter and lander networks. *Planetary and Space Science*, **44**:1395–1409.

Marov, M. Y. (2005). Mikhail Lomonosov and the discovery of the atmosphere of Venus during the 1761 transit. In D. W. Kurtz, editor, *IAU Colloq. 196: Transits of Venus: New Views of the Solar System and Galaxy*, pages 209–219.

Mayr, H. G. and Harris, I. (1983). Quasi-axisymmetric circulation and superrotation in planetary atmospheres. *Astronomy and Astrophysics*, **121**:124–136.

McGuffie, K. and Henderson-Sellers, A. (2005). *A climate modelling primer*. Research and developments in climate. John Wiley. ISBN 9780470857519.

Mendonça, J. M.; Read, P. L.; Wilson, C. F. and Lewis, S. R. (2012). Zonal winds at high latitudes on Venus: An improved application of cyclostrophic balance to Venus Express observations. *Icarus*, **217**:629–639.

Mills, F. P.; Esposito, L. W. and Yung, Y. L. (2007). Atmospheric Composition, Chemistry, and Clouds. In L. W. Esposito; E. R. Stofan and T. E. Cravens, editors, *Exploring Venus as a Terrestrial Planet*, pages 73–100.

NASA PDS (2009a). Encyclopedia of Standard Planetary Information, Formulae, and Constants. `http://pds-atmospheres.nmsu.edu/education_and_outreach/encyclopedia/gas_constant.htm` Online; accessed 15-September-2012.

——— (2009b). Encyclopedia of Standard Planetary Information, Formulae, and Constants. `http://pds-atmospheres.nmsu.edu/education_and_outreach/encyclopedia/atmospheric_parameters.htm` Online; accessed 15-September-2012.

Newman, C. E.; Lewis, S. R.; Read, P. L. and Forget, F. (2002). Modeling the Martian dust cycle, 1. Representations of dust transport processes. *Journal of Geophysical Research (Planets)*, **107**:5123.

Newman, M. and Leovy, C. (1992). Maintenance of strong rotational winds in Venus' middle atmosphere by thermal tides. *Science*, **257**:647–650.

Peralta, J.; Hueso, R. and Sánchez-Lavega, A. (2007). A reanalysis of Venus winds at two cloud levels from Galileo SSI images. *Icarus*, **190**:469–477.

Pettengill, G. and Price, R. (1961). Radar echoes from Venus and a new determination of the solar parallax. *Planetary and Space Science*, **5**:71–74.

Read, P. L. (1986a). Super-rotation and diffusion of axial angular momentum. I. "Speed limits" for axisymmetric flow in a rotating cylindrical fluid annulus. *Quarterly Journal of the Royal Meteorological Society*, **112**:231–251.

——— (1986b). Super-rotation and diffusion of axial angular momentum. II. A review of quasi-axisymmetric models of planetary atmospheres. *Quarterly Journal of the Royal Meteorological Society*, **112**:253–272.

Read, P. L. and Lewis, S. R. (2004). The martian climate revisited: atmosphere and environment of a desert planet. In *The Martian climate revisited: atmosphere and environment of a desert planet*, volume 26 of *Springer Praxis Books: Geophysical Sciences*. Springer.

Riehl, H. and Fultz, D. (1958). The general circulation in a steady rotating-dishpan experiment. *Quarterly Journal of the Royal Meteorological Society*, **84**:389–417.

Rossow, W. B. (1983). A general circulation model of a Venus-like atmosphere. *Journal of Atmospheric Sciences*, **40**:273–302.

Rossow, W. B.; Fels, S. B. and Stone, P. H. (1980). Comments on 'A three-dimensional model of dynamical processes in the Venus atmosphere'. *Journal of Atmospheric Sciences*, **37**:250–252.

Rossow, W. B. and Williams, G. P. (1979). Large-scale motion in the Venus stratosphere. *Journal of Atmospheric Sciences*, **36**:377–389.

Sánchez-Lavega, A.; Hueso, R.; Piccioni, G.; Drossart, P.; Peralta, J.; Pérez-Hoyos, S.; Wilson, C. F.; Taylor, F. W.; Baines, K. H.; Luz, D.; Erard, S. and Lebonnois, S. (2008). Variable winds on Venus mapped in three dimensions. *Geophysical Research Letters*, **35**:13204–+.

Saunders, R. S.; Pettengill, G. H.; Arvidson, R. E.; Sjogren, W. L.; Johnson, W. T. K. and Pieri, L. (1990). The Magellan Venus radar mapping mission. *Journal of Geophysical Research*, **95**:8339–8355.

Schofield, J. T. and Taylor, F. W. (1983). Measurements of the mean, solar-fixed temperature and cloud structure of the middle atmosphere of Venus. *Quarterly Journal of the Royal Meteorological Society*, **109**:57–80.

Schubert, G. (1983). General circulation and the dynamical state of the Venus atmosphere. In D. M. Hunten; L. Colin; T. M. Donahue and V. I. Moroz, editors, *Venus*, pages 681–765.

Schubert, G.; Covey, C.; del Genio, A.; Elson, L. S.; Keating, G.; Seiff, A.; Young, R. E.; Apt, J.; Counselman, C. C.; Kliore, A. J.; Limaye, S. S.; Revercomb, H. E.;

Sromovsky, L. A.; Suomi, V. E.; Taylor, F.; Woo, R. and von Zahn, U. (1980). Structure and circulation of the Venus atmosphere. *Journal of Geophysical Research*, **85**:8007–8025.

Schubert, G. and Whitehead, J. A. (1969). Moving Flame Experiment with Liquid Mercury: Possible Implications for the Venus Atmosphere. *Science*, **163**:71–72.

Seidelmann, P. K.; Archinal, B. A.; A'Hearn, M. F.; Cruikshank, D. P.; Hilton, J. L.; Keller, H. U.; Oberst, J.; Simon, J. L.; Stooke, P.; Tholen, D. J. and Thomas, P. C. (2005). Report of the IAU/IAG Working Group on Cartographic Coordinates and Rotational Elements: 2003. *Celestial Mechanics and Dynamical Astronomy*, **91**:203–215.

Seiff, A.; Schofield, J. T.; Kliore, A. J.; Taylor, F. W. and Limaye, S. S. (1985). Models of the structure of the atmosphere of Venus from the surface to 100 kilometers altitude. *Advances in Space Research*, **5**:3–58.

Spiga, A.; Forget, F.; Madeleine, J.-B.; Montabone, L.; Lewis, S. R. and Millour, E. (2011). The impact of martian mesoscale winds on surface temperature and on the determination of thermal inertia. *Icarus*, **212**:504–519.

Stone, P. H. (1974). The Structure and Circulation of the Deep Venus Atmosphere. *Journal of Atmospheric Sciences*, **31**:1681–1690.

Svedhem, H.; Titov, D. V.; Taylor, F. W. and Witasse, O. (2007). Venus as a more Earth-like planet. *Nature*, **450**:629–632.

Taylor, F. and Grinspoon, D. (2009). Climate evolution of Venus. *Journal of Geophysical Research (Planets)*, **114**:E00B40.

Taylor, F. W. (2006). Venus before Venus Express. *Planetary and Space Science*, **54**:1249–1262.

Taylor, F. W.; Beer, R.; Chahine, M. T.; Diner, D. J.; Elson, L. S.; Haskins, R. D.; McCleese, D. J.; Martonchik, J. V.; Reichley, P. E.; Bradley, S. P.; Delderfield, J.; Schofield, J. T.; Farmer, C. B.; Froidevaux, L.; Leung, J.; Coffey, M. T. and Gille, J. C. (1980). Structure and meteorology of the middle atmosphere of Venus Infrared remote sensing from the Pioneer orbiter. *Journal of Geophysical Research*, **85**:7963–8006.

Urey, H. C. (1961). *The Planets*, pages 199–+. Science in Space.

Yamamoto, M. and Takahashi, M. (2003a). Superrotation and equatorial waves in a T21 Venus-like AGCM. *Geophysical Research Letters*, **30**(9):090000–1.

——— (2003b). The Fully Developed Superrotation Simulated by a General Circulation Model of a Venus-like Atmosphere. *Journal of Atmospheric Sciences*, **60**:561–574.

——— (2004). Dynamics of Venus' superrotation: The eddy momentum transport processes newly found in a GCM. *Geophysical Research Letters*, **31**:9701–+.

——— (2006). Superrotation Maintained by Meridional Circulation and Waves in a Venus-Like AGCM. *Journal of Atmospheric Sciences*, **63**:3296–3314.

Young, R. E. and Pollack, J. B. (1977). A three-dimensional model of dynamical processes in the Venus atmosphere. *Journal of Atmospheric Sciences*, **34**:1315–1351.

Young, R. E.; Walterscheid, R. L.; Schubert, G.; Seiff, A.; Linkin, V. M. and Lipatov, A. N. (1987). Characteristics of gravity waves generated by surface topography on Venus - Comparison with the VEGA Balloon results. *Journal of Atmospheric Sciences*, **44**:2628–2639.